

HEMISPHERICAL OPTICAL MICROCAVITY FOR CAVITY-QED STRONG
COUPLING

by

JUSTIN MICHIO HANNIGAN

A DISSERTATION

Presented to the Department of Physics
and the Graduate School of the University of Oregon
in partial fulfillment of the requirements
for the degree of
Doctor of Philosophy

December 2009

University of Oregon Graduate School

Confirmation of Approval and Acceptance of Dissertation prepared by:

Justin Hannigan

Title:

"Optical Microcavities for Cavity-QED Strong Coupling"

This dissertation has been accepted and approved in partial fulfillment of the requirements for the Doctor of Philosophy degree in the Department of Physics by:

Hailin Wang, Chairperson, Physics
Michael Raymer, Advisor, Physics
Jens Noeckel, Member, Physics
Richard Taylor, Member, Physics
Andrew Marcus, Outside Member, Chemistry

and Richard Linton, Vice President for Research and Graduate Studies/Dean of the Graduate School for the University of Oregon.

December 12, 2009

Original approval signatures are on file with the Graduate School and the University of Oregon Libraries.

© 2009 Justin Michio Hannigan

be capable of displaying strong coupling. The dipole coupling strength, cavity loss and quantum dot dephasing rates are estimated to be, respectively, $g = 35\mu\text{eV}$, $\kappa = 30\mu\text{eV}$, and $\gamma = 15\mu\text{eV}$.

A survey of two different distributed Bragg reflector (DBR) samples was carried out. Four different probe lasers were used to measure transmission spectra for the coupled cavity-QED system.

The system initially failed to display strong coupling due to the available lasers being too far from the design wavelength of the spacer layer, corresponding to a loss of field strength at the location of the quantum dots. Unfortunately, the only available lasers capable of probing the design wavelength of the spacer layer had technical problems that prevented us from obtaining clean spectra. Both a Ti:Al₂O₃ and a diode laser were used to measure transmission over the design wavelength range.

The cavity used here has many promising features and should be capable of displaying strong coupling. It is believed that with a laser system centered at the design wavelength and possessing low enough linewidth and single-mode operation across a wide wavelength range strong coupling should be observable in this system.

CURRICULUM VITAE

NAME OF AUTHOR: Justin Michio Hannigan

PLACE OF BIRTH: Hilo, Hawaii

DATE OF BIRTH: July 18, 1977

GRADUATE AND UNDERGRADUATE SCHOOLS ATTENDED:

University of Oregon

University of Hawaii, Hilo

DEGREES AWARDED:

Doctor of Philosophy in Physics, 2009, University of Oregon

Bachelor of Science in Physics and Mathematics, 2000, University of Oregon

AREAS OF SPECIAL INTEREST:

Quantum Optics

Quantum Information

Semiconductor Optics

PROFESSIONAL EXPERIENCE:

Graduate Research Assistant,
University of Oregon, 2000 – 2009

Graduate Teaching Assistant,
University of Oregon, 2006 – 2007

Physics and Mathematics Tutor,
Academic Learning Services,
University of Oregon, 1998 - 2000

PUBLICATIONS:

G. Cui, J. M. Hannigan, R. Loeckenhoff, F. M. Matinaga, M. G. Raymer, S. Bhongale, M. Holland, S. Mosor, S. Chatterjee, H. M. Gibbs, and G. Khitrova. A hemispherical, high-solid-angle optical micro-cavity for cavity- QED studies. *Opt. Express*, 14(6):22892299, 2006 .

ACKNOWLEDGEMENTS

First and foremost I would like to acknowledge my adviser, Michael Raymer. He has seen my academic journey progress from the point when I first entered the University of Oregon as an undergraduate to the completion of my studies as a graduate student. While I consider that many things could have gone better during my graduate career, Mike has proven himself as a steadfast and dedicated adviser. I have truly learned a lot from him, both as a physicist and as a human. I consider myself fortunate to have been able to work on this project, despite the lack of positive results. I have struggled and learned a lot during this time at the University of Oregon.

I thank Hyatt Gibbs and Galina Khitrova for their work in designing, fabricating and characterizing the semiconductor structures used in this work as well as for providing surface characterization for the micro-mirrors that we produced. This work would not have been possible without their hard work and expertise.

Murray Holland should also be acknowledged for providing early calculations that provided estimates of mode volume for the microcavity modes as well as helping secure funding for the project.

Of course, I must acknowledge my colleague of many years in this work, Guoqiang Cui. Our time together working on this project led to a close relationship

and I truly consider him to be one of my closest friends. Our trajectories have diverged, but I am sure they will cross again in the future.

I must also acknowledge David Foster, my predecessor on this project. He is responsible for many engineering details, including design of the tripod structure and the vacuum chamber. His attention to detail provided a good example for me when pursuing further design work.

It was also a great experience to work with Franklin Matinaga. He came to work with us from Universidade Federal de Minas Gerais on two separate occasions. His experience was of great help in obtaining good signal quality in the cavity-modified photoluminescence experiments.

I must acknowledge the Technical Science Administration professionals who have provided excellent support in many aspects of design and construction. Thanks to David Senkovich, Kris Johnson, John Boosinger, Jeffrey Garman and Cliff Dax for helpful guidance and support over the years.

Thanks also to my entire committee (Michael Raymer, Hailin Wang, Jens Nöckel, Richard Taylor and Andrew Marcus) for supporting me.

Thanks to Andrew Cook for sharing in adventures with me.

Finally, I must acknowledge my parents (Stephen and Jeanne Hannigan) for encouraging curiosity and allowing intellectual freedom. I hope to provide such an environment for my daughter, Lillian.

DEDICATION

To my daughter, Lillian Haruko Hannigan-Thompson: I dedicate this work to you.

Believe in yourself and live your dreams. I love you.

TABLE OF CONTENTS

Chapter	Page
I. INTRODUCTION	1
1.1 Introduction	1
1.2 Context	1
1.3 Motivation	4
1.4 Outline	12
II. THEORY	15
2.1 Overview	15
2.2 Theoretical Considerations for IFQDs	15
2.3 The Jaynes-Cummings Hamiltonian	24
2.4 Diagonalization — Normal Modes	55
2.5 Linewidth, Dissipation and Open Systems	70
2.6 Numerical Studies of Non-paraxial Modes	93
III. THE HEMISPHERICAL MICROCAVITY	100
3.1 Flat Semiconductor DBR Containing QDs	100
3.2 Large Solid-Angle Micro-mirrors	108
3.3 Mounted Micro-mirrors	115
3.4 The Near-hemispherical Microcavity	119
3.5 Tripod Support System	122
3.6 Cryostat and Cold-Finger	129
3.7 Ultra-high Vacuum Chamber	130
3.8 Summary	132
IV. EXPERIMENTS AND DATA	135
4.1 Introduction	135
4.2 Input Beams	135
4.3 Output Beams	138
4.4 Mode Matching	141
4.5 Cavity-Modified Photoluminescence	145

Chapter	Page
4.6 Using the Newport Laser as Probe	146
4.7 Using the New Focus Laser as Probe	152
4.8 Sacher LiON as Probe	154
V. CONCLUSIONS AND OUTLOOK	160
5.1 Conclusions	160
5.2 Improvements to the Apparatus	165
5.3 Outlook	166
APPENDICES	
A. TIME-DEPENDENCE OF EXPECTATION VALUES	168
B. QUANTIZATION OF A PARAXIAL RESONATOR	177
B.1 Classical Field of the Resonator	177
C. ACRONYMS	194
BIBLIOGRAPHY	199

LIST OF FIGURES

Figure	Page
1.1 A QCPG scheme based on trion-trion interactions.	6
1.2 Entangled photon pairs from a biexciton coupling to cavity	9
2.1 Bulk GaAs band structure near Γ	17
2.2 Selection rules for QDs in two bases.	18
2.3 Selection rules — axisymmetric QD	20
2.4 Anisotropic exchange splitting	22
2.5 Selection rules — asymmetric QD	23
2.6 2-level system energies	26
2.7 E/M field energy levels	37
2.8 Rotation from bare states into dressed states	61
2.9 Effect of interaction on energy levels; normal mode splitting	63
2.10 Energies of bare and dressed states	65
2.11 Rabi flopping	69
2.12 Quantum dynamical map	73
2.13 Transmission spectrum	92
2.14 FDTD calculation of micro-cavity modes	94

Figure	Page
2.15 Gaussian to V-mode transition	96
2.16 Amplitude at $y=0$ and polarization for $z=0$	97
3.1 DBR surface roughness	101
3.2 DBR reflectivity as a function of distance	103
3.3 Reflection spectrum for CAT96 and CAT97	105
3.4 Micro-PL for CAT96 and CAT97	106
3.5 Nano-PL from CAT97	107
3.6 Micro-mirror substrate preparation	110
3.7 Procedure for removing glass chips with PDMS films	112
3.8 Micro-mirror sphericity and surface roughness	114
3.9 Micro-mirror $T(\theta)$: Setup and data	116
3.10 Twyman-Green interferometer for mounting micro-mirrors	118
3.11 Cavity stability parameters	120
3.12 Flexure mount for X-Y translation	124
3.13 Schematic of sample column	126
3.14 Hidden line drawing of the support structure	128
3.15 Schematic of cooling system	131
3.16 Schematic: ultra-high vacuum (UHV) system	133
3.17 Photograph of the support tripod and cooling system	134
4.1 Laser sources filtered by single-mode fiber	137

Figure	Page
4.2	Detection setup for active control of cavity length 139
4.3	Detection configuration for passive cavity control 141
4.4	Lens system schematic 143
4.5	Effect of the lens system 144
4.6	Cavity-modified PL — setup 146
4.7	Cavity-modified PL — short cavity 147
4.8	Cavity-modified PL — long cavity 148
4.9	Polarized PL from intracavity IFQDs 149
4.10	A missing peak 150
4.11	Narrow absorption tuned through modes 151
4.12	Doublets except on the fundamental 153
4.13	Sacher single peaks 154
4.14	Sacher — strange features 155
4.15	Sacher — double peaks 155
4.16	Sacher vs. New Focus spectra 156
4.17	Length scans with Sacher laser at 765 nm 157
4.18	Length scans for fixed probe at various locations on the sample 159

LIST OF TABLES

Table	Page
3.1 Properties of borosilicate microcaps	109
3.2 Micro-cavity parameters	120
3.3 Relevant degrees of freedom and their role in the experiment	123

CHAPTER I

INTRODUCTION

1.1 Introduction

This dissertation reports on the effectiveness of near-hemispherical microcavities for achieving strong coupling between a single exciton bound to an interface fluctuation quantum dot and a single photon occupying a single mode of the electromagnetic field. The near hemispherical nature of the optical cavity provides for small mode volumes and exhibits large solid angle, non-paraxial modes.

1.2 Context

This research takes place in the subfield of quantum optics referred to as cavity quantum electrodynamics (CQED). Generally, CQED involves the use of optical resonators (i.e. resonant cavities) to modify the nature of the interactions between the electromagnetic field and a material system.

One of the first predictions of what is now commonly viewed as a CQED effect (the Purcell effect) did not involve a cavity at all. It was a prediction made regarding nuclear magnetic resonance (NMR) systems. In a 1946 abstract, E. M.

Purcell predicted that nuclear spins coupled to a resonant electronic circuit would experience an enhanced spontaneous emission rate [52]. The emitter in Purcell's scheme was a nuclear spin in a magnetic field while in contemporary CQED it is quite often an atom. Of course, a two-level system may be used as an idealized model for both a simple atom with one valence electron and a nuclear spin in a DC magnetic field. Consequently, we naturally find many common features in NMR and quantum optics.

Much later, in 1981, inhibited spontaneous emission was also predicted [36]. Both of these phenomena (inhibition and enhancement of spontaneous emission) occur in a regime well described by perturbation theory. Both correspond to a general modification of the emission rate due to modification of the density of available output states and henceforth I will refer to both phenomena as simply the Purcell effect, in accordance with common parlance. The Purcell effect can be understood as a straightforward application of Fermi's golden rule. The Purcell effect was observed first in superconducting (niobium) microwave cavities [25]. Other experiments with a variety of atoms and cavity configurations followed [32, 29, 43, 30, 46].

The Purcell effect arises due to an incoherent interaction between the electric field inside of the cavity and the optical emitter. Changes in lifetime or energy shifts [30] may be observed in this regime but not phase dependent phenomena. In

order to observe quantum interference the dynamics must enter a regime of strong coupling in which the two systems evolve in time coherently.

Roughly, the strong coupling regime corresponds to situations in which the intracavity mode coupling to the material emitter is greater than any other (environmental) interactions. A consequence of this is that the differential equations for the time evolution of the system exhibit complex eigenvalues and the interacting systems behave analogously to classical, coupled oscillators: The time evolution can concisely be described in terms of normal-modes, which are each marked by a shared frequency.

The rationale for using microcavities in CQED becomes obvious when the relationship between electromagnetic energy and volume is considered:

$$\mathcal{E} = \frac{1}{2} \int_V d\tau \left(\epsilon_0 E^2 + \frac{1}{\mu_0} B^2 \right).$$

If energy is held constant, then fields of arbitrary intensity (squared modulus) can be produced by confining the energy to a small enough volume (i.e. to keep the value of the integral constant while integrating over a tiny volume the values of E^2 and B^2 have to increase by an appropriate amount over that volume). This explains the ubiquity of microcavities or even nanocavities in experiments that seek to observe strong coupling. In order to observe a coherent coupling between interacting systems it is necessary to make the interaction channel between the

two systems stronger than any other interactions with external degrees of freedom (i.e. losses). The interaction may be made stronger by confining the field to a small volume.

1.3 Motivation

This work shares many of the same motivations as the atomic CQED experiments. Namely, that strong coupling in CQED leads to inter-system coherence and entanglement and this can be used as a resource in the field of quantum information. Two obvious connections are to quantum computing and quantum key distribution.

A pair of quantum dots coupled to a microcavity has been shown to be a potential physical system for instantiation of a quantum logic gate [14, 48]. In this scheme, dopants provide for excess electrons or holes (depending on whether the dopant is n-type or p-type). These excess charge carriers end up confined to the quantum dots and the ground state of the dots will be a degenerate pair of states corresponding to the two components of spin along a particular axis. A qubit encoded in the spin of this trapped particle will enjoy much longer coherence times than those based on properties of excitons.

This spin may be used as a qubit. Quantum conditional logic may be obtained via dynamics that involve charged exciton (trion) states. For the case of an n-doped sample, in which the trapped spin belongs to an electron, the transition to a trion state is allowed only for the case that the second electron's spin is

opposite to the first electron's spin state — otherwise the Pauli exclusion principle prohibits the transition. This mechanism provides for a way to build a (two qubit) quantum controlled phase gate, an important building block in quantum computer architecture.

If neighboring quantum dots are brought into the trion state the exchange interaction will dominate the unitary time evolution and there will be a collective phase accumulation for the two dots. Only one particular input state will be excited to a trion-trion state by a given (circularly polarized) π -pulse. This produces a conditional phase shift controlled by the logical values of the input qubits.

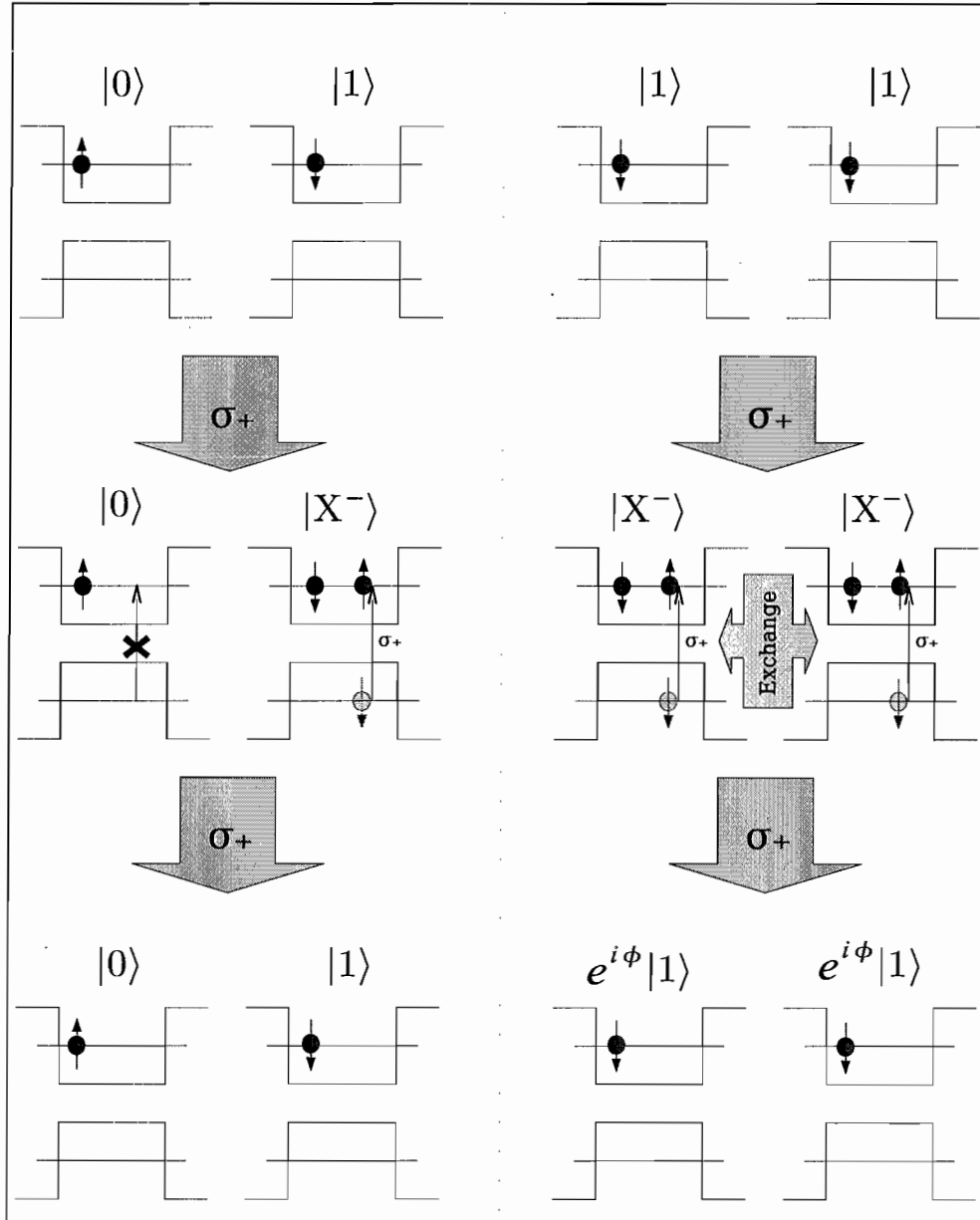


FIGURE 1.1: A QCPG scheme based on trion-trion interactions [48]. A pair of quantum dots is depicted on each side of the dotted line. The pair on the left side is in an input state $|0\rangle|1\rangle$ while the pair on the right side is in the input state $|1\rangle|1\rangle$. A π -pulse of right-hand circularly polarized light is applied in both cases. The quantum dot whose spin initially corresponds to a logical value of $|0\rangle$ cannot be excited to a trion state because of Pauli blocking. Each of the other dots allows the transition to a $|X^- \rangle$ trion state. The pair of quantum dots on the right hand side now accumulates phase due to an exciton-exciton exchange interaction. Finally, another π -pulse is used to bring the quantum dots back to the initial state. The QCPG has mapped $|1\rangle|1\rangle \rightarrow e^{i\phi}|1\rangle|1\rangle$, while mapping any other input state back to itself.

After unitary time evolution to build up phase on the pair of trions, another pulse is used to return both dots to the ground state. On an appropriate time scale, the phase due to unitary time evolution will be small on each input qubit state except for $|11\rangle$. In the limit that this phase accumulation is negligible, it may be seen that the entire process, beginning and ending with the quantum dots in their ground state, may be expressed in the ordered basis $\{|00\rangle, |01\rangle, |10\rangle, |11\rangle\}$ of qubits as

$$QCPG = \begin{bmatrix} 1 & 0 & 0 & 0 \\ 0 & 1 & 0 & 0 \\ 0 & 0 & 1 & 0 \\ 0 & 0 & 0 & e^{i\phi} \end{bmatrix}.$$

The technique of molecular-beam epitaxy will enable one to grow two quantum wells (QWs) with a several-nanometer separation, with a large enough barrier potential to prevent electron tunneling, where interface fluctuation quantum dots (IFQDs) formed in each QW are each doped with an excess electron¹.

Another important application of such strongly coupled cavity-QD systems is the deterministic generation of single-photons [38, 35, 45, 13] or of polarization-entangled photon pairs on demand [55].

The cavity design should also lend itself to applications in atomic quantum optics [42] as well as semiconductor optics [33] and seems ideally suited to test

¹The scheme, as presented, relies on circularly polarized optical transitions, so use of IFQDs would necessitate the use of a strong magnetic field to satisfy this.

certain recent predictions about non-paraxial modes [19, 18] that will be discussed in the next chapter.

The scheme by Stace, Milburn and Barnes utilizes decay from the biexciton state of an asymmetric quantum dot [55], such as an IFQD. Whereas the two photon cascade emitted from the biexciton state of asymmetric quantum dots (QDs) is generally entangled in both frequency and polarization, a properly designed cavity acts to erase the “which path” information and causes the pair of emitted photons to be entangled in polarization only. This is advantageous, from an experimental point of view, because polarizations can be manipulated with linear optics.

The cavity also acts to collect the biexciton emission into a pair of adjacent, longitudinal modes with the same transverse, spatial profile. Thus, the biexciton emission may be collected (primarily) into a single spatial mode, governed by the geometry of the optical cavity. This provides much higher efficiency than attempting to collect light emitted into free space.

The achievement of either a deterministic single-photon source [38, 35, 45, 11] or a source of entangled photons would help to enable an optical scheme for performing quantum computations — linear optical quantum computing (LOQC) [37]. In turn, a single-photon source is a valuable resource for schemes such as Bennett and Brassard, 1984 (BB84), which rely on a source of single photons.

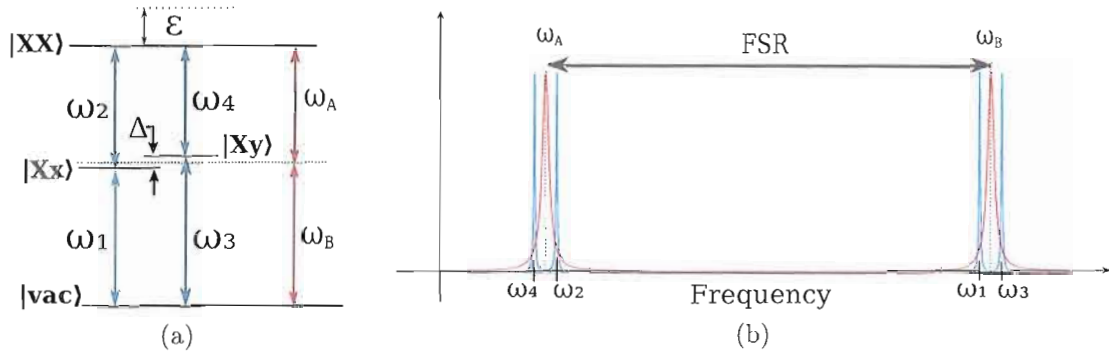


FIGURE 1.2: Entangled photon pairs from a biexciton coupling to cavity. This diagram depicts the proposed setup in [55]. The energy levels of the ground state biexciton and the ground state excitons in an asymmetric quantum dot are shown in (a). The frequencies of quantum dot transitions are shown in blue. The frequencies of two different cavity modes separated by one FSR are shown in red. The anisotropy splitting is labeled by Δ and is on the order of tens of μeV , while the biexciton binding energy (labeled by ϵ) is on the order of several meV . The biexciton emission spectrum is shown in (b) in blue. The red trace shows the location of the cavity modes with respect to the QD transitions.

The ability to produce entangled photon pairs enables techniques such as quantum teleportation [60] or entanglement swapping [47]. The ability to supply entangled photon pairs rather than single photons is also known to reduce the resource requirements in LOQC.

Such sources have wide applications in the emerging field of quantum information science [4]. This is particularly true for quantum cryptography, in which an essential element of secure quantum key distribution (QKD) is an optical source emitting a train of pulses that contain one and only one photon [2]. For example, a source having zero probability for generating two or more photons in a pulse and greater than 20% probability of generating one photon would lead to a great advance in QKD in daylight through the atmosphere [31, 54, 49].

Solid-state emitters have certain distinguishing advantages over atoms and molecules. In particular, their lack of mobility removes the requirement for robust trapping and cooling. The population of emitters in a particular solid sample has to do with structural peculiarities of the crystal (as opposed to what one might call structural peculiarities of free space). Due to the rigid lattice of a crystal, the structural defects have well-defined positions.

Accordingly, when dealing with solid state emitters the number of emitters in a particular volume of the crystal is fixed ². In contrast, an atomic beam intersecting a cavity will typically exhibit shot noise. It is exceedingly difficult to keep one and only one atom at a well-defined position inside of a micro-cavity. Using structural defects such as QDs takes care of this problem, though at the cost of well-defined, consistent properties. Delivering single atoms to a microcavity requires exacting technical expertise. From an experimental standpoint, absorbing heat from a crystal into a cold finger is trivial by comparison.

The emitters of choice for this work are interface fluctuation quantum dots (IFQDs). They make a good choice for CQED experiments due to very large dipole moments [5, 44]. In fact two of three first indications of single quantum dot (SQD) CQED strong coupling [61, 53, 50] involved IFQDs; [53] employed self-assembled InAs QDs.

²This assumes stable operating conditions. The number of available bound states depends on a particle's energy compared to the binding energy of a given potential. Factors that affect either of these two quantities will therefore have an effect on the number of transitions that can be observed. If the particle's energy is high enough no bound states are accessible and there will be no observable emitter.

The primary difference in this work, compared with those just cited, is the type of cavity. While successful efforts have used microdiscs, micropillars and photonic crystal nanocavities, this work combines an IFQD with an external, near-hemispherical cavity. External cavities provide certain advantages, such as the ability to scan the waist of the cavity mode in search of suitable emitters. Independent detuning of cavity frequency compared to emitter frequency is also possible, in contrast to monolithic structures where temperature tuning is often the only technique available. Temperature tuning can be undesirable because in addition to thermal expansion, temperature also determines the population of phonons present, a chief source of dissipation and dephasing in solid-state systems.

The external cavity allows a given emitter to be positioned at a region of maximum field strength while also providing for independent tuning of cavity frequency to match the emitter's transition frequency. This also provides for clearer examination of temperature dependence of the coupled system since the detuning may be held fixed while tuning the temperature.

The near-hemispherical geometry of the cavity provides for a very small (close to the diffraction limit) mode waist. This means a small mode volume for a given cavity length. A mirror with a radius of curvature of $50\ \mu\text{m}$ should yield a mode volume of less than about $50\ \mu\text{m}^3$ — a rough estimate based on an approximate spot size at the flat mirror multiplied by the length of the optical cavity.

As the cavity is shortened, the radius of the mode waist increases and the divergence angle decreases. Eventually, the paraxial limit is reached and the mode may be treated as a Gaussian beam. In this situation we would expect a mode volume of $\frac{\pi}{4}w_0^2 \cdot L$, as calculated in appendix B. The non-paraxial nature of the modes under the near-hemispherical conditions) investigated here defies a treatment in terms of Gaussian beams.

The external microcavity system we have built also provides a nearly ideal environment for assessing certain predictions like mixing of nearly degenerate modes as predicted in [19]. Mode mixing is attended by non-simple polarization distribution – at times characterized by mixtures of circular and linear polarization at different transverse locations within a given mode.

1.4 Outline

Here, a brief sketch of the structure of the succeeding chapters is provided.

Chapter 2 will cover theoretical considerations for this experiment. First, a description of the IFQDs is provided, along with a justification for treating them as a two-level system. Following this, the two levels of interest will be used to express a Hamiltonian in terms of pseudo-spin operators.

The quantization of the field follows this. Due to the absence of analytic solutions for the near-hemispherical cavity's non-paraxial modes, the particular form of the quantized field will not be treated explicitly. A quantization of the

paraxial Gaussian fundamental mode is carried out in appendix B. This provides guidance for the relationship between the classical fields and the quantum operators invoked in the theoretical analysis and helps make clear the relationship between the parameter V_{eff} that appears in the quantum field operators and the amplitude of the field at the position of interest.

A treatment of the dipole interaction follows this and the pieces are assembled into the familiar Jaynes-Cummings Hamiltonian.

The remainder of the chapter involves methods for including dissipation via interactions with unmeasurable reservoirs and coupling to an input and output mode so that a steady-state transmission spectrum can be calculated. The chapter ends with some numerical results pertaining to non-paraxial mode properties for cavities with configurations similar to ours. These results come from both Murray Holland's group at University of Colorado and Jens Nöckel's group here at the University of Oregon.

Chapter 3 will discuss the design and construction of the microcavity system. It will account for the equipment and designs used and remark about suitability for achieving the stated goals. It will briefly describe the processing of curved micromirrors and the basic design of the semiconductor DBRs used to form the cavity boundaries. This work was done in collaboration with Guoqiang Cui in the Raymer Lab and Hyatt Gibbs and Galina Khitrova at the University of Arizona, and was published in [12].

Chapter 4 will discuss the experimental work. It begins with a discussion of the observed modes and steps taken to mode-match into the desired mode.

The next topic is intra-cavity photoluminescence (PL) of the dots, to observe the presence of IFQDs and determine the orientation of the crystal axes by measuring polarized PL.

Finally, an array of transmission measurements under various conditions will be presented. Data was taken for two different DBR samples. Each sample was measured at various transverse positions, various cavity lengths and with various ranges of probe wavelength (covered by three different probe lasers).

Chapter 5 will summarize the results of the experiment and assess possible improvements to this work. Ideas for future research and directions will also be discussed.

CHAPTER II

THEORY

2.1 Overview

This chapter's goals are to provide a theoretical framework for analyzing the data obtained in the experiment. At first, some theory about the quantum dots used in this work will be presented. Later sections will provide a theory for the interaction of a two-level system with a single mode of the electromagnetic field. In particular, the Hamiltonian for an analog closed system is developed. Next, the Hamiltonian will be diagonalized (i.e. transformed to a dressed-state basis) to provide for basic predictions of vacuum Rabi splitting. Finally, coupling to electromagnetic and vibrational reservoirs will be included to provide a more realistic account of the expected dynamics.

2.2 Theoretical Considerations for IFQDs

The purpose of this section is to provide a theoretical description of the emitters to be used in this work. The emitter used here will be described as a two-level system. The two energy levels correspond to vacuum and a ground-state exciton

in the exciton basis. To justify this description, a brief account of the properties of these dots will be provided. The emitters of interest in this work are IFQDs. They are shallow (weak lateral confinement), anisotropic GaAs/Al_xGa_{1-x}As quantum dots that have large lateral extent and thus exhibit a large dipole moment, making them attractive emitters for CQED strong coupling.

2.2.1 Confinement and Light Holes

Quantum dots are spatially localized regions of semiconductor with lower energy than their surroundings. They are characterized by confinement in all three dimensions and because of this they may be regarded as quasi-zero-dimensional systems.

Excitations in undoped semiconductor systems result from the promotion of an electron in a valence band to the conduction band. In the neighborhood of the Γ -point, where $|k| = 0$, there are two degenerate valence bands in bulk GaAs. The two valence bands have band edges with different curvatures, leading to different effective mass for the holes left by promoting an electron to the conduction band. Holes in the higher-curvature band have a larger smaller effective mass and are called heavy holes, while those in the lower-curvature band have smaller effective mass and are called light holes.

In confined systems, such as quantum wells and QDs, the energy of the light hole is much higher than the heavy hole and it becomes decoupled. As mentioned in [23], for well widths narrower than around 12 nm the light-hole exciton overlaps

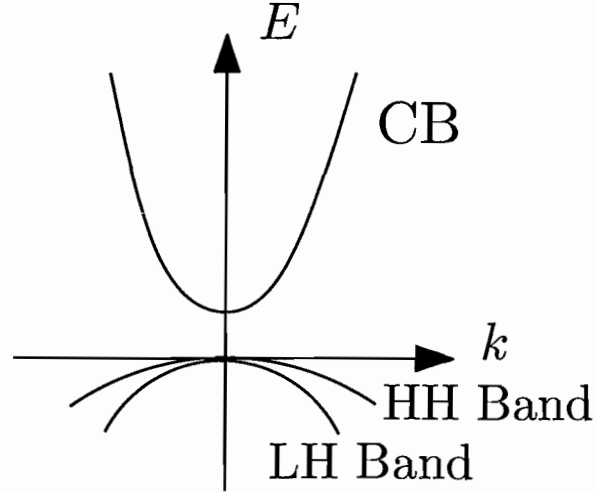


FIGURE 2.1: Bulk GaAs band structure near Γ . The two degenerate valence bands are shown for bulk GaAs. Another split-off band is not shown because it occurs at a lower energy; adapted from [15].

the continuum states of the heavy-hole exciton. Also, calculations of lateral barrier height for narrow GaAs IFQDs are roughly of the order of 16 meV [58], whereas the light-hole exciton is generally tens of meV higher in energy than the heavy-hole exciton¹. This means that for the IFQDs used in this work, which occur in QWs with widths of 3.86 nm, we can consider the exciton ground states as being almost purely bound states of electrons and heavy holes. It suggests that mixing between heavy-holes and light holes only occurs for continuum states of heavy holes (i.e. holes that are no longer bound by the shallow lateral potential due to the monolayer fluctuations). Therefore, we assume that the exciton ground states are

¹The barrier height is actually smaller than the thermal energy at room temperature, which is about 26 meV. This means that at room temperature excitons have higher energy than the lateral potential and there are effectively no quantum dots.

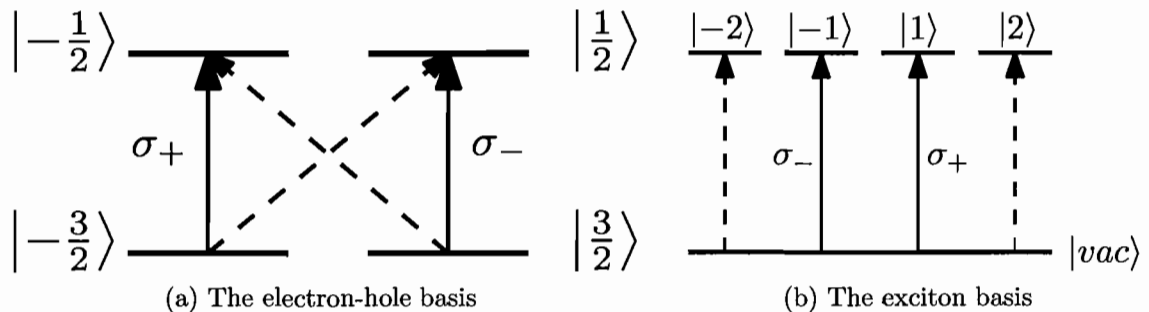


FIGURE 2.2: Selection rules for QDs in two bases. Selection rules show dipole-allowed transitions in a description involving electrons and heavy holes (a) or excitons (b). The solid arrows indicate dipole-allowed transitions.

bound states of a heavy hole and an electron. There are four possible such bound states and there exists an underlying four-fold degeneracy [1, 51, 40].

2.2.2 Selection Rules and the Exchange Interaction

The four possible pairings of the electron with the heavy hole may be written as $|-3/2\rangle_h |-1/2\rangle_e$, $|-3/2\rangle_h |+1/2\rangle_e$, $|+3/2\rangle_h |-1/2\rangle_e$ and $|+3/2\rangle_h |+1/2\rangle_e$ in the electron-hole basis.

Alternatively, it is possible to label these combinations in terms of total z -component of spin and talk about excitons rather than electrons and holes. In this case, the same four bound states may be labeled, respectively, $|-2\rangle$, $|-1\rangle$, $|+1\rangle$ and $|+2\rangle$.

The $|+1\rangle$ and $|-1\rangle$ states are referred to as the spin-up and spin-down bright excitons. In turn, $|+2\rangle$ and $|-2\rangle$ will be the spin-up and spin-down dark excitons. One of the two standard approaches for dealing with the exchange interaction is the Ivchenko-Pikus representation in which the state of the hole $|J_z = \pm 3/2\rangle$ is represented by a pseudospin, $|S_{h,z} = \mp 1/2\rangle$.

The Hamiltonian for the electron-hole exchange interaction may then be parametrized in terms of the observed energy splittings of an anisotropic quantum dot, as in [21]:

$$\hat{\mathcal{H}}_{\text{exch}} = \frac{\delta_0}{2} \hat{\sigma}_z^e \otimes \hat{\sigma}_z^h + \frac{\delta_b}{4} (\hat{\sigma}_x^e \otimes \hat{\sigma}_x^h - \hat{\sigma}_y^e \otimes \hat{\sigma}_y^h) + \frac{\delta_d}{4} (\hat{\sigma}_x^e \otimes \hat{\sigma}_x^h + \hat{\sigma}_y^e \otimes \hat{\sigma}_y^h) \quad (2.1)$$

where δ_0 is the energy difference between the dark and bright excitons, δ_b is the energy splitting of the bright exciton due to the long range exchange interaction, and δ_d is the energy splitting of the dark exciton states. The matrix in the ordered basis of $|1\rangle$, $|-1\rangle$, $|2\rangle$ and $|-2\rangle$ is:

$$[\hat{\mathcal{H}}_{ex}] = \frac{1}{2} \begin{bmatrix} \delta_0 & \delta_b & 0 & 0 \\ \delta_b & \delta_0 & 0 & 0 \\ 0 & 0 & -\delta_0 & \delta_d \\ 0 & 0 & \delta_d & -\delta_0 \end{bmatrix} \quad (2.2)$$

This immediately indicates the decoupling of the $|\pm 1\rangle$ excitons from the $|\pm 2\rangle$ excitons. The eigenstates are again determined by finding the vectors that diagonalize the Hamiltonian.

Symmetric Quantum Dots

In spherical (or axisymmetric) dots there is rotational invariance in 2 (or 1) angles. The azimuthal invariance of the Hamiltonian implies a conserved quantity. Noether's theorem implies a conservation of angular momentum in this case. The selection rules for such dots are depicted in figure 2.3.

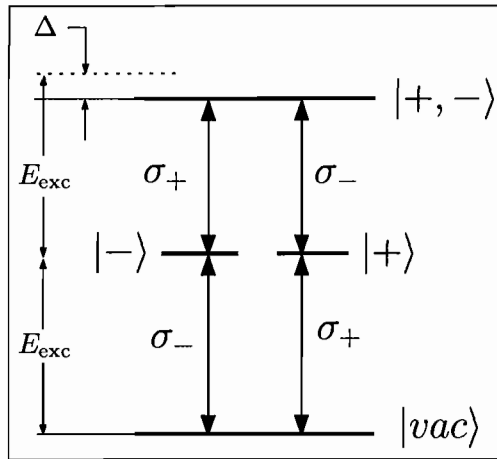


FIGURE 2.3: Selection rules — axisymmetric QD. The dipole-allowed selection rules for an axisymmetric QD are shown

The degeneracy between the dark and bright excitons is lifted by the short-range exchange interaction. The long-range interaction is negligible due to transverse symmetry and $\delta_b \approx 0$. The bright excitons, thus occupy a degenerate doublet. The exciton states are eigenstates of total angular momentum and the angular momentum projection along the z- axis. The $|+1\rangle$ and $| -1\rangle$ excitons are generated by absorption of a left-hand circular polarized photon and a right-hand circular polarized photon, respectively. They must, respectively, involve an invocation of angular momentum ladder operators applied to the vacuum state.

More concretely, as stated in [21], the Bloch functions in a quantum well have symmetries like this:

$$|+1\rangle = (|X + iY\rangle_h \uparrow)(|s\rangle_e \downarrow) \quad (2.3)$$

$$|-1\rangle = (|X - iY\rangle_h \downarrow)(|s\rangle_e \uparrow). \quad (2.4)$$

This represents the bright excitons as bound states of two spin-1/2 particles aligned anti-parallel to each other. The excess angular momentum appears as an orbital angular momentum portion of the heavy-hole pseudospin in this representation. The heavy-hole kets in the above expressions are immediately reminiscent of the form of angular momentum ladder operators and also of circularly polarized light [34].

Asymmetric Quantum Dots

For asymmetric (anisotropic) QDs (such as IFQDs) the rotational invariance is destroyed and angular momentum is no longer a good quantum number. The new selection rules will be described briefly. The long-range exchange interaction acquires a finite effect and leads to eigenstates which are totally symmetric and anti-symmetric combinations of the angular momentum eigenstates.



FIGURE 2.4: Anisotropic exchange splitting. This figure shows the level diagram with and without the exchange interaction for spin-1 excitons.

Working with the $|\pm 1\rangle$ manifold diagonalize the matrix in the usual way. In this situation δ_1 is nonzero.

$$\begin{aligned} \begin{vmatrix} \delta_0 - \lambda & \delta_b \\ \delta_b & \delta_0 - \lambda \end{vmatrix} &= (\delta_0 - \lambda)^2 - \delta_1^2 = 0 \\ \Rightarrow \lambda^2 - 2\lambda\delta_0 + (\delta_0^2 - \delta_1^2) &= 0 \\ \Rightarrow \lambda &= \frac{2\delta_0 \pm \sqrt{4\delta_0^2 - 4(\delta_0^2 - \delta_1^2)}}{2} \\ \lambda &= \delta_0 \pm \delta_1 \end{aligned}$$

The eigenvectors corresponding to $\lambda = \delta_0 \pm \delta_1$ are $|v\rangle = \frac{e^{i\phi}}{2} (|1\rangle \mp |-1\rangle)$.

Taking the positive and negative combinations of (2.3) and (2.4) provides for

$$\begin{aligned} |X\rangle &= \frac{e^{i\phi}}{2} (|1\rangle + |-1\rangle) \\ |Y\rangle &= -i\frac{e^{i\phi}}{2} (|1\rangle - |-1\rangle) \end{aligned}$$

The directions X and Y tend to correspond with the $[110]$ and $[\bar{1}10]$, respectively for GaAs IFQDs. The excitons are dipole active along these directions.

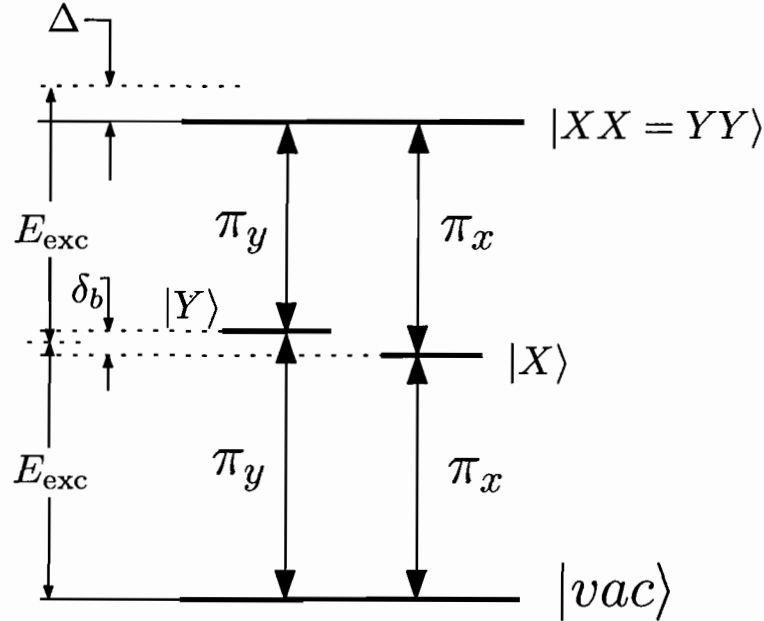


FIGURE 2.5: Selection rules — asymmetric QD. This figure shows the linear polarized optical transitions connecting the excitons to the biexciton state and the vacuum state. The bright-exciton splitting is shown here as δ_b . The exciton binding energy is labeled as Δ .

Taking the above together with (2.3) and (2.4) it is evident that the spin states of the electron are mixed together and also that the polarization of the absorbed or emitted photons must be linear. Experimentally observed splittings are well described by this theory, as shown in [22, 39, 24].

So, due to the confinement and shallowness of these dots, the excitons may be thought of as combinations of only the heavy hole and the electron. Short-range exchange interactions split the possible exciton states into dark states and bright states. Due to anisotropy, the degeneracy of the bright doublet is lifted and the selection rules for these transitions require linear polarization of the light field.

Going forward from here, a simple two-level system with dipole moment pointing along the [110] direction of the crystal will be used to model the pair of states corresponding to the vacuum state and the ground-state exciton of an IFQD. Because the experiment seeks to operate in the single excitation limit, it is not necessary to distinguish carefully between whether the excitons have bosonic, fermionic or mixed characteristics: Differences between fermions and excitons only become evident when multiple excitations are confronted and effects like exclusion or bunching have a chance to manifest.

2.3 The Jaynes-Cummings Hamiltonian

In this section, the basic Jaynes-Cummings Hamiltonian is developed. This system consists of a single, quantized mode of the electromagnetic field coupled via electric dipole interaction to a single two-level system. The Hamiltonians for the two non-interacting systems will be developed followed by the interaction Hamiltonian. Finally, the Hamiltonian will be written in a simplified form.

2.3.1 Two-level Hamiltonian

The Hamiltonian for the two energy levels will be expressed in terms of pseudo-spin operators (Pauli matrices).

Consider a two-level system with energies E_a and E_b . Let the difference of the two energies be given by

$$E_a - E_b = \hbar\omega. \tag{2.5}$$

The Hilbert space is spanned by two states labeled by $|a\rangle$ and $|b\rangle$. In this case, the lower level $|b\rangle$ corresponds to the vacuum state of an IFQD and the $|a\rangle$ corresponds to the ground state exciton. We may calculate the matrix elements of the 2-level Hamiltonian by exploiting the two energy eigenstates,

$$\hat{\mathcal{H}}_{2\text{-level}} |a\rangle = E_a |a\rangle \quad (2.6)$$

$$\hat{\mathcal{H}}_{2\text{-level}} |b\rangle = E_b |b\rangle. \quad (2.7)$$

This allows us to write down the atomic Hamiltonian by calculating its matrix elements. Meanwhile, completeness of our basis ensures that

$$|a\rangle \langle a| + |b\rangle \langle b| = \hat{I}. \quad (2.8)$$

This expression for the identity permits the following description of the 2-level Hamiltonian. Inserting two complete sets we obtain:

$$\begin{aligned} \hat{\mathcal{H}}_{2\text{-level}} &= \sum_{i,j \in \{a,b\}} |i\rangle \langle i| \hat{\mathcal{H}}_{2\text{-level}} |j\rangle \langle j| \\ &= \sum_{i,j \in \{a,b\}} |i\rangle \langle j| \langle i| \hat{\mathcal{H}}_{2\text{-level}} |j\rangle \\ &= \sum_{i,j \in \{a,b\}} |i\rangle \langle j| \overbrace{\langle i|j\rangle}^{\delta_{ij}} E_j \\ &= \sum_{i \in \{a,b\}} |i\rangle \langle i| E_i. \end{aligned} \quad (2.9)$$

The Hamiltonian may then be written explicitly in the basis of energy eigenstates as:

$$\hat{\mathcal{H}}_{2\text{-level}} = E_a |a\rangle \langle a| + E_b |b\rangle \langle b|. \quad (2.10)$$

This is a completely general Hamiltonian for a two-level system. It merely consists of projection operators into the two possible states with the corresponding energies as coefficients.

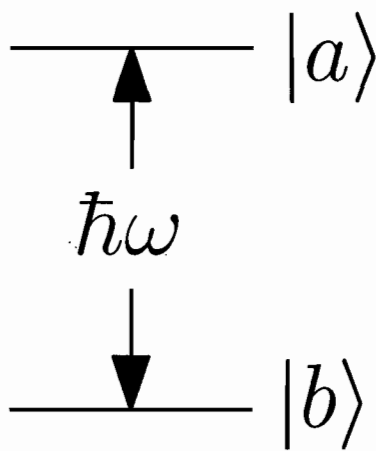


FIGURE 2.6: 2-level system energies. This shows the two energy levels in question with given energy difference

This general two-level system is mathematically equivalent to a non-relativistic spin-1/2 particle (i.e. the dynamics may be formulated in terms of Pauli pseudospin operators). As an aside: A concrete mapping to the Pauli matrices is obtained by choosing a particular map of our state vectors into an orthogonal pair of column vectors. This map generates a set of 2×2 matrices which are identically the Pauli matrices. For the moment, it is not necessary to choose such a map, so the matter will be left for later. Suffice it to say that the

dynamics may suitably be described by operators in the group $SU(2)$.

Without loss of generality, we may define a set of operators by taking outer products of our basis states:

$$\hat{S}_+ \equiv |a\rangle \langle b| \quad (2.11)$$

$$\hat{S}_- \equiv |b\rangle \langle a| \quad (2.12)$$

$$\hat{\sigma}_z \equiv |a\rangle \langle a| - |b\rangle \langle b|. \quad (2.13)$$

The two-level Hamiltonian can be simplified significantly from (2.10). By applying an appropriate additive identity, the above may be cast into a form consistent with the Pauli description.

$$\begin{aligned} \hat{\mathcal{H}}_{2\text{-level}} &= E_a |a\rangle \langle a| + E_b |b\rangle \langle b| \\ &= \frac{1}{2} (E_a |a\rangle \langle a| + E_b |b\rangle \langle b|) + \frac{1}{2} (E_a |a\rangle \langle a| + E_b |b\rangle \langle b|) \\ &\quad - \frac{1}{2} (E_b |a\rangle \langle a| - E_a |b\rangle \langle b|) + \frac{1}{2} (E_b |a\rangle \langle a| - E_a |b\rangle \langle b|) \\ &= \frac{1}{2} (E_a - E_b) (|a\rangle \langle a| - |b\rangle \langle b|) + \frac{1}{2} (E_a + E_b) (|a\rangle \langle a| + |b\rangle \langle b|) \\ &= \frac{1}{2} (E_a - E_b) \hat{\sigma}_z + \frac{1}{2} (E_a + E_b) \hat{\mathbb{I}}. \end{aligned} \quad (2.14)$$

On the fourth line (2.13) and (2.8) have been used.

To study the dynamics of the system it is sufficient to look at how the energy scales. The constant energy term (proportional to the identity operator) plays no role in determining the dynamics of the system. It is safe to ignore it for now. It can always be added at a later point if it becomes convenient to do so. At this

point, retain the part proportional to the Pauli operator. Using (2.5) gives the following atomic contribution to the energy:

$$\boxed{\hat{\mathcal{H}}_{2\text{-level}} = \frac{1}{2} \hbar \omega \hat{\sigma}_z.} \quad (2.15)$$

2.3.2 Field Hamiltonian

Appendix B reviews the theory of a paraxial cavity. In particular, the forms of the Hamiltonian and the quantized electric field operator are found, as well as the mode volume for a paraxial Gaussian mode of the cavity. The treatment of the field in that appendix rests heavily on the paraxial approximation, whereas a hemispherical cavity has a diffraction-limited spot-size and large solid angle, and so is not described well by that approximation.

Departing from the paraxial regime means that approximations like $\sin \theta \approx \theta$, $\tan \theta \approx \theta$, and $\cos \theta \approx 1$ are no longer justified. In other words, it becomes necessary to go beyond first-order in the theory. The standard trick of separation of transverse and longitudinal variables fails because we can no longer make the above approximations.

The lack of an analytical framework for characterizing the solutions to Maxwell's equations under such conditions pushes research in the direction of numerical solutions. Numerical investigations into cavities of similar geometry to the ones considered here [20] have led to predictions of novel modes whose behavior depends

intimately on the vector nature of light [18] (i.e. the spatial distribution of the amplitude of the modes is not independent of the spatial distribution of the polarization of the modes).

Interestingly, such studies have also yielded predictions of optical spin-orbit coupling due to mode mixing induced by polarization-dependent phase shifts (upon reflection from layers in a Bragg stack) that extend arbitrarily far into the paraxial regime [19].

Nevertheless, while non-paraxiality may lead to certain novel behaviors not easily described by analytic methods, it does not affect the expression for the energy density of an electromagnetic field; nor does it change the fact that $\mathbf{E}(\mathbf{r}, t)$ lies in the plane of the QW. We proceed by quantizing the classical electromagnetic Hamiltonian.

Classical Field

It is possible, for the case of paraxial modes (see appendix B) to carry out the necessary integration of the mode function explicitly to determine the mode volume. In this case, without an analytic representation of the mode function, the mode volume will not be explicitly determined.

The plan of attack here is to write down the classical energy and show that it (as in the paraxial regime) has the form of a harmonic oscillator. This classical field

will then be quantized by canonical quantization. The quantized electric field will be used later to write down the interaction Hamiltonian².

$$H = \frac{1}{2} \int_V d^3r \left(\epsilon_0 \mathbf{E}^2 + \frac{1}{\mu_0} \mathbf{B}^2 \right). \quad (2.16)$$

Of course, the fields must obey the source-free, vacuum Maxwell's equations.

Thus, each of the fields must satisfy a wave equation.

$$\nabla^2 \mathbf{E}(\mathbf{r}, t) = \frac{1}{c^2} \frac{\partial^2}{\partial t^2} \mathbf{E}(\mathbf{r}, t) \quad (2.17)$$

$$\nabla^2 \mathbf{B}(\mathbf{r}, t) = \frac{1}{c^2} \frac{\partial^2}{\partial t^2} \mathbf{B}(\mathbf{r}, t) \quad (2.18)$$

The time dependent part of the equations may easily be separated from the vectorial, space dependent part. Working with the electric field, define it to be a product of a vectorial function of a position vector with a scalar function of time.

Let

$$\mathbf{E}(\mathbf{r}, t) = \mathbf{R}(\mathbf{r}) \cdot T(t). \quad (2.19)$$

²In this section boldface denotes vectors in \mathbb{R}^3 , caret denotes a unit vector in \mathbb{R}^3 .

Then,

$$\begin{aligned}\nabla^2 \mathbf{E}(\mathbf{r}, t) &= \frac{1}{c^2} \frac{\partial^2}{\partial t^2} \mathbf{E}(\mathbf{r}, t) \\ \Rightarrow \nabla^2 \mathbf{R}(\mathbf{r}) \cdot T(t) &= \frac{1}{c^2} \frac{\partial^2}{\partial t^2} \mathbf{R}(\mathbf{r}) \cdot T(t) \\ \Rightarrow T(t) \nabla^2 \mathbf{R}(\mathbf{r}) &= \frac{\mathbf{R}(\mathbf{r})}{c^2} \ddot{T}(t)\end{aligned}$$

Now scalar multiply both sides from the left by $\hat{R}(\mathbf{r})/|\mathbf{R}(\mathbf{r})| \cdot T(t)$ (where \hat{R} denotes a spatial unit vector pointing along \mathbf{R}). This provides a separated harmonic equation for the scalar time-dependent function and a seemingly non-separable vector equation.

$$\begin{aligned}\frac{T(t) \hat{R}(\mathbf{r}) \cdot \nabla^2 \mathbf{R}(\mathbf{r})}{|\mathbf{R}(\mathbf{r})| \cdot T(t)} &= \frac{\hat{R}(\mathbf{r}) \cdot \mathbf{R}(\mathbf{r})}{|\mathbf{R}(\mathbf{r})| \cdot c^2 T(t)} \ddot{T}(t) \\ \Rightarrow \frac{\hat{R}(\mathbf{r}) \cdot \nabla^2 \mathbf{R}(\mathbf{r})}{|\mathbf{R}(\mathbf{r})|} &= \frac{1}{c^2 T(t)} \ddot{T}(t) = -k^2\end{aligned}$$

The time dependent function is, therefore, a harmonic function of time and has solutions as given in (B.5). In the absence of a resonator the eigenvalues would generally have a continuous spectrum. In cavity-QED, we may assume the presence of a stable resonant cavity so that the eigenvalue spectrum becomes sharply peaked. It is well known that self-consistency of the modal field in a resonant cavity leads to sharply peaked density of states and the eigenvalues (ω) become bunched about certain discrete values called the resonant frequencies of the cavity.

Additionally, with the small length of the cavities considered in this work, the mode spacing can become quite large and it is not difficult to tune a probe beam to become resonant with only one cavity mode. Henceforth, discussion will concern only one mode at a time. Define $\nu = kc$. Then each mode will be labeled by a particular value of ν and it is reasonable to write

$$T(t) = T_0 e^{-i\nu t}. \quad (2.20)$$

Armed with (2.20) return to the wave equation for the electric field (2.17).

Since the time dependent function has been found take this opportunity to change notation, switching from $\mathbf{R}(\mathbf{r})$ for the vectorial, spatially dependent factor to the clearer $\mathbf{E}(\mathbf{r})$. This provides

$$\begin{aligned} \nabla^2 \mathbf{E}(\mathbf{r}) T_0 e^{-i\nu t} - \frac{\mathbf{E}(\mathbf{r})}{c^2} (-\nu^2) T_0 e^{-i\nu t} &= 0 \\ \Rightarrow \nabla^2 \mathbf{E}(\mathbf{r}) + k^2 \mathbf{E}(\mathbf{r}) &= 0 \end{aligned} \quad (2.21)$$

The vector Helmholtz equation on the last line of (2.21) can be written more simply due to the source free Gauss's Law.

$$\begin{aligned} \nabla^2 \mathbf{E}(\mathbf{r}) + k^2 \mathbf{E}(\mathbf{r}) &= \nabla(\nabla \cdot \mathbf{E}) - \nabla \times (\nabla \times \mathbf{E}(\mathbf{r})) + k^2 \mathbf{E}(\mathbf{r}) \\ &= \nabla \times (\nabla \times \mathbf{E}(\mathbf{r})) + k^2 \mathbf{E}(\mathbf{r}) = 0 \end{aligned}$$

This can plainly be satisfied provided the following expression for the curl of the field holds:

$$\nabla \times \mathbf{E}(\mathbf{r}) = \pm ik\mathbf{E}(\mathbf{r}). \quad (2.22)$$

Now the application of Faraday's Law is straightforward.

$$\frac{\partial}{\partial t}\mathbf{B}(\mathbf{r}, t) = -\nabla \times \mathbf{E}(\mathbf{r}, t) = \mp ik\hat{k} \times \mathbf{E}(\mathbf{r}, t) \quad (2.23)$$

Differentiate (2.23) with respect to time to achieve the magnetic field's second time derivative.

$$\begin{aligned} \ddot{\mathbf{B}}(\mathbf{r}, t) &= \mp ik\hat{k} \times \dot{\mathbf{E}}(\mathbf{r}, t) = -\nu^2\mathbf{B}(\mathbf{r}, t) \\ \Rightarrow \mathbf{B}(\mathbf{r}, t) &= -\frac{1}{\nu^2}(\mp ik\hat{k} \times \dot{\mathbf{E}}(\mathbf{r}, t)) \end{aligned}$$

Now, that the relationship between the fields has been determined the electromagnetic energy of the intracavity field may be written down. The electromagnetic energy, as given by (2.16), is

$$\begin{aligned} H &= \frac{1}{2} \int_V d^3r \left(\epsilon_0 |\mathbf{E}(\mathbf{r})|^2 T^2(t) + \frac{1}{\mu_0} \frac{k^2}{\nu^4} \left| \hat{k} \times \mathbf{E}(\mathbf{r}) \right|^2 \dot{T}^2(t) \right) \\ &= \frac{\epsilon_0}{2} \int_V d^3r \left(|\mathbf{E}(\mathbf{r})|^2 T^2(t) + \frac{1}{\nu^2} \left| \hat{k} \times \mathbf{E}(\mathbf{r}) \right|^2 \dot{T}^2(t) \right) \\ &= \frac{\epsilon_0}{2} \left(T^2(t) + \frac{\dot{T}^2}{\nu^2} \right) \int_V d^3r |\mathbf{E}(\mathbf{r})|^2 \end{aligned} \quad (2.24)$$

Write this in terms of the effective mode volume. Suppose that the field has a uniform intensity everywhere. The effective mode volume is defined so that when it multiplies the uniform intensity, the result is the same as when integrating the varying intensity of the real field over the cavity volume.

$$V_{\text{eff}} \cdot |\mathbf{E}(\mathbf{r}_0)|^2 = \int_V d^3r |\mathbf{E}(\mathbf{r})|^2 \quad (2.25)$$

Combine (2.25) with (2.24) to produce

$$H = \frac{\epsilon_0}{2} \left(T^2(t) + \frac{\dot{T}^2}{\nu^2} \right) \cdot V_{\text{eff}} \cdot |\mathbf{E}(\mathbf{r}_0)|^2.$$

Finally, define a new dynamical variable, which is just a scaled version of $T(t)$.

Let

$$q(t) = \sqrt{\frac{\epsilon_0 V_{\text{eff}}}{\nu^2}} |\mathbf{E}(\mathbf{r}_0)| T(t). \quad (2.26)$$

For future consideration, $\mathbf{E}(\mathbf{r}_0)$ may be regarded as the product of a scalar amplitude, a (possibly) position-dependent vector field and a normalized mode function. That is,

$$\mathbf{E}(\mathbf{r}_0) = E_0 u(\mathbf{r}_0) \boldsymbol{\epsilon}(\mathbf{r}_0), \quad (2.27)$$

with the obvious generalization:

$$\mathbf{E}(\mathbf{r}) = E_0 u(\mathbf{r}) \boldsymbol{\epsilon}(\mathbf{r}). \quad (2.28)$$

Due to (2.26) the classical energy is written as follows:

$$H = \frac{1}{2} (\nu^2 q^2 + \dot{q}^2)$$

This is the energy of a classical, harmonic oscillator with unit mass with canonical coordinate q . In this case $p = \dot{q}$ so that

$$H = \frac{1}{2} (\nu^2 q^2 + p^2). \quad (2.29)$$

Quantization of the field

Now, the problem is quantized according to canonical quantization by simply replacing the quantities q , p and H with operators \hat{q} , \hat{p} and $\hat{\mathcal{H}}$. The operators \hat{q} and \hat{p} obey the Heisenberg uncertainty principle:

$$[\hat{q}, \hat{p}] = i\hbar$$

It is usually convenient to express the dynamics in terms of an alternate set of operators: $q, p \rightarrow a, a^\dagger$. Let the new basis be:

$$\hat{a} = \frac{1}{\sqrt{2\hbar\nu}} (\nu\hat{q} + i\hat{p}) \quad (2.30)$$

$$\hat{a}^\dagger = \frac{1}{\sqrt{2\hbar\nu}} (\nu\hat{q} - i\hat{p}). \quad (2.31)$$

This gives, for the inverse transformation:

$$\hat{q} = \sqrt{\frac{\hbar}{2\nu}} (\hat{a} + \hat{a}^\dagger) \quad (2.32)$$

$$\hat{p} = -i\sqrt{\frac{\hbar\nu}{2}} (\hat{a} - \hat{a}^\dagger). \quad (2.33)$$

The new \hat{a} operators obey the following commutation relationship:

$$[\hat{a}, \hat{a}^\dagger] = 1. \quad (2.34)$$

Now we can use the above to re-write the Hamiltonian in the familiar form using the creation (annihilation) operators. These operators generate the familiar ladder of states beginning at the ground state and proceeding, in units of $\hbar\nu$, to infinity. From (B.26) the Hamiltonian is:

$$\begin{aligned} \frac{1}{2} (\nu^2 \hat{q}^2 + \hat{p}^2) &= \frac{1}{2} \frac{\hbar\nu}{2} [(\hat{a} + \hat{a}^\dagger)^2 - (\hat{a} - \hat{a}^\dagger)^2] \\ &= \frac{\hbar\nu}{4} [2(\hat{a}\hat{a}^\dagger + \hat{a}^\dagger\hat{a})] \\ &= \frac{\hbar\nu}{2} [(1 + 2\hat{a}^\dagger\hat{a})] \\ &= \hbar\nu (\hat{a}^\dagger\hat{a} + \frac{1}{2}). \end{aligned}$$

As with the atomic Hamiltonian drop the constant energy term. This gives the form of the Hamiltonian that will be used in the rest of the analysis.

$$\hat{\mathcal{H}}_{\text{Field}} = \hbar\nu \cdot \hat{a}^\dagger \hat{a} \quad (2.35)$$

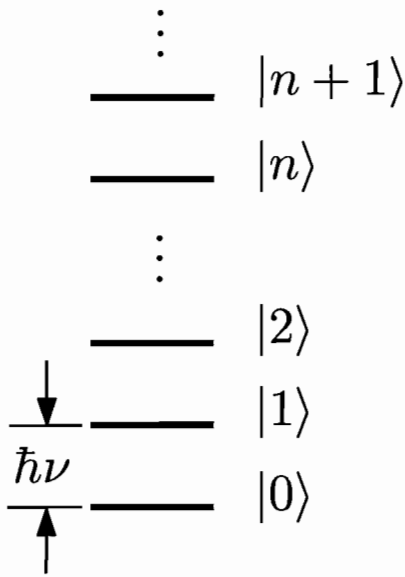


FIGURE 2.7: E/M field energy levels. This shows the ladder of states of the quantum harmonic oscillator.

Finally, write down the electric field operator since it is relevant to the discussion in section 2.3.3, where the interaction of a dipole with the electric field is to be considered. Since the QDs are stationary we can consider the position of the dipole to be fixed at a particular location (\mathbf{r}_0) and thus the effective mode volume can be considered constant.

By (2.27), $|\mathbf{E}(\mathbf{r}_0)| = E_0 u(\mathbf{r}_0)$ and thus, by (2.26),

$$\sqrt{\frac{\nu^2}{\epsilon_0 V_{\text{eff}}}} q = E_0 u(\mathbf{r}_0) T.$$

This permits (2.28) to be expressed in terms of q as

$$\mathbf{E}(\mathbf{r}, t) = \sqrt{\frac{2\nu^2}{\epsilon_0 V_{\text{eff}}}} q \cdot \boldsymbol{\epsilon}.$$

Now that the field is expressed in terms of the canonical variable q , the quantized version of the classical field can be given in one of the following forms:

$$\hat{\mathbf{E}}(\mathbf{r}) = \sqrt{\frac{\nu^2}{\epsilon_0 V_{\text{eff}}}} \hat{q} \boldsymbol{\epsilon} = \sqrt{\frac{\hbar \nu}{2 \epsilon_0 V_{\text{eff}}}} (\hat{a} + \hat{a}^\dagger) \boldsymbol{\epsilon}. \quad (2.36)$$

Time evolution may be considered to apply to operators or vectors (states) in quantum mechanics, so explicit time dependence has been dropped here.

2.3.3 Interaction Hamiltonian

Under the assumption that the field is almost constant across the dimension of the emitter the interaction is that of a dipole interacting with the electric field. A constant field will polarize a quantum dot containing an exciton by pulling the hole and electron in opposite directions. The IFQDs have lateral size of the order of $\lambda/15$ (around 50 nm). This is the so-called dipole approximation.

The energy of an electric dipole interacting with an electric field is:

$$V = -\boldsymbol{\mu} \cdot \mathbf{E}. \quad (2.37)$$

In order to quantize this energy equation look at the atomic dipole operator. We already have a quantized form for the electric field from the previous subsection. Expand the dipole operator in the basis of atomic operators by once again inserting two complete sets. The dipole operator is expressed as: $\hat{\boldsymbol{\mu}} = e \cdot \hat{\boldsymbol{x}}$. This has an

odd parity, so it will have non-vanishing matrix elements only between states of different parity.

$$\begin{aligned}
\hat{\mu} &= \sum_{i,j \in \{a,b\}} |i\rangle\langle i| \hat{\mu} |j\rangle\langle j| \\
&= \sum_{i,j \in \{a,b\}} |i\rangle\langle j| \langle i| \hat{\mu} |j\rangle \\
&= \sum_{i,j \in \{a,b\}} |i\rangle\langle j| \langle i| \hat{e}_x |j\rangle \\
&= \mu_{ab} |a\rangle\langle b| + \mu_{ba} |b\rangle\langle a|
\end{aligned} \tag{2.38}$$

Hermiticity of the dipole operator requires that the nonzero dipole matrix elements be related by a complex conjugate.

$$\begin{aligned}
\hat{\mu} &= \mu_{ab} |a\rangle\langle b| + \mu_{ba} |b\rangle\langle a| \\
\hat{\mu}^\dagger &= \mu_{ab}^* |b\rangle\langle a| + \mu_{ba}^* |a\rangle\langle b| \\
\hat{\mu} = \hat{\mu}^\dagger &\Leftrightarrow \mu_{ab} = \mu_{ba}^*.
\end{aligned} \tag{2.39}$$

Using the results of (2.38) and (2.39) and writing the complex dipole matrix elements in polar form, the dipole operator may be written as:

$$\hat{\mu} = \mu e^{i\Phi} |a\rangle\langle b| + \mu e^{-i\Phi} |b\rangle\langle a|$$

A suitable change of basis will render the dipole matrix elements real. Suppose that

$$\langle a' | \hat{\mu} | a' \rangle = \langle b' | \hat{\mu} | b' \rangle = 0 \quad \langle a' | \hat{\mu} | b' \rangle = \langle b' | \hat{\mu} | a' \rangle = \mu$$

where $|a'\rangle$ and $|b'\rangle$ are related to $|a\rangle$ and $|b\rangle$ by a change of basis \hat{T} :

$$\begin{aligned} |a'\rangle &= \hat{T} |a\rangle = e^{\frac{i\Phi}{2}} |a\rangle \\ |b'\rangle &= \hat{T} |b\rangle = e^{-\frac{i\Phi}{2}} |b\rangle. \end{aligned}$$

Notice that \hat{T} is a unitary operator. Its matrix will be diagonal so that complex conjugation has the same effect as a Hermitian adjoint; to produce an inverse operator $\hat{T}^\dagger = \hat{T}^{-1}$.

Now just write down the matrix elements of $\hat{\mu}$ in the primed basis.

$$\begin{aligned} \langle a' | \hat{\mu} | b' \rangle &= \langle a | (e^{-i\Phi/2} \hat{\mu} e^{-i\Phi/2}) | b \rangle \\ &= \langle a | \hat{\mu} | b \rangle e^{-i\Phi} = \mu \\ \langle b' | \hat{\mu} | a' \rangle &= \langle b | (e^{i\Phi/2} \hat{\mu} e^{i\Phi/2}) | a \rangle \\ &= \langle b | \hat{\mu} | a \rangle e^{i\Phi} = \mu. \end{aligned}$$

Equivalently, one may leave the two energy eigenstates fixed and regard the transformation as applying to the dipole operator (i.e. a unitary or similarity transformation).

Now that it has been shown that a change of basis *can* produce real matrix elements as desired, just relabel the basis vectors so that a and b correspond to the basis states that produce real matrix elements in the dipole matrix. This gives us the resulting expression for the dipole operator:

$$\hat{\mu} = \mu \left(\hat{S}_+ + \hat{S}_- \right). \quad (2.40)$$

Now multiply with the electric field operator which is given in (2.36). The resulting interaction Hamiltonian is given by the following equation:

$$\begin{aligned} \hat{\mathcal{H}}_{\text{Int}} &= -\hat{\mu} \cdot \hat{\mathbf{E}}(\mathbf{r}, t) \\ &= -\mu \sqrt{\frac{\hbar \nu}{\epsilon_0 V}} u(\mathbf{r}) \left(\hat{S}_+ + \hat{S}_- \right) (\hat{a} + \hat{a}^\dagger) \cos \varphi. \end{aligned} \quad (2.41)$$

Here $\cos \varphi$ is due to the dot product between the field and the dipole unit vectors.

Let the coefficient of the operators be equal to $\hbar \cdot g$.

$$\begin{aligned} \hbar g &= \mu E_0 \cos \varphi \\ g &= \mu \sqrt{\frac{\nu}{\hbar \epsilon_0 V}} \cos \varphi. \end{aligned} \quad (2.42)$$

The new parameter g is the coupling constant and is the characteristic frequency for the interaction. The interaction Hamiltonian now appears as follows:

$$\hat{\mathcal{H}}_{\text{Int}} = -\hbar g (\hat{a} + \hat{a}^\dagger) (\hat{S}_+ + \hat{S}_-) \quad (2.43)$$

Rotating Wave Approximation

To obtain a simplified form for the Hamiltonian, we briefly examine the time evolution of the terms in the interaction Hamiltonian in the interaction picture. In the interaction picture, the time evolution of operators is generated by the free Hamiltonian, while the interaction generates time evolution for the state vector.

The free Hamiltonian is:

$$\hat{\mathcal{H}}_0 = \hbar\nu \cdot \hat{n} + \frac{1}{2}\hbar\omega \cdot \hat{\sigma}_z. \quad (2.44)$$

The time evolution for operators is governed by a Heisenberg equation. A general operator obeys the following equation.

$$\dot{\hat{O}} = \frac{1}{i\hbar} [\hat{O}, \hat{\mathcal{H}}_0]. \quad (2.45)$$

Or, more explicitly,

$$\begin{aligned}
\dot{\hat{a}} &= \frac{1}{i\hbar} [\hat{a}, \hat{\mathcal{H}}_0] \\
&= \frac{1}{i\hbar} [\hat{a}, \hbar\nu (\hat{a}^\dagger \hat{a})] \\
&= -i\nu (\hat{a} \hat{a}^\dagger \hat{a} - \hat{a}^\dagger \hat{a} \hat{a}) \\
&= -i\nu (\hat{a} \hat{a}^\dagger - \hat{a}^\dagger \hat{a}) \hat{a} \\
&= -i\nu [\hat{a}, \hat{a}^\dagger] \hat{a} \\
&= -i\nu \hat{a},
\end{aligned}$$

which has the immediate solution:

$$\hat{a}(t) = \hat{a}(0)e^{-i\nu t}. \quad (2.46)$$

Taking the Hermitian conjugate of equation (2.46) gives the evolution of the creation operator.

$$\hat{a}^\dagger(t) = \hat{a}^\dagger(0)e^{i\nu t}. \quad (2.47)$$

Similarly, calculate the time evolution for the atomic operators.

$$\begin{aligned}
\dot{\hat{S}}_- &= \frac{1}{i\hbar} [\hat{S}_-, \hat{\mathcal{H}}_0] = \frac{1}{i\hbar} \left[\hat{S}_-, \frac{1}{2} \hbar \omega \hat{\sigma}_z \right] \\
&= -i\omega \frac{1}{2} \cdot [\hat{S}_-, \hat{\sigma}_z] \\
&= -i\omega \frac{1}{2} \cdot 2\hat{S}_- \\
&= -i\omega \hat{S}_-
\end{aligned}$$

Taking the adjoint provides us with the equation of motion for the raising operator.

$$\dot{\hat{S}}_+ = i\omega\hat{S}_+. \quad (2.48)$$

From (2.43) we see that the terms have the following time evolution.

$$\hat{a}^\dagger(t)\hat{S}_+(t) = \hat{a}^\dagger(0)\hat{S}_+(0)e^{i(\omega+\nu)t} \quad (2.49)$$

$$\hat{a}(t)\hat{S}_-(t) = \hat{a}(0)\hat{S}_-(0)e^{-i(\omega+\nu)t} \quad (2.50)$$

$$\hat{a}^\dagger(t)\hat{S}_-(t) = \hat{a}^\dagger(0)\hat{S}_-(0)e^{-i(\omega-\nu)t} \quad (2.51)$$

$$\hat{a}(t)\hat{S}_+(t) = \hat{a}(0)\hat{S}_+(0)e^{i(\omega-\nu)t} \quad (2.52)$$

Normally, under the rotating wave approximation (RWA) we boost to a rotating frame and then take the DC component. In this situation where we consider the product of two operators and under the condition that the atomic transition and the cavity mode are close to resonance we really just need to take the low frequency components; high frequency components will quickly average to zero. Dropping terms corresponding to (2.49) and (2.50) while keeping terms given by (2.51) and (2.52) gives us the following simplified interaction Hamiltonian.

$$\boxed{\hat{\mathcal{H}}_{\text{Int}} = -\hbar g \left(\hat{a} \hat{S}_+ + \hat{a}^\dagger \hat{S}_- \right)} \quad (2.53)$$

2.3.4 Total Hamiltonian

The dynamics unfold in a composite Hilbert space. The composite space is simply the tensor product of the two independent Hilbert spaces. First, the formalism for a composite Hilbert space is presented following the treatment of [6]. Then, the final form of the operators in the composite Hilbert space will be derived. It will be seen that simply expanding the Hamiltonian in terms of the basis vectors over the composite space automatically produces operators of the correct dimensionality.

Composite Hilbert Space

The Hilbert space is composite. Taking the tensor product of the two independent Hilbert spaces produces a new Hilbert space whose dimension is the product of the dimensions of the constituent Hilbert spaces.

$$\mathfrak{H} = \mathfrak{H}^A \otimes \mathfrak{H}^B \quad (2.54)$$

Then, given fixed orthonormal bases $\{|\varphi_i^{(A)}\rangle\}$ and $\{|\varphi_j^{(B)}\rangle\}$ in \mathfrak{H}^A and \mathfrak{H}^B respectively, a general state in \mathfrak{H} may be written:

$$|\psi\rangle = \sum_{i,j} |\varphi_i^{(A)}\rangle \otimes |\varphi_j^{(B)}\rangle. \quad (2.55)$$

It then follows that an operator over this composite space has the following expansion:

$$\hat{O} = \sum_i \hat{O}_i^A \otimes \hat{O}_i^B. \quad (2.56)$$

In the context of the current problem our basis consists of $\{|\phi_i^{Field}\rangle \otimes |\phi_j^{2-level}\rangle\}$. This set of vectors spans the composite Hilbert space. Then, a unified Hamiltonian may be constructed by expanding in terms of these vectors. Let $|i, m\rangle = |m\rangle \otimes |i\rangle$.

The Hamiltonian is composed of an pseudospin part, a field part, and a part that overlaps both spaces. Exploit the completeness of the states and insert the corresponding identity operators:

$$\begin{aligned} \hat{\mathcal{H}} &= \hat{\mathcal{H}}_{2-level} + \hat{\mathcal{H}}_{Field} + \hat{\mathcal{H}}_{Int} \\ \Rightarrow \hat{\mathcal{H}} &= \sum_{i,j \in \{b,a\}} \sum_{m,n=0}^{\infty} |i, m\rangle \langle j, n| \langle i, m| \hat{\mathcal{H}}_{2-level} |j, n\rangle \\ &+ \sum_{i,j \in \{b,a\}} \sum_{m,n=0}^{\infty} |i, m\rangle \langle j, n| \langle i, m| \hat{\mathcal{H}}_{Field} |j, n\rangle \\ &+ \sum_{i,j \in \{b,a\}} \sum_{m,n=0}^{\infty} |i, m\rangle \langle j, n| \langle i, m| \hat{\mathcal{H}}_{AF} |j, n\rangle. \end{aligned} \quad (2.57)$$

It is now time to calculate the appropriate matrix elements in the composite basis.

$$\begin{aligned}
\langle i, m | \hat{\mathcal{H}}_{2-level} | j, n \rangle &= \frac{1}{2} \hbar \omega \langle i | \langle m | (|a\rangle\langle a| - |b\rangle\langle b|) | n \rangle | j \rangle \\
&= \frac{1}{2} \hbar \omega \langle m | n \rangle (\langle i | a \rangle \langle a | j \rangle - \langle i | b \rangle \langle b | j \rangle) \\
&= \frac{\hbar \omega}{2} \delta_{mn} (\delta_{ia} \delta_{aj} - \delta_{ib} \delta_{bj})
\end{aligned} \tag{2.58}$$

$$\begin{aligned}
\langle i, m | \hat{\mathcal{H}}_{Field} | j, n \rangle &= \langle i | \langle m | \hbar \omega \cdot \hat{n} | n \rangle | j \rangle \\
&= \hbar \omega \cdot n \delta_{mn} \delta_{ij}
\end{aligned} \tag{2.59}$$

$$\begin{aligned}
\langle i, m | \hat{\mathcal{H}}_{Int} | j, n \rangle &= -\hbar g \langle i, m | (\hat{S}_+ \cdot \hat{a} + \hat{S}_- \cdot \hat{a}^\dagger) | j, n \rangle \\
&= -\hbar g \langle i, m | (|a\rangle\langle b| \cdot \hat{a} + |b\rangle\langle a| \cdot \hat{a}^\dagger) | j, n \rangle \\
&= -\hbar g [\langle i, m | a \rangle \langle b | \hat{a} | j, n \rangle + \langle i, m | b \rangle \langle a | \hat{a}^\dagger | j, n \rangle] \\
&= -\hbar g [\sqrt{n} \langle i, m | a \rangle \langle b | j, n-1 \rangle + \sqrt{n''+1} \langle i, m | b \rangle \\
&\quad \times \langle a | j, n+1 \rangle] \\
&= -\hbar g [\sqrt{n} \cdot \delta_{ia} \delta_{bj} \delta_{m,n-1} + \sqrt{n+1} \cdot \delta_{ib} \delta_{aj} \delta_{m,n+1}]
\end{aligned} \tag{2.60}$$

Substitution of the results (2.58), (2.59) and (2.60) into (2.57) gives the following expression for the Hamiltonian.

$$\begin{aligned}\hat{\mathcal{H}} &= \sum_{i,j \in \{b,a\}} \sum_{m,n=0}^{\infty} |i, m\rangle\langle j, n| \frac{\hbar\omega}{2} (\delta_{ia}\delta_{aj} - \delta_{ib}\delta_{bj}) \delta_{mn} \\ &+ \sum_{i,j \in \{b,a\}} \sum_{m,n=0}^{\infty} |i, m\rangle\langle j, n| n \hbar\nu \delta_{ij} \delta_{mn} \\ &- \sum_{i,j \in \{b,a\}} \sum_{m,n=0}^{\infty} |i, m\rangle\langle j, n| \hbar g [\sqrt{n} \cdot \delta_{ia}\delta_{bj} \delta_{m,n-1} + \sqrt{n+1} \cdot \delta_{ib}\delta_{aj} \delta_{m,n+1}]\end{aligned}$$

Rewriting the outerproduct $|i, m\rangle\langle j, n| = |m\rangle\langle n| \otimes |i\rangle\langle j|$, as suggested by (2.56) yields the expression below.

$$\begin{aligned}\hat{\mathcal{H}} &= \sum_{i,j \in \{b,a\}} \sum_{m,n=0}^{\infty} |m\rangle\langle n| \otimes |i\rangle\langle j| \frac{\hbar\omega}{2} (\delta_{ia}\delta_{aj} - \delta_{ib}\delta_{bj}) \delta_{mn} \\ &+ \sum_{i,j \in \{b,a\}} \sum_{m,n=0}^{\infty} |m\rangle\langle n| \otimes |i\rangle\langle j| n \hbar\nu \delta_{ij} \delta_{mn} \\ &- \sum_{i,j \in \{b,a\}} \sum_{m,n=0}^{\infty} |m\rangle\langle n| \otimes |i\rangle\langle j| \hbar g [\sqrt{n} \cdot \delta_{ia}\delta_{bj} \delta_{m,n-1} + \sqrt{n+1} \cdot \delta_{ib}\delta_{aj} \delta_{m,n+1}]\end{aligned}$$

The interaction reduces to the following expression:

$$\hat{\mathcal{H}}_{\text{Int}} = -\hbar g \sum_{n=0}^{\infty} \left(|n\rangle\langle n+1| \otimes \underbrace{|a\rangle\langle b|}_{\hat{S}_+} + |n+1\rangle\langle n| \otimes \underbrace{|b\rangle\langle a|}_{\hat{S}_-} \right) \sqrt{n+1}. \quad (2.61)$$

We utilize the following result:

$$\sum_{i,j \in \{a,b\}} |i\rangle\langle j| \delta_{ij} = \sum_{i \in \{a,b\}} |i\rangle\langle i| = \hat{\mathbb{I}}_{2-level} \quad (2.62)$$

$$\sum_{m,n=0}^{\infty} |m\rangle\langle n| \delta_{mn} = \sum_{n=0}^{\infty} |n\rangle\langle n| = \hat{\mathbb{I}}_{Field}. \quad (2.63)$$

This leads to the following simplified form for the Hamiltonian operator over the composite Hilbert space.

$$\boxed{\hat{\mathcal{H}} = \hat{\mathcal{H}}_{Field} \otimes \hat{\mathbb{I}}_{2-level} + \hat{\mathbb{I}}_{Field} \otimes \hat{\mathcal{H}}_{2-level} + \hat{\mathcal{H}}_{Int}} \quad (2.64)$$

It is now possible to write out explicit matrix representations of these operators by choosing an appropriate map between kets and column vectors. For the present work it makes sense to use

$$\{|b\rangle, |a\rangle\} \rightarrow \left\{ \begin{bmatrix} 1 \\ 0 \end{bmatrix}, \begin{bmatrix} 0 \\ 1 \end{bmatrix} \right\}$$

and

$$\{|0\rangle, |1\rangle, |2\rangle, \dots, |n\rangle, \dots\} \rightarrow \left\{ \begin{array}{c} \left[\begin{array}{c} 1 \\ 0 \\ \vdots \\ \vdots \end{array} \right], \left[\begin{array}{c} 0 \\ 1 \\ 0 \\ \vdots \\ \vdots \end{array} \right], \left[\begin{array}{c} 0 \\ 0 \\ 1 \\ 0 \\ \vdots \\ \vdots \end{array} \right], \dots, \left[\begin{array}{c} 0 \\ \vdots \\ \vdots \\ 1 \\ \vdots \end{array} \right], \dots \end{array} \right\}.$$

These column vectors can be suitably used to represent the dynamics of the problem at hand. Matrices provide a representation that can convey visual information about interactions and can allow visual identification of non-interacting subspaces. This map of kets into column vectors allows the various pieces of the Hamiltonian to be written in matrix form. First write down the matrix for the 2-level system and the field. Combine these to get the free Hamiltonian (with no interactions). Then write down the interaction Hamiltonian and combine it with the free Hamiltonian to produce the full Hamiltonian for the Jaynes-Cummings system.

In order to produce matrices that span both spaces, employ a direct (or Kronecker) product between operators in each Hilbert space. The direct product

is defined such that the components of a matrix $\mathbf{C} = \mathbf{A} \otimes \mathbf{B}$ are given by

$$c_{mn} = a_{ij}b_{kl}$$

where $m = p(i - 1) + k$, $n = p(j - 1) + l$ and where \mathbf{B} is a $p \times p$ matrix. This can be succinctly displayed by supposing that \mathbf{A} is a 2×2 matrix. Then we can directly write

$$\mathbf{C} = \begin{bmatrix} a_{11}\mathbf{B} & a_{12}\mathbf{B} \\ a_{21}\mathbf{B} & a_{22}\mathbf{B} \end{bmatrix}.$$

By writing the outer product $|i, m\rangle\langle j, n|$ as $|m\rangle\langle n| \otimes |i\rangle\langle j|$ a representation has already been chosen. The 2-level Hilbert space stands to the right in the direct product. This means that the operators for the composite Hilbert space will tend to contain 2×2 blocks, as will be shown shortly.

Next, write down the matrix for the interaction Hamiltonian using the matrix elements from (2.60).

$$\hat{\mathcal{H}}_{\text{int}} = -\hbar g \begin{bmatrix} \begin{pmatrix} 0 & 0 \\ 0 & 0 \end{pmatrix} & \begin{pmatrix} 0 & 0 \\ 1 & 0 \end{pmatrix} & \begin{pmatrix} 0 & 0 \\ 0 & 0 \end{pmatrix} & \dots & \begin{pmatrix} 0 & 0 \\ 0 & 0 \end{pmatrix} \\ \begin{pmatrix} 0 & 1 \\ 0 & 0 \end{pmatrix} & \ddots & \begin{pmatrix} 0 & 0 \\ \sqrt{2} & 0 \end{pmatrix} & \ddots & \vdots \\ \begin{pmatrix} 0 & 0 \\ 0 & 0 \end{pmatrix} & \begin{pmatrix} 0 & \sqrt{2} \\ 0 & 0 \end{pmatrix} & \ddots & \ddots & \begin{pmatrix} 0 & 0 \\ 0 & 0 \end{pmatrix} \\ \vdots & \ddots & \ddots & \ddots & \begin{pmatrix} 0 & 0 \\ \sqrt{n+1} & 0 \end{pmatrix} \\ \begin{pmatrix} 0 & 0 \\ 0 & 0 \end{pmatrix} & \dots & \begin{pmatrix} 0 & 0 \\ 0 & 0 \end{pmatrix} & \begin{pmatrix} 0 & \sqrt{n+1} \\ 0 & 0 \end{pmatrix} & \ddots \end{bmatrix}$$

frequency. As in classical mechanics, they provide a mathematically convenient and conceptually simple basis for expanding the dynamics of systems of coupled oscillators.

2.4.1 Minimal Decoupled Subspace

As in classical mechanics off-diagonal elements in the Hamiltonian matrix signify coupling between the various degrees of freedom. The Hamiltonian is block diagonal, consisting of 2×2 blocks along the major diagonal. It is for this reason that the Hilbert space was decomposed into the current ordering for the direct product. By writing the atomic Hilbert space to the right we are provided with a matrix containing 2×2 blocks. The block diagonal structure means that each 2×2 block represents an independent subspace which is not coupled to the rest of the Hilbert space. As indicated previously, this is only a choice of representation and doesn't change any intrinsic properties of the vector space (e.g., which states couple to which other states). However, the particular choice of representation can greatly simplify calculation and interpretation. In practice it is generally easier to identify non-interacting subspaces when their terms are grouped together in blocks in matrix representations.

The Hamiltonian given by the n^{th} block is:

$$\mathbf{H}_n = \hbar\nu \left(n + \frac{1}{2}\right) \begin{bmatrix} 1 & 0 \\ 0 & 1 \end{bmatrix} + \frac{\hbar}{2} \begin{bmatrix} \Delta & -\Omega_R \\ -\Omega_R & -\Delta \end{bmatrix}, \quad (2.66)$$

where $\Delta \equiv \omega - \nu$ is called the detuning and $\Omega_R \equiv 2g\sqrt{n+1}$ is called the Rabi frequency. This implies that each subspace is spanned by two quantum states: $|a, n\rangle$ and $|b, n+1\rangle$. Based on the structure of the Hamiltonian over the entire Hilbert space we see that the kets in the combined Hilbert space map naturally map to a normally ordered two-dimensional basis in the following way:

$$|a, n\rangle \rightarrow \begin{bmatrix} 1 \\ 0 \end{bmatrix}, \quad |b, n+1\rangle \rightarrow \begin{bmatrix} 0 \\ 1 \end{bmatrix}$$

2.4.2 Eigenvalues and Eigenvectors

This reduced subspace is manageable and may be easily diagonalized. The first matrix in (2.66) is proportional to the identity matrix so it will remain diagonal under any suitable principal axis transformation. We need only find the eigenvectors of the second matrix.

First label the matrix to be diagonalized as Ω' . The factor of $\hbar/2$ has been dropped, for now.

$$\Omega' = \begin{bmatrix} \Delta & -\Omega_R \\ -\Omega_R & -\Delta \end{bmatrix}$$

$$\det(\Omega' - \lambda\mathbf{I}) = 0.$$

$$\Rightarrow \begin{vmatrix} \Delta - \lambda & -\Omega_R \\ -\Omega_R & -\Delta - \lambda \end{vmatrix} = 0 \tag{2.67}$$

$$\begin{aligned}
&\Rightarrow (\lambda - \Delta)(\Delta + \lambda) - \Omega_R^2 = 0 \\
&\Rightarrow \lambda = \pm \sqrt{\Delta^2 + \Omega_R^2} = \pm \Omega_n
\end{aligned} \tag{2.68}$$

Now to generate the appropriate eigenvectors, apply each of the eigenvalues to the eigenvalue equation -- $\Omega' \cdot \mathbf{v} = \lambda \mathbf{v}$.

$$\begin{aligned}
&\begin{bmatrix} \Delta & -\Omega_R \\ -\Omega_R & -\Delta \end{bmatrix} \begin{bmatrix} a \\ b \end{bmatrix} = \lambda \begin{bmatrix} a \\ b \end{bmatrix} \\
&\Rightarrow \begin{cases} (\Delta - \lambda)a - (\Omega_R)b = 0 \\ (-\Omega_R)a + (-\Delta - \lambda)b = 0 \end{cases}
\end{aligned} \tag{2.69}$$

Additionally, the change of basis should preserve the normalization. Invoke the normalization condition for the eigenvectors.

$$\begin{aligned}
&\vec{v} = (a, b) \\
&|\vec{v}| = 1 \Leftrightarrow a^2 + b^2 = 1
\end{aligned} \tag{2.70}$$

Using (2.69) and (2.70) gives a set of normalized eigenvectors. For $\lambda = -\Omega_n$:

$$\begin{aligned}
b^2 &= \frac{\overbrace{-\Omega_R}^{(2.69)} \overbrace{\Delta + \Omega_n}^{(2.70)}}{\Delta - \Omega_n} a^2 = \overbrace{1 - a^2}^{(2.70)} \\
&\Rightarrow \frac{\Omega_n^2 - \Delta^2}{(\Delta - \Omega_n)^2} a^2 = 1 - a^2 \\
&\Rightarrow \left(\frac{\Omega_R^2}{(\Delta - \Omega_n)^2} + 1 \right) a^2 = 1 \\
&\Rightarrow a^2 = \frac{(\Delta - \Omega_n)^2}{(\Delta - \Omega_n)^2 + \Omega_R^2} \\
&\Rightarrow a = \frac{\Omega_n - \Delta}{\sqrt{(\Delta - \Omega_n)^2 + \Omega_R^2}} \\
b &= \frac{-\Omega_R}{\Delta - \Omega_n} a = \frac{\Omega_R}{\sqrt{(\Delta - \Omega_n)^2 + \Omega_R^2}} \\
\vec{v}_- &= \begin{bmatrix} \frac{\Omega_n - \Delta}{\sqrt{(\Delta - \Omega_n)^2 + \Omega_R^2}} \\ \frac{\Omega_R}{\sqrt{(\Delta - \Omega_n)^2 + \Omega_R^2}} \end{bmatrix}
\end{aligned}$$

Meanwhile, a similar calculation for $\lambda = \Omega_n$ gives the other independent eigenvector.

$$\vec{v}_+ = \begin{bmatrix} \frac{\Omega_R}{\sqrt{(\Delta - \Omega_n)^2 + \Omega_R^2}} \\ \frac{\Delta - \Omega_n}{\sqrt{(\Delta - \Omega_n)^2 + \Omega_R^2}} \end{bmatrix}$$

Consistent with the normalization condition we can make a trigonometric substitution for the components of the eigenvectors.

$$\sin \theta_n = \frac{\Delta - \Omega_n}{\sqrt{(\Omega_n - \Delta)^2 + \Omega_R^2}}; \quad \cos \theta_n = \frac{\Omega_R}{\sqrt{(\Omega_n - \Delta)^2 + \Omega_R^2}} \quad (2.71)$$

$$\Rightarrow \sin 2\theta_n = \frac{\Omega_R}{\Omega_n}; \quad \cos 2\theta_n = -\frac{\Delta}{\Omega_n} \quad (2.72)$$

The transformation matrix which diagonalizes the Hamiltonian may now be written as:

$$\mathbf{P} = \begin{bmatrix} \cos \theta_n & -\sin \theta_n \\ \sin \theta_n & \cos \theta_n \end{bmatrix}. \quad (2.73)$$

In other words, the diagonalized Hamiltonian is obtained from the original Hamiltonian via a similarity transformation (a unitary transformation).

$$\mathbf{H}' = \mathbf{P}^{-1}\mathbf{H}\mathbf{P}$$

$$\Rightarrow \mathbf{H} =$$

$$\mathbf{H} \cdot \mathbf{v} = E\mathbf{v}$$

$$\mathbf{P}\mathbf{H}'\mathbf{P}^{-1} \cdot \mathbf{v} = E\mathbf{v}$$

$$\mathbf{H}'\mathbf{P}^{-1} \cdot \mathbf{v} = E\mathbf{P}^{-1} \cdot \mathbf{v}$$

$$\Rightarrow \mathbf{v}' = \mathbf{P} \cdot \mathbf{v}$$

Thus, the inverse matrix of \mathbf{P} provides for the change of basis from the bare states into the dressed states (the new eigenvectors). For example, The \vec{v}_+ vector is transformed by \mathbf{P}^{-1} as follows:

$$\begin{bmatrix} \cos \theta_n & \sin \theta_n \\ -\sin \theta_n & \cos \theta_n \end{bmatrix} \begin{bmatrix} \cos \theta_n \\ \sin \theta_n \end{bmatrix} = \begin{bmatrix} 1 \\ 0 \end{bmatrix}.$$

The map between dressed states and column vectors in the dressed state basis is therefore given by

$$\{|n, +\rangle_d, |n, -\rangle_d\} = \left\{ \begin{bmatrix} 1 \\ 0 \end{bmatrix}, \begin{bmatrix} 0 \\ 1 \end{bmatrix} \right\}.$$

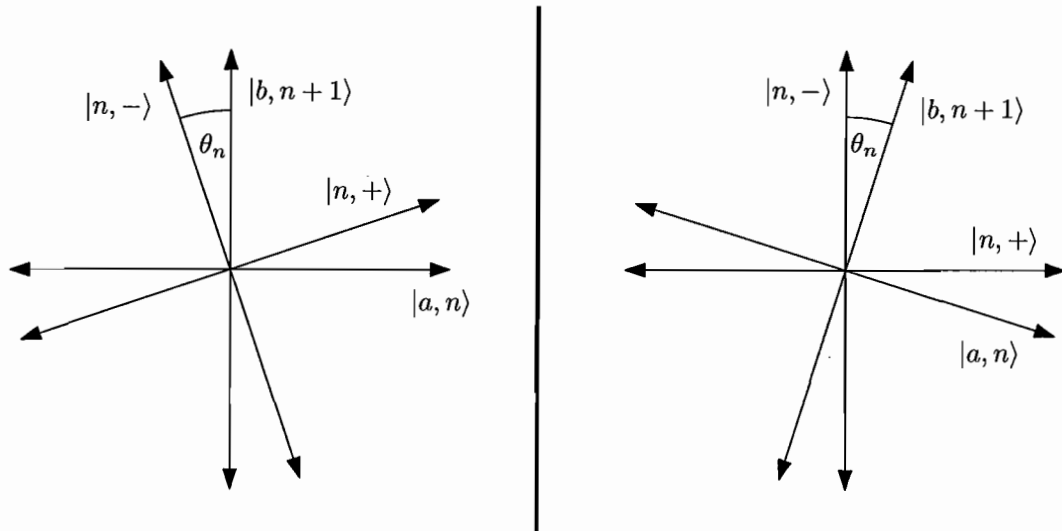


FIGURE 2.8: Rotation from bare states into dressed states. This diagram shows a geometric representation of the change of basis from the bare states into the dressed states in terms of the mixing angle θ_n . The graph on the left shows the dressed states in terms of bare basis vectors. The graph on the right shows the bare states in terms of dressed basis vectors.

$$\begin{bmatrix} C_{n+} \\ C_{n-} \end{bmatrix} = \begin{bmatrix} \cos \theta_n & \sin \theta_n \\ -\sin \theta_n & \cos \theta_n \end{bmatrix} \begin{bmatrix} C_{a,n} \\ C_{b,n+1} \end{bmatrix} \quad (2.74)$$

The eigenstates of the “free” Hamiltonian are referred to as bare states. It is said that the interaction dresses the states and the new basis, in which the Hamiltonian is diagonal is referred to as the dressed state basis. Alternatively, the dressed states are sometimes referred to as normal modes since the situation is analogous to a classical system of coupled oscillators, in which it becomes advantageous to talk about collective motions of the coupled oscillators rather than insisting on describing the motions of each oscillator separately.

2.4.3 Normal Mode Splitting

Acting on each of the eigenvectors with the Hamiltonian over our chosen manifold, (2.66), we obtain the eigenvalues of the Hamiltonian.

The eigenvalues of the complete Hamiltonian are the energies of the dressed states. They are simply:

$$E_{n,\pm} = \hbar\nu \left(n + \frac{1}{2} \right) \pm \frac{\hbar}{2} \Omega_n. \quad (2.75)$$

The lifting of the degenerate eigenvalues of the free Hamiltonian by the inclusion of the interaction is called normal-mode splitting. At zero detuning (i.e. on resonance), the energy now exhibits a split spectrum as shown in figure 2.9.

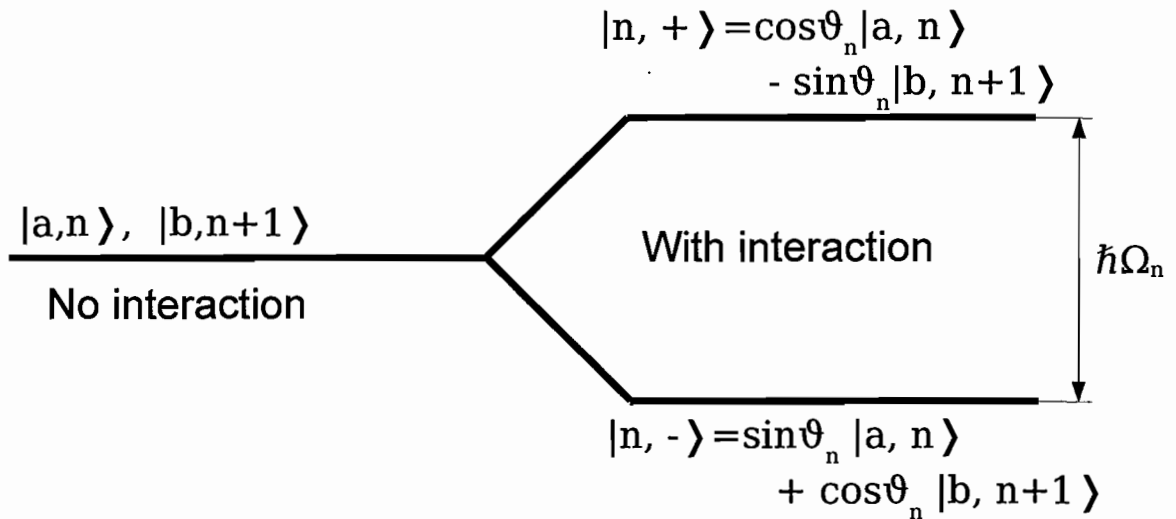


FIGURE 2.9: Effect of interaction on energy levels; normal mode splitting. The energy levels of the energy eigenstates are shown in the case of inclusion of the interaction (right) and sans interaction (left). The lifting of the degeneracy by the interaction is sometimes called normal mode splitting.

Consider varying the cavity length so that the resonance frequency of the intra-cavity field changes. If we plot the energies of the dressed and bare states we can see that the dressed states become asymptotic to the bare states in the limit of large detunings. For the $n = 0$ manifold the bare states correspond to a vacuum state of the field with an excited state (ground-state exciton) of the quantum dot or a single excitation in the field and a vacuum state of the quantum dot.

The eigenvalues for the $n = 0$ manifold are $E_{0,\pm} = \frac{\hbar}{2} [\nu \pm \sqrt{(\omega - \nu)^2 + \Omega_R^2}]$. In the limit of large Δ we can ignore the factor of Ω_R^2 and evaluate the square root as

having the value of $\pm\Delta$. Equivalently,

$$\begin{aligned}
E_{0,\pm} &= \frac{\hbar}{2} \left(\nu \pm \sqrt{\Delta^2 + \Omega_R^2} \right) \\
&= \frac{\hbar}{2} \left[\nu \pm \sqrt{\Delta^2} \sqrt{1 + \frac{\Omega_R^2}{\Delta^2}} \right] \\
&\approx \frac{\hbar}{2} \left[\nu \pm \sqrt{\Delta^2} \left(1 + \frac{\Omega_R^2}{2\Delta^2} \right) \right] \quad \text{for } |\Delta| \gg |\Omega_R| \\
&\approx \frac{\hbar}{2} [\nu \pm |\omega - \nu|].
\end{aligned}$$

This approximation is only valid asymptotically. In each of those limits we have

$$\begin{aligned}
E_{0,+} &= \begin{cases} \frac{\hbar}{2}(\nu + \omega - \nu) & \text{for } \nu \ll \omega \\ \frac{\hbar}{2}(\nu + \nu - \omega) & \text{for } \nu \gg \omega \end{cases} \\
&= \begin{cases} \frac{\hbar\omega}{2} & \text{for } \nu \ll \omega \\ \hbar\nu - \frac{\hbar\omega}{2} & \text{for } \nu \gg \omega \end{cases} .
\end{aligned}$$

Similarly, the other set of eigenvalues may be described, asymptotically as

$$E_{0,-} = \begin{cases} \hbar\nu - \frac{\hbar\omega}{2} & \text{for } \nu \ll \omega \\ \frac{\hbar\omega}{2} & \text{for } \nu \gg \omega \end{cases} .$$

By including the constant energy terms that were omitted previously, the energy will be uniformly shifted up by a factor of $\hbar\omega/2$. This makes the lower energy contribution by the two-level system, corresponding to the quantum dot vacuum state, become zero and the upper state take on a value of $\hbar\omega$. This is entirely

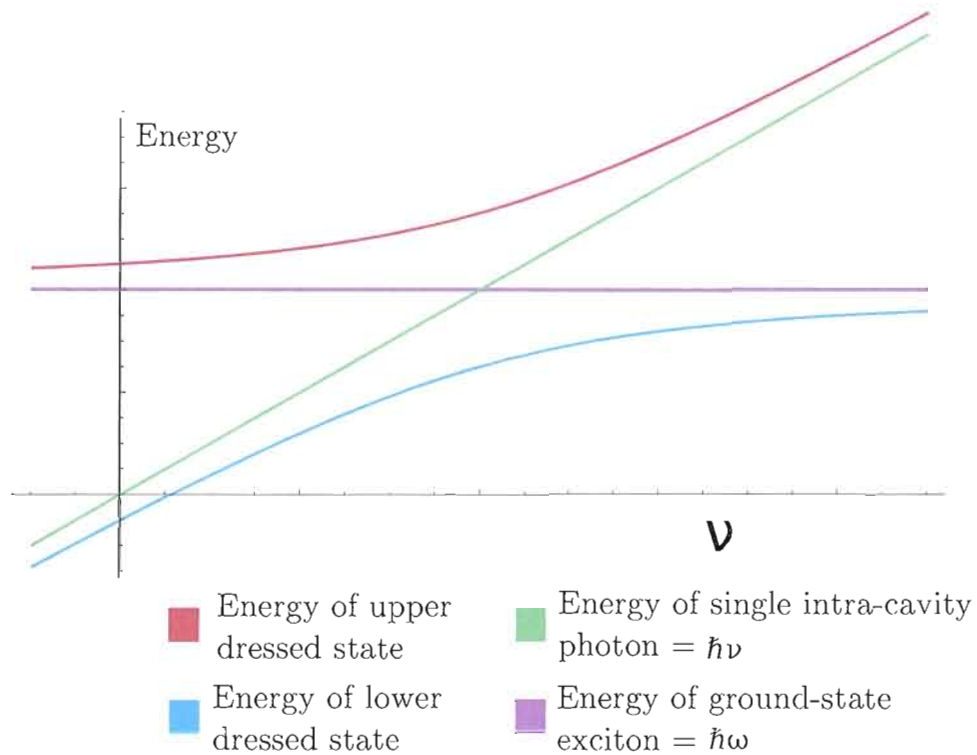


FIGURE 2.10: Energies of bare and dressed states. The energies for both bare states and both dressed states are shown. It can be seen that each of the dressed states asymptotically approaches a different bare state on either side of the resonance.

optional and doesn't affect any dynamical predictions of the system. However, it does enable a slightly simpler labeling of the energy diagram. In this case we may associate the asymptotic bare energies as corresponding to purely one or the other of the bare systems. In other words, the asymptotic bare state energies can be thought of as either an excited quantum dot with vacuum in the cavity field, or a vacuum state of the quantum dot with a single excitation in the cavity field.

2.4.4 Rabi Oscillations

The advantage of transforming into the dressed-state (diagonalized) basis becomes clear when we look at the time evolution of the system. Because the dressed states are eigenstates of the Hamiltonian, they are each necessarily also eigenstates of the time-evolution operator. For example,

$$|n, + (t)\rangle = \hat{U}(t, t_0) |\Psi(t_0)\rangle = e^{-i\phi(t)} |n, +(t_0)\rangle,$$

because the time-evolution operator may produce a time-dependent eigenvalue, but leaves an eigenstate of the Hamiltonian unchanged. For a time-independent Hamiltonian the form of the time-evolution operator is:

$$\hat{U}(t, t_0) = \exp \left[\frac{-i\hat{\mathcal{H}}(t - t_0)}{\hbar} \right].$$

This gives the following time evolution for the quantum state.

$$\begin{aligned} |\psi(t)\rangle &= \exp \left[-i\hat{\mathcal{H}}t/\hbar \right] |\psi(0)\rangle \\ &= \sum_{n=0}^{\infty} \sum_{m \in \{+, -\}} \exp \left[-iE_{nm}t/\hbar \right] |n, m\rangle \langle n, m| \psi(0)\rangle \end{aligned}$$

The eigenvalues of the Hamiltonian and the associated eigenvectors have been determined, so the time evolution is trivial.

$$\begin{aligned}
\begin{bmatrix} C_{n+}(t) \\ C_{n-}(t) \end{bmatrix} &= \left(\exp [iE_{n-}t/\hbar] \begin{bmatrix} 0 & 0 \\ 0 & 1 \end{bmatrix} + \exp [iE_{n+}t/\hbar] \begin{bmatrix} 1 & 0 \\ 0 & 0 \end{bmatrix} \right) \begin{bmatrix} C_{n+}(0) \\ C_{n-}(0) \end{bmatrix} \\
&= e^{[i\frac{2n+1}{2}\nu t]} \begin{bmatrix} e^{i\Omega_n t} & 0 \\ 0 & e^{-i\Omega_n t} \end{bmatrix} \cdot \begin{bmatrix} C_{n+}(0) \\ C_{n-}(0) \end{bmatrix} \tag{2.76}
\end{aligned}$$

In order to see the so-called Rabi oscillations we transform back into the bare state basis. To evolve the bare states forward in time the time-evolution operator must be cast into the bare-state basis.

$$\begin{aligned}
\hat{P} |\psi(t)\rangle_D &= \hat{P} \hat{U}_D \hat{P}^{-1} \hat{P} |\psi(0)\rangle_D \\
|\psi(t)\rangle_B &= \hat{P} \hat{U}_D \hat{P}^{-1} |\psi(0)\rangle_B \\
\begin{bmatrix} C_{a,n}(t) \\ C_{b,n+1}(t) \end{bmatrix} &= \exp \left[i \frac{2n+1}{2} \nu t \right] \cdot \hat{P} \begin{bmatrix} e^{\frac{1}{2}i\Omega_n t} & 0 \\ 0 & e^{-\frac{1}{2}i\Omega_n t} \end{bmatrix} \hat{P}^{-1} \begin{bmatrix} C_{a,n}(0) \\ C_{b,n+1}(0) \end{bmatrix}
\end{aligned}$$

Using (2.73) and performing the necessary matrix multiplication we obtain the following result for the time evolution of the bare states.

$$\begin{bmatrix} C_{a,n}(t) \\ C_{b,n+1}(t) \end{bmatrix} = [\hat{U}_B(t)] \cdot \begin{bmatrix} C_{a,n}(0) \\ C_{b,n+1}(0) \end{bmatrix}$$

where

$$[\hat{U}_B(t)] = e^{[i\frac{2n+1}{2}\nu t]} \cdot \begin{bmatrix} \cos\left(\frac{\Omega_n t}{2}\right) + i \cos 2\theta_n \sin\left(\frac{\Omega_n t}{2}\right) & i \sin 2\theta_n \sin\left(\frac{\Omega_n t}{2}\right) \\ i \sin 2\theta_n \sin\left(\frac{\Omega_n t}{2}\right) & \cos\left(\frac{\Omega_n t}{2}\right) - i \cos 2\theta_n \sin\left(\frac{\Omega_n t}{2}\right) \end{bmatrix}.$$

Suppose the initial state of the system is $C_{a,n}(0) = 1, C_{b,n+1} = 0$. Also, suppose that the mixing angle $\theta_n = \pi/4$ (i.e. the detuning parameter $\Delta = 0$). Then the state at a time t will be given by:

$$\begin{bmatrix} C_{a,n}(t) \\ C_{b,n+1}(t) \end{bmatrix} = \exp\left[i\frac{2n+1}{2}\nu t\right] \cdot \begin{bmatrix} \cos\left(\frac{\Omega_n t}{2}\right) \\ i \sin\left(\frac{\Omega_n t}{2}\right) \end{bmatrix}.$$

So, the probability to find the system in either of the bare states varies sinusoidally. This periodic switching between maximal probability and zero probability is referred to as Rabi flopping.

2.4.5 The Single Quantum Manifold

Now consider the situation in the $n = 0$ manifold. The bare states that span this manifold are: $|b, 1\rangle$ and $|a, 0\rangle$. The representation of the change of basis as a rotation is convenient. In the case of resonance between the cavity mode and the transition between the two levels, the effective mixing angle is $\pi/4$. The time

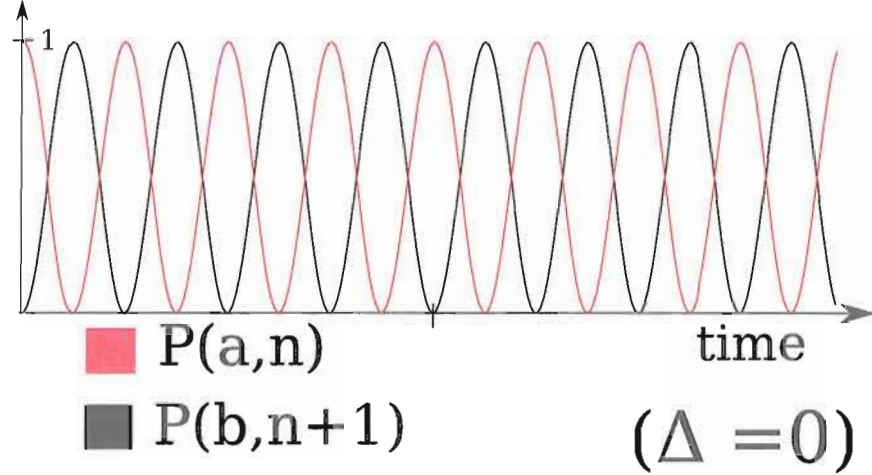


FIGURE 2.11: Rabi flopping. This is a plot of the probabilities of measuring the system in either of the two bare states as a function of time, assuming zero detuning. Each probability oscillates with a period of $\frac{2\pi}{\Omega_n}$.

evolution, in this case, is simply given by

$$\begin{bmatrix} C_-(t) \\ C_+(t) \end{bmatrix} = \begin{bmatrix} e^{i(\nu - \Omega_R)t/2} & 0 \\ 0 & e^{i(\nu + \Omega_R)t/2} \end{bmatrix} \begin{bmatrix} C_-(0) \\ C_+(0) \end{bmatrix}.$$

Correspondingly, the quantum state exhibits maximal entanglement — the two Schmidt numbers have equal magnitude. This is commonly referred to as a Schrödinger cat state.

The normal-mode splitting, in this case, is commonly referred to as vacuum Rabi splitting and the oscillations of the state vectors as vacuum Rabi oscillations. An example of Rabi oscillations in a semiclassical context are oscillations in the state of a two-level atom driven by a resonant optical field. The frequency of the oscillations (flopping) is proportional to the amplitude of the applied electric field.

The Rabi flopping in this case cannot be explained semiclassically. In the case of an initially excited two-level system, the electromagnetic field is in a vacuum state. It may roughly be said that the excited atom undergoes emission that's stimulated by the vacuum field of the cavity mode and for this reason the splitting of the energy levels and the oscillations in the probabilities of measuring either of the bare states are referred to, respectively, as vacuum Rabi splitting and vacuum Rabi oscillations.

Obviously, this phenomenology will apply to any two level system interacting with a single mode of the electromagnetic field.

2.5 Linewidth, Dissipation and Open Systems

The preceding treatment is sufficient for explaining the appearance of certain features in experimental studies, but fails to properly describe most real world systems that one might hope to measure. The reason for this is the rather idealized closed system. The situation parallels that of a driven, undamped oscillator in classical mechanics. The spectrum consists of a set of delta function peaks.

Realistic oscillators exhibit damping, which may arise in the context of classical mechanics as (velocity dependent) dissipative forces, or in quantum mechanics as dissipative couplings to external degrees of freedom. They both correspond to interactions that carry energy out of the system of interest and lead to damped responses, characterized by finite amplitudes and linewidths for oscillators.

More precisely, a realistic model of a quantum optical system should allow for interactions with unmonitored degrees of freedom, which may lead to dissipation and dephasing (decoherence). Dissipation corresponds to reduction of probabilities (diagonal components of the density matrix). This also, necessarily reduces the size of the off-diagonal coherence terms. This is termed dissipation-driven decoherence. Dephasing corresponds to decay of the off-diagonal terms and the approach to a classical mixture (also retreat from a quantum pure state). Decoherence that proceeds without associated dissipation may be called pure dephasing.

It is, therefore, necessary to employ a model that includes couplings to external degrees of freedom in order to account for real-world phenomenology. For example, the mode of the optical cavity is connected to other modes of the electro-magnetic field via scattering and transmission. The two-level emitter, which in these experiments is an interface fluctuation quantum dot, may also couple to non-cavity modes of the field via spontaneous emission (especially in the case of an open-sided cavity as used here). In the case of a single atom, the primary interaction channels involve radiative couplings. In the case of a QD, a number of other channels may also be involved. The QD may still emit radiatively to either the cavity mode or non-cavity modes. However, non-radiative interaction channels are also available, such as tunneling of the exciton to neighboring QDs or interactions with phonons. Since the interest here is merely in providing a proper account of the expected spectrum of the transmission of a weak probe beam, care will not be taken to

distinguish each possible reservoir in detail. A primary contribution to the overall dissipation and dephasing properties of quantum dots does appear to be due to interactions with phonons, however [57, 16].

We will continue development of the theory in an ad-hoc manner, first including the effects of reservoir couplings, then introducing a driving field so that a transmission spectrum may be derived.

2.5.1 Reservoirs

Time evolution for closed systems in quantum mechanics is represented as a one-parameter unitary group. Among other things, this says that for each time evolution operator propagating the system into the future there exists an inverse operator carrying the system back in time. Ignoring the measurement/ collapse problem (which breaks the assumption of a closed system anyway), the dynamics are time-reversal invariant. So far, the model has been closed and the Hamiltonian is the generator of time evolution (i.e $\hat{U}(t, t_0) = \exp[i\hat{\mathcal{H}}(t - t_0)]$).

For many systems studied in quantum optics the assumption of a closed system is not appropriate. Spontaneous emission is a good example of behavior that is not time-reversal invariant and therefore not well described by models involving closed systems.

A successful method of dealing with this is to include interactions between the open system of interest and a reservoir (e.g. an infinite set of oscillators). This leads to non-unitary time-evolution that exhibits an arrow of time. In the case of

unitary time evolution the eigenstates of the Hamiltonian are also eigenstates of the time evolution operator. A closed system prepared in an energy eigenstate will remain in that state forever.

For the case of an open-system coupled to a reservoir, however, the open system is free to emit energy into the reservoir (or vice versa) until they reach equilibrium (i.e. the likelihood for the open system to emit a quantum of energy into the reservoir is equal to the likelihood of it absorbing a quantum of energy from the reservoir).

$$\begin{array}{ccc}
 \rho(0) = \rho_S(0) \otimes \rho_R & \xrightarrow{\text{unitary evolution}} & \rho(t) = U(t, 0) [\rho_S(0) \otimes \rho_R] U^\dagger(t, 0) \\
 \text{Tr}_R \downarrow & & \downarrow \text{Tr}_R \\
 \rho_S(0) & \xrightarrow{\text{dynamical map}} & \rho_S(t) = V(t) \cdot \rho_S(0)
 \end{array}$$

FIGURE 2.12: Quantum dynamical map. A commutative diagram shows the action of a dynamical map $V(t)$, reproduced from [6].

The commutative diagram shown in figure 2.12 says that time evolution and taking the partial trace over the reservoir are commutative. That is, it doesn't matter in which order we take these two operations. We may calculate the time evolution over the closed system $S \oplus R$ then trace out the reservoir degrees of freedom to find the state of the open sub-system at a later time. Alternatively, and of great practical importance, it is possible to trace out the reservoir in the beginning and calculate the (non-unitary) time evolution of the open sub-system

(S) purely in terms of states and operators that are defined in \mathfrak{H}_S . As is indicated in the diagram, the evolution of S is given by a dynamical map (V).

The expression at the upper left corner of the diagram in figure 2.12 presupposes that the combined system of the subsystem of interest together with the reservoir is factorizable at $t = 0$. In other words, there are no correlation, initially.

Commutativity requires that

$$\rho_S(t) = V(t)\rho_S(0) \equiv \text{tr}_R \left\{ \hat{U}(t, 0)[\rho_S(0) \otimes \rho_R]\hat{U}^\dagger(t, 0) \right\}.$$

If it is assumed that the reservoir is large enough that its state does not depend on the interactions with the subsystem (which in this case can be considered to contain only a single quantum of energy), then $\forall t > 0, V(t) : \mathfrak{H}_S \rightarrow \mathfrak{H}_S$. That is, it defines a map from \mathfrak{H}_S into itself for time translations into the future (but not the past). It is clear from the commutative diagram that the dynamical map V must involve only operators in \mathfrak{H}_S .

2.5.2 Approximations

In pursuit of a formulation of the dynamics of the open-system in terms of a master equation in the Lindblad form, it is necessary to invoke some approximations. Three approximations are generally needed to obtain a quantum master equation in the Lindblad form [6, 7]:

1. The Born approximation involves only working to second order in the terms that couple the system to the reservoir. This is justified if the couplings are weak.
2. The Markov approximation requires the existence of two widely separated time-scales. The time-scale over which the system is to be examined must greatly exceed the time-scale over which correlations in the reservoir persist. The Markov approximation allows for a description that is local in time, it is equivalent to taking the two-time correlation function for reservoir operators to be a delta-function.

$$\langle \hat{\tilde{b}}_i(t) \hat{\tilde{b}}_j(t') \rangle_R \propto \delta(t - t'),$$

where tilde indicates operators in the interaction picture.

3. The rotating-wave approximation was made already when deriving the Jaynes-Cummings Hamiltonian. It is necessary to make the same approximation for the couplings between the system and reservoir in order to derive a master equation in the Lindblad form from a Born-Markov master equation.

If each of these approximations may be justified, then the quantum dynamical map $V(t)$ may be described as an element of a quantum dynamical semigroup.

$$V(t_1) \cdot V(t_2) = V(t_1 + t_2), \quad \text{for } t_1, t_2 \geq 0. \quad (2.77)$$

Here, t_1 and t_2 label changes in time. The dynamical map for the time evolution of the open subsystem depends only on the total time elapsed between the initial state and the final state. It does not depend on the particular times involved. The dynamical map may be said to be independent of history, consistent with the Markov approximation.

Under these conditions, it may be assumed that the dynamical map V , belonging to a semi-group, may be formulated in terms of an infinitesimal generator of the semi-group. That is,

$$V(t) = \exp[\mathcal{L}t].$$

Then, in terms of the generator \mathcal{L} of the semigroup, we may write

$$\frac{d}{dt}\hat{\rho}_S = \mathcal{L}\hat{\rho}_S. \quad (2.78)$$

Since we are assuming that the Born-Markov approximation and the RWA hold, we may assert that the generator, \mathcal{L} , is in the Lindblad form. In this case, we may write (2.78) as:

$$\begin{aligned} \dot{\hat{\rho}} = & \frac{1}{i\hbar} [\hat{\mathcal{H}}, \hat{\rho}] + \frac{\gamma_I}{2} (2\hat{S}_- \hat{\rho} \hat{S}_+ - \hat{S}_+ \hat{S}_- \hat{\rho} - \hat{\rho} \hat{S}_+ \hat{S}_-) \\ & + \kappa (2\hat{a} \hat{\rho} \hat{a}^\dagger - \hat{a}^\dagger \hat{a} \hat{\rho} - \hat{\rho} \hat{a}^\dagger \hat{a}) \\ & + \frac{\gamma_p}{2} (\hat{\sigma}_z \hat{\rho} \hat{\sigma}_z - \hat{\rho}). \end{aligned} \quad (2.79)$$

The term weighted by γ_p is a phenomenological pure dephasing term as discussed in [8].

The time evolution of expectation values can then be calculated in the following way:

$$\begin{aligned} \langle \dot{\hat{O}} \rangle = \text{tr} \left(\dot{\hat{\rho}} \hat{O} \right) = \text{tr} \left(\frac{1}{i\hbar} [\hat{\mathcal{H}}, \hat{\rho}] \hat{O} + \frac{\gamma_I}{2} (2\hat{S}_- \hat{\rho} \hat{S}_+ - \hat{S}_+ \hat{S}_- \hat{\rho} - \hat{\rho} \hat{S}_+ \hat{S}_-) \hat{O} \right. \\ \left. + \kappa (2\hat{a} \hat{\rho} \hat{a}^\dagger - \hat{a}^\dagger \hat{a} \hat{\rho} - \hat{\rho} \hat{a}^\dagger \hat{a}) \hat{O} \right. \\ \left. + \frac{\gamma_p}{2} (\hat{\sigma}_z \hat{\rho} \hat{\sigma}_z - \hat{\rho}) \hat{O} \right). \end{aligned} \quad (2.80)$$

The coupling to the reservoirs has the effect of coupling the single quantum manifold to the vacuum state, $|0, b\rangle$. The density matrix for the scenario under consideration may thus be expanded in a basis consisting of three states. In other words, coupling to reservoirs causes the decoupling between the subspaces of the closed system model to no longer be rigorously observed. The Hamiltonian now contains terms that couple these blocks to each other and provide for transition to lower energy manifolds. Starting off in the single quantum manifold, the Hilbert space for the open subsystem is now spanned by three states:

$$\{|0, b\rangle, |1, b\rangle, |0, a\rangle\} \rightarrow \left\{ \begin{bmatrix} 1 \\ 0 \\ 0 \end{bmatrix}, \begin{bmatrix} 0 \\ 1 \\ 0 \end{bmatrix}, \begin{bmatrix} 0 \\ 0 \\ 1 \end{bmatrix} \right\}$$

The quantum state in this 3-state basis can be written as

$$|\psi\rangle = c_1 |0, b\rangle + c_2 |1, b\rangle + c_3 |0, a\rangle \quad \text{for } c_i \in \mathbb{C}. \quad (2.81)$$

In turn the density matrix over the open subsystem looks like

$$\begin{bmatrix} |c_1|^2 & c_1 c_2^* & c_1 c_3^* \\ c_2 c_1^* & |c_2|^2 & c_2 c_3^* \\ c_3 c_1^* & c_3 c_2^* & |c_3|^2 \end{bmatrix}$$

where due to the orthonormality of the basis we can consider the matrix to be a sum over the 9 outer products of the basis vectors (i.e. an expansion over the matrix elements). For example, the term $c_1 c_2^*$, due to

$$c_1 c_2^* |0, b\rangle\langle 1, b| = c_1 c_2^* \begin{bmatrix} 0 & 1 & 0 \\ 0 & 0 & 0 \\ 0 & 0 & 0 \end{bmatrix}$$

is one such matrix element.

It turns out that each of these matrix elements may be interpreted as the expectation value of an operator defined on the subspace. For example, the matrix element depicted above is associated with an overlap between the states $|0, b\rangle$ and $|1, b\rangle$. We may demonstrate that this corresponds directly to the expectation value

of the annihilation operator. The expectation values of higher moments are zero in the restricted subspace.

$$\langle \hat{a} \rangle = \langle \psi | \hat{a} | \psi \rangle = c_1 \langle \psi | 0, b \rangle = c_1 c_2^*$$

The five³ independent components of the density matrix may each be written down similarly in terms of expectation values of operators.

$$[\hat{\rho}] = \begin{bmatrix} 1 - \langle \hat{a}^\dagger \hat{a} \rangle - \langle \hat{S}_+ \hat{S}_- \rangle & \langle \hat{a} \rangle & \langle \hat{S}_- \rangle \\ \langle \hat{a}^\dagger \rangle & \langle \hat{a}^\dagger \hat{a} \rangle & \langle \hat{a}^\dagger \hat{S}_- \rangle \\ \langle \hat{S}_+ \rangle & \langle \hat{a} \hat{S}_+ \rangle & \langle \hat{S}_+ \hat{S}_- \rangle \end{bmatrix}$$

By specifying an initial condition in this Hilbert space, one may formulate a well-posed initial value problem. This is a necessary course of action if one wishes to study the emissive properties of the CQED system. Though the goal here is to obtain a transmission spectrum rather than a spontaneous emission spectrum, it will be worthwhile to pause here to calculate the mean-value equations for the \hat{a} and \hat{S}_- operators. These may be calculated as shown in (2.80).

The calculations are worked out in appendix A. As can be seen from (A.6) and (A.7), the annihilation operator and the lowering operator for the quantum dot are

³Hermiticity reduces the number of independent components of the matrix to 6 (from 9). Normalization ($\text{tr}[\hat{\rho}] = 1$) makes one of the diagonal matrix elements linearly dependent on the other two.

coupled. The pair of equations may be written in matrix form as follows:

$$\frac{d}{dt} \begin{bmatrix} \langle \hat{a} \rangle \\ \langle \hat{S}_- \rangle \end{bmatrix} = \begin{bmatrix} -(\kappa + i\nu) & ig \\ ig & -(\Gamma + i\omega) \end{bmatrix} \begin{bmatrix} \langle \hat{a} \rangle \\ \langle \hat{S}_- \rangle \end{bmatrix}. \quad (2.82)$$

The general solution of a linear, homogeneous system of differential equations ($\dot{\mathbf{y}} = \mathbf{M} \cdot \mathbf{y}$) is given by $\mathbf{y} = A\mathbf{v}_1 \exp[\lambda_1 t] + B\mathbf{v}_2 \exp[\lambda_2 t] + C$, where λ_i and \mathbf{v}_i are eigenvalues and eigenvectors generated by \mathbf{M} . The eigenvalues are

$$\lambda_{\pm} = -\frac{\kappa + \Gamma}{2} - i\frac{\omega + \nu}{2} \pm \frac{1}{2}\sqrt{(\kappa - \Gamma - i\Delta)^2 - 4g^2} \quad (2.83)$$

For certain values of κ , Γ and g , the time evolution may be seen to be governed by a complex eigenvalue and thus corresponds to damped harmonic motion. So, without solving the problem in detail, it's already evident that the behavior of the undriven system corresponds to either damped harmonic time evolution or to pure exponential decay, depending on whether the eigenvalues are complex or purely real, respectively.

2.5.3 Input-Output Formalism

The experiment that we wish to model is the transmission spectrum of a weak probe beam through the coupled cavity/emitter system. In pursuit of this, we now expand upon the damped Jaynes-Cummings Hamiltonian considered so far. The intracavity field will be connected to the probe field via transmission. Similarly, the intracavity field drives a pair of output fields via transmission.

First consider the coupling to an input probe field. The interaction that transfers energy from one mode to the other is transmission at the input mirror. Input and output both involve interactions with reservoir modes. The interaction

Hamiltonian that couples the intracavity mode to the input probe field and to the output field that will be measured by a detector is the same Hamiltonian that generates dissipation and dephasing.

$$\hat{\mathcal{H}}_{SR} = \hbar \sum_k \kappa_k \hat{a}^\dagger \hat{r}_k + \kappa_k^* \hat{a} \hat{r}_k^\dagger \quad . \quad (2.84)$$

It is appropriate to consider the reservoir modes as traveling waves obeying periodic boundary conditions along one dimension. These traveling modes thus have field operators whose amplitudes depend on the volume of a box with length L' . The box defines a natural length scale for the density of states. In particular, a wave entering the box on one end will end up in the same state at the other side of the box. The reciprocal of this crossing time defines a FSR of $\frac{c}{L'}$, where L' is the length of the box (we can take $\lim_{L' \rightarrow \infty}$ later). This is the frequency difference between reservoir modes and leads directly to a density of states (over angular frequency), which will be used later:

$$g(\omega) = \frac{L'}{2\pi c}. \quad (2.85)$$

We consider a reservoir mode coupled to one mirror as the input probe beam. Assume that one mode with angular frequency ω_L is in a coherent state, with all other modes in the vacuum state. In this situation, the one input mode can be merged into the Hilbert space, leaving the rest of the vacuum modes to contribute

via the Lindblad form. The interaction with the probe beam can then be written as

$$\hat{\mathcal{H}}_{\text{Probe Int.}} = \hbar \left(\kappa_k \hat{a}^\dagger \hat{r}_k + \kappa_k^* \hat{a} \hat{r}_k^\dagger \right) \Big|_{\omega_k = \omega_L}. \quad (2.86)$$

Due to the linearity of the trace, the contribution to the rate equations can be calculated separately. The Hilbert space now may be considered to be

$$\mathfrak{H} = \mathfrak{H}_{\text{QD}} \otimes \mathfrak{H}_{\text{Field}} \otimes \mathfrak{H}_{\text{Probe}}.$$

The fact that the input field is a coherent state means that the mean value of the envelope of the probe field is the displacement parameter. This allows a simple calculation of the probe field contribution to the time evolution of the intracavity field.

$$\begin{aligned} \frac{d\langle \hat{a} \rangle}{dt} &= \frac{1}{i\hbar} \text{tr} \left\{ \left[\hat{\mathcal{H}}_{\text{Probe Int.}}, \hat{\rho} \right] \hat{a} \right\} \\ &= \frac{\hbar \kappa_{\omega_L}}{i\hbar} \text{tr} \left\{ \left[\hat{a}^\dagger \hat{r}_{\omega_L}, \hat{\rho} \right] \hat{a} \right\} \\ &= -i\kappa_{\omega_L} \text{tr} \left\{ \hat{a}^\dagger \hat{r}_{\omega_L} \hat{\rho} \hat{a} - \hat{\rho} \hat{a}^\dagger \hat{r}_{\omega_L} \hat{a} \right\} \\ &= -i\kappa_{\omega_L} \text{tr} \left\{ \hat{\rho} \left(\left[\hat{a}, \hat{a}^\dagger \right] \hat{r}_{\omega_L} \right) \right\} \\ &= -i\kappa_{\omega_L} \langle \hat{r}_{\omega_L} \rangle \\ \frac{d\langle \hat{a} \rangle}{dt} &= -i\kappa_{\omega_L} \beta e^{-i\omega_L t}, \end{aligned} \quad (2.87)$$

where β is the displacement parameter of the coherent state produced by the probe laser.

We are now in a position to determine the steady state solution of the mean field inside of the cavity. By including (2.87) in the damped rate equations given in (2.82), we obtain a pair of rate equations for the driven CQED system.

The resulting rate equations for the mean values of the field and quantum dot polarization operators are

$$\frac{d}{dt} \begin{bmatrix} \langle \hat{a} \rangle \\ \langle \hat{S}_- \rangle \end{bmatrix} = \begin{bmatrix} -(\kappa + i\nu) & ig \\ ig & -(\Gamma + i\omega) \end{bmatrix} \begin{bmatrix} \langle \hat{a} \rangle \\ \langle \hat{S}_- \rangle \end{bmatrix} + \begin{bmatrix} -i\kappa_{\omega_L}\beta e^{-i\omega_L t} \\ 0 \end{bmatrix}. \quad (2.88)$$

This is a non-homogeneous system of first order differential equations. It is possible to solve these equations directly and get the time dependent solutions. This would be necessary for describing experiments sensitive to transient behavior. In this case, where we probe the CQED system with a continuous-wave (CW) beam, we are only interested in the steady state behavior.

2.5.3.1 Steady-state solutions

In order to find a steady state solution, transform into a frame rotating at the frequency of the driving field. This permits a static solution in terms of the slowly varying envelope of the input field. The rate equations for the mean field and mean

polarization can be found by using the chain rule:

$$\begin{aligned}\langle \hat{\tilde{a}} \rangle &= \langle \hat{a} \rangle e^{i\omega_L t} &\Rightarrow \frac{d\langle \hat{\tilde{a}} \rangle}{dt} &= \frac{d\langle \hat{a} \rangle}{dt} e^{i\omega_L t} + i\omega_L \langle \hat{\tilde{a}} \rangle \\ \langle \hat{\tilde{S}}_- \rangle &= \langle \hat{S}_- \rangle e^{i\omega_L t} &\Rightarrow \frac{d\langle \hat{\tilde{S}}_- \rangle}{dt} &= \frac{d\langle \hat{S}_- \rangle}{dt} e^{i\omega_L t} + i\omega_L \langle \hat{\tilde{S}}_- \rangle.\end{aligned}\quad (2.89)$$

Using (2.89) with (2.88) we obtain rate equations in the rotating frame.

$$\frac{d}{dt} \begin{bmatrix} \langle \hat{\tilde{a}} \rangle \\ \langle \hat{\tilde{S}}_- \rangle \end{bmatrix} = \begin{bmatrix} -(\kappa + i(\nu - \omega_L)) & ig \\ ig & -(\Gamma + i(\omega - \omega_L)) \end{bmatrix} \begin{bmatrix} \langle \hat{\tilde{a}} \rangle \\ \langle \hat{\tilde{S}}_- \rangle \end{bmatrix} + \begin{bmatrix} -i\kappa\omega_L\beta \\ 0 \end{bmatrix}. \quad (2.90)$$

To find the steady state solutions, set the left-hand side of (2.88) equal to zero – i.e. the rate of change of the dynamical quantities vanishes. This converts the system of ordinary differential equations (ODEs) into a linear system of algebraic equations:

$$\begin{bmatrix} -(\kappa + i(\nu - \omega_L)) & ig \\ ig & -(\Gamma + i(\omega - \omega_L)) \end{bmatrix} \begin{bmatrix} \langle \hat{\tilde{a}} \rangle \\ \langle \hat{\tilde{S}}_- \rangle \end{bmatrix} = \begin{bmatrix} i\kappa(\omega_L)\beta \\ 0 \end{bmatrix}. \quad (2.91)$$

This can be solved by substitution or Gaussian elimination. The resulting steady-state solution for the mean field is

$$\langle \hat{\tilde{a}} \rangle_{ss} = \frac{-i\kappa(\omega_L)\beta(\Gamma + i(\omega - \omega_L))}{g^2 + (\kappa + i(\nu - \omega_L))(\Gamma + i(\omega - \omega_L))}. \quad (2.92)$$

In order to calculate the transmission spectrum, the output field generated by the input field needs to be determined.

2.5.4 Transmission Spectrum

To calculate the transmission spectrum the output field needs to be compared to the input field. The output field couples to the intracavity field in the same way as the input field, via (2.84). When treating the input field, it was possible to simplify the analysis considerably by specifying that the input field was vacuum except for a single mode that coupled to the intracavity mode. Now that we have found the steady state cavity mean field, it is necessary to permit interaction with many output modes. In order to treat the output modes, we will use a Heisenberg picture approach to find the time evolution of the output reservoir mode operators in terms of the intracavity mode operators. This subsection follows the treatment in [9] closely.

The self energy for the reservoir modes is simply

$$\hat{\mathcal{H}}_R = \hbar \sum_k \kappa_k \hat{a}^\dagger \hat{r}_k + \kappa_k^* \hat{a} \hat{r}_k^\dagger.$$

The time evolution of the operator \hat{r}_k may then be calculated by evaluating its commutator with the Hamiltonian:

$$\frac{d\hat{r}_k}{dt} = \frac{1}{i\hbar} [\hat{r}_k, \mathcal{H}_R + \mathcal{H}_{SR}]$$

$$= \frac{-i\mathcal{H}}{\mathcal{H}} \left[\hat{r}_k, \sum_{k'} \left(\omega_{k'} \hat{r}_k^\dagger \hat{r}_{k'} + \cancel{\kappa_{k'} \hat{a}^\dagger \hat{r}_{k'}} + \kappa_{k'}^* \hat{a} \hat{r}_{k'}^\dagger \right) \right].$$

One of the terms in the sum has been eliminated because $[\hat{r}_k, \hat{r}_{k'}] = 0$. Further, because $[\hat{r}_k, \hat{r}_{k'}^\dagger] = \delta_{kk'}$, the sum may be truncated to include only the term $k' = k$.

$$\begin{aligned} \frac{d\hat{r}_k}{dt} &= -i \left[\omega_k \underbrace{\left(\hat{r}_k \hat{r}_k^\dagger \hat{r}_k - \hat{r}_k^\dagger \hat{r}_k \hat{r}_k \right)}_{[\hat{r}_k, \hat{r}_k^\dagger] \hat{r}_k} + \kappa_k^* \hat{a} \underbrace{\left(\hat{r}_k \hat{r}_k^\dagger - \hat{r}_k^\dagger \hat{r}_k \right)}_{[\hat{r}_k, \hat{r}_k^\dagger]} \right] \\ \frac{d\hat{r}_k}{dt} &= -i\omega_k \hat{r}_k - i\kappa_k^* \hat{a}. \end{aligned}$$

This first-order non-homogeneous differential equation can be solved by the method of integrating factors. Rewrite the above result with the non-homogeneous driving term on one side, so that it has the form $y' + P(x)y = Q(x)$.

$$\frac{d\hat{r}_k}{dt} + i\omega_k \hat{r}_k = -i\kappa_k^* \hat{a}.$$

Proceed by multiplying through by an appropriate integrating factor that will allow the left-hand side to be expressed as a complete derivative. The integrating factor will be of the form $\int P(x)dx$. In this case, the integrating factor is $e^{i\omega_k t}$.

Multiplying the above equation by this integrating factor, we obtain

$$\begin{aligned} e^{i\omega_k t} \frac{d\hat{r}_k}{dt} + i\kappa_k^* e^{i\omega_k t} \hat{r}_k &= -i\kappa_k^* \hat{a} \\ \frac{d(e^{i\omega_k t} \hat{r}_k)}{dt} &= -i\kappa_k^* e^{i\omega_k t} \hat{a} \end{aligned}$$

$$\Rightarrow e^{i\omega_k t} \hat{r}_k = C - i\kappa_k^* \int_0^t e^{i\omega_k t'} \hat{a} e^{-i\omega_C t'} dt',$$

where in the last line, we have used $\hat{a} = \hat{a} e^{-i\omega_C t}$ with ω_C denoting the frequency of the cavity mode. Solving for $\hat{r}_k(t)$ we obtain

$$\begin{aligned} \hat{r}_k(t) &= C e^{-i\omega_k t} - i\kappa_k^* \int_0^t \hat{a} e^{i(\omega_k - \omega_C)t'} \cdot e^{-i\omega_k t} dt' \\ &= \hat{r}_k(0) e^{-i\omega_k t} - i\kappa_k^* e^{i\omega_C t} \int_0^t \hat{a} e^{i(\omega_k - \omega_C)(t'-t)} dt'. \end{aligned}$$

In the last line the integration constant has been given the more physical label of $\hat{r}_k(0)$ by requiring that $\hat{r}_k(t)|_{t=0} = \hat{r}_k(0)$.

The reservoir field is

$$\hat{\mathbf{E}}(z, t) = \mathbf{e}_0 \sum_k \sqrt{\frac{\hbar\omega_k}{2\epsilon_0 V'}} \hat{r}_k(t) \cdot \exp\left[i\left(\frac{\omega_k}{c}z + \phi(z)\right)\right],$$

which naturally separates into two pieces; one part due to the free reservoir field, the other due to the intracavity field. In this case, we measure the transmitted field, so the initial reservoir fields are all vacuum and don't contribute to the expectation value of the field. We need only consider the field emanating from the cavity:

$$\begin{aligned} \hat{\mathbf{E}}_{\text{R}}^{(+)}(z, t) &= -i\mathbf{e}_0 \sqrt{\frac{\hbar}{2\epsilon_0 V'}} e^{-i[\omega_C(t-z/c) - \phi(z)]} \\ &\quad \times \sum_k \sqrt{\omega_k \kappa_k^*} \int_0^t dt' \hat{a}(t') e^{i(\omega_k - \omega_C)(t' - t + z/c)}. \end{aligned} \tag{2.93}$$

It is convenient to replace the sum over k with an integral over the density of states. This may be regarded as conversion of a Fourier series into a Fourier transform or as counting of states by integrating the density of states rather than adding up k (i.e. ω/c) values. In any case, we use (2.85) to replace the sum over k with an integral — $\sum_k \rightarrow \int d\omega g(\omega) = \frac{L'}{2\pi c} \int d\omega$:

$$\begin{aligned} \hat{\mathbf{E}}_{\mathbf{R}}^{(+)}(z, t) &= -i\mathbf{e}_0 \sqrt{\frac{\hbar}{2\epsilon_0 AL'}} e^{-i[\omega_C(t-z/c)-\phi(z)]} \\ &\times \frac{L'}{2\pi c} \int_0^\infty d\omega \sqrt{\omega} \kappa^*(\omega) \int_0^t dt' \hat{a}(t') e^{i(\omega_k - \omega_C)(t' - t + z/c)}. \end{aligned} \quad (2.94)$$

To go further, some approximations must be made. In particular, invoke the slowly varying envelope approximation, which says that \hat{a} is almost constant on the time scale of an optical period ($2\pi/\omega_C$). Furthermore, the exponential term oscillates ‘quickly’ for frequencies away from ω_C , leading to cancellation on frequency intervals away from ω_C . Armed with this argument, we set $\sqrt{\omega} \approx \sqrt{\omega_C}$ and $\kappa^*(\omega) \approx \kappa^*(\omega_C)$. This allows (2.94) to be rewritten as

$$\begin{aligned} \hat{\mathbf{E}}_{\mathbf{R}}^{(+)}(z, t) &= -i\mathbf{e}_0 \sqrt{\frac{\hbar\omega_C}{2\epsilon_0 Ac}} \sqrt{\frac{L'}{c}} e^{-i[\omega_C(t-z/c)-\phi(z)]} \kappa^*(\omega_C) \\ &\times \left[\int_0^t dt' \hat{a}(t') \frac{1}{2\pi} \int_0^\infty d\omega e^{i(\omega_k - \omega_C)(t' - t + z/c)} \right] \\ &= -i\mathbf{e}_0 \sqrt{\frac{\hbar\omega_C}{2\epsilon_0 Ac}} \sqrt{\frac{L'}{c}} e^{-i[\omega_C(t-z/c)-\phi(z)]} \kappa^*(\omega_C) \\ &\times \left[\int_0^t dt' \hat{a}(t') \delta(t' - t + z/c) \right]. \end{aligned}$$

For negative values of z , the delta-function selects a value of t' outside of the range of integration. The field operator for reservoir modes emanating from the cavity is

$$\hat{\mathbf{E}}_{\text{R}}^{(+)}(z, t) = \begin{cases} -i\mathbf{e}_0 \sqrt{\frac{\hbar\omega_C}{2\epsilon_0 A c}} \sqrt{\frac{L'}{c}} \kappa^*(\omega_C) \hat{a}(t - z/c) & ct > z > 0 \\ 0 & z < 0 \end{cases} \quad (2.95)$$

Now, the interaction constant $\kappa^*(\omega_C)$ may be determined by imposing a constraint. In steady state, we require that

$$\begin{aligned} \langle \hat{\mathbf{E}}_{\text{R}}^{(+)}(z, t) \rangle &= \sqrt{T} e^{i\phi_T} \langle \hat{\mathbf{E}}_{\text{cav}} \rangle \\ \Leftrightarrow -i \sqrt{\frac{\hbar\omega_C}{2\epsilon_0 A c}} \sqrt{\frac{L'}{c}} \kappa^*(\omega_C) \langle \hat{a} \rangle e^{i\phi_R} &= \sqrt{\frac{\hbar\omega_C}{2\epsilon_0 A L}} \sqrt{T} e^{i\phi_T} \langle \hat{a} \rangle \\ \Leftrightarrow -i \sqrt{\frac{L'}{c}} \kappa^*(\omega_C) e^{i\phi_R} &= \sqrt{\frac{c}{L}} \sqrt{T} e^{i\phi_T} = \sqrt{2\kappa} e^{i\phi_T} \\ \Leftrightarrow \kappa(\omega_C) &= -i \sqrt{\frac{2\kappa c}{L'}} e^{i(\phi_R - \phi_T)}. \end{aligned}$$

Combining (2.95) with (2.92), we obtain the steady-state mean field emitted by the pumped CQED system. Because the intracavity field is proportional to the input field, we replace ω_C with ω_L .

$$\begin{aligned} \langle \hat{\mathbf{E}}_{\text{T}} \rangle &= \sqrt{T} e^{i\phi_T} \sqrt{\frac{\hbar\omega_L}{2\epsilon_0 V}} \frac{-i\kappa(\omega_L)\beta(\Gamma + i(\omega - \omega_L))}{g^2 + (\kappa + i(\nu - \omega_L))(\Gamma + i(\omega - \omega_L))} \\ &= \sqrt{\frac{\hbar\omega_L}{2\epsilon_0 V}} \sqrt{\frac{2\kappa L}{\phi}} \sqrt{\frac{2\kappa\phi}{L'}} e^{i\phi_T} \frac{-\beta(\Gamma + i(\omega - \omega_L))}{g^2 + (\kappa + i(\nu - \omega_L))(\Gamma + i(\omega - \omega_L))} \\ &= \sqrt{\frac{\hbar\omega_L}{2\epsilon_0 V'}} \cdot 2\kappa \frac{-\beta(\Gamma + i(\omega - \omega_L))}{g^2 + (\kappa + i(\nu - \omega_L))(\Gamma + i(\omega - \omega_L))} \end{aligned}$$

Finally, the transmission coefficient is

$$T = \left| \frac{\langle \hat{\mathbf{E}}_T \rangle}{\langle \hat{\mathbf{E}}_{Probe} \rangle} \right|^2 = \left| \frac{\sqrt{\frac{\hbar\omega_L}{2\epsilon_0 V'}} \cdot 2\kappa \frac{-\beta(\Gamma+i(\omega-\omega_L))}{g^2+(\kappa+i(\nu-\omega_L))(\Gamma+i(\omega-\omega_L))}}{\sqrt{\frac{\hbar\omega_L}{2\epsilon_0 V'}} \beta} \right|^2$$

$$T = \left| 2\kappa \frac{(\Gamma+i(\omega-\omega_L))}{g^2+(\kappa+i(\nu-\omega_L))(\Gamma+i(\omega-\omega_L))} \right|^2. \quad (2.96)$$

2.5.4.1 Transmission as a Function of Probe Energy and Cavity-QD Detuning

Figure 2.13 shows (2.96) plotted as a function of probe frequency and cavity-QD detuning. It depicts an aerial view of a 3-dimensional graph. The detuning is plotted in units of μeV while the probe energy is plotted in units of eV. The detuning parameter is $\Delta = \omega - \nu$. The graph is oriented so that the mode energy increases toward the rear of the graph. The plot was generated using $g = 35\mu\text{eV}$, $\kappa = 30\mu\text{eV}$, and $\Gamma = \gamma_I = 15\mu\text{eV}$. The value for the coupling constant (g) corresponds to a mode volume of $50\mu\text{m}^3$ with a modest electric dipole moment of 31 Debye. Cavity decay rate (κ) corresponds to observed finesse and decay rate for the IFQDs is based on observed free-space linewidths. Figure 2.13 is an obvious generalization of figure 2.10, which showed the avoided crossing for the closed-system Jaynes-Cummings energies.

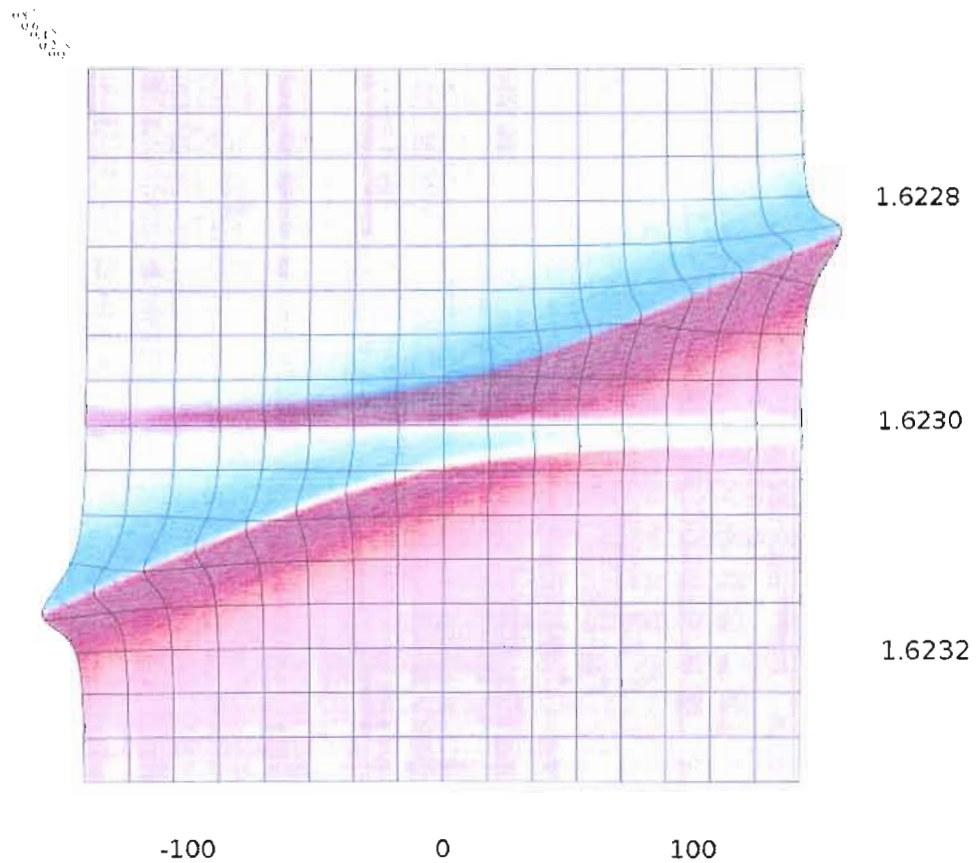


FIGURE 2.13: Transmission spectrum. This plot shows an aerial view of a 3-dimensional plot of the transmission coefficient, as calculated in (2.96), plotted against cavity-QD detuning (x-axis) and probe energy (y-axis). The choice of parameters in this calculation is $g = 35 \mu\text{eV}$, $\kappa = 30 \mu\text{eV}$, and $\Gamma = 15 \mu\text{eV}$, corresponding to best estimates based on anticipated mode volume and observed finesse. The probe energy is plotted in units of eV, while the detuning is in units of μeV .

2.6 Numerical Studies of Non-paraxial Modes

As mentioned previously, the large angular spread of modes in a near-hemispherical cavity violate the conditions for making a paraxial approximation. In order to ascertain the effective mode volume for this experiment, it is necessary to characterize the modes and identify the strength of the electric field at the location of the QDs and this requires the use of various numerical methods.

Through collaboration with the theory group of Murray Holland at the University of Colorado, as well as the theory group of Jens Nöckel at the University of Oregon, we have determined quantitatively the coupling strength between a QD and the mode of our external microcavity. Calculating the mode function is nontrivial, since the field for such a high-numerical aperture (NA) cavity is non-paraxial. As a consequence, this field is not separable into a simple pair of polarization components. Whereas in paraxial systems the polarization may be considered to be roughly independent of the spatial mode, this is not necessarily the case for non-paraxial systems. The non-paraxial field is also not separable into longitudinal and transverse modes.

The computations deal carefully with the structure of the DBR while treating the curved mirror as a simple conductor. While both mirrors consist of Bragg stacks, the field should strike the curved mirror everywhere at normal incidence, so the effects of angle-dependent phase-shifts should be negligible.

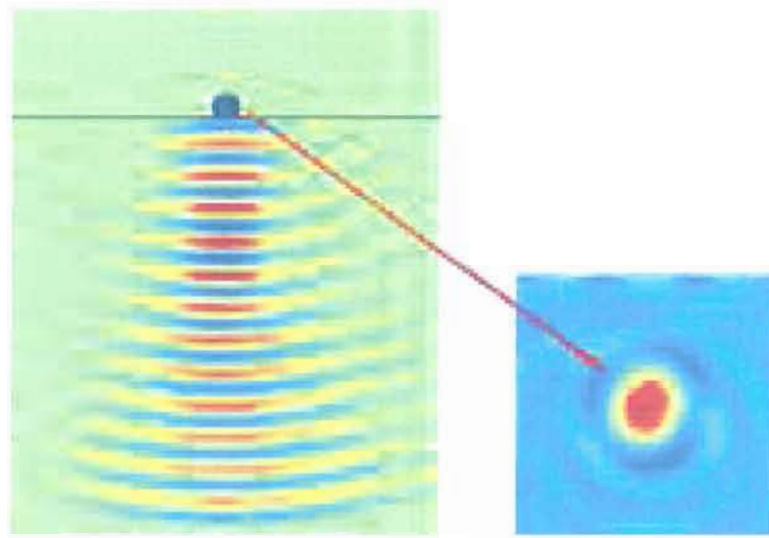


FIGURE 2.14: FDTD calculation of micro-cavity modes. Calculations confirm that the mode waist is on the order of a wavelength near the hemispherical limit.

An example of the finite-difference time-domain (FDTD) method, showing the calculated energy density of the mode in the $y = 0$ plane is shown in figure 2.6. The calculations show that even in the presence of angle-dependent phase shifts, the mode waist in the non-paraxial regime is smaller than one wavelength.

The hybrid method mentioned earlier [20] has produced certain novel predictions. It relies on numerical calculation of E and H values in a plane (say $y = 0$) and azimuthal integration to generate the behavior in other planes.

Near the hemispherical limit, qualitatively new types of modes may be identified. One such mode, a p-polarized “V” mode [18], appears to adiabatically continue from the Gaussian fundamental as the cavity length is varied. This method has also yielded predictions of optical spin-orbit coupling due to mode mixing of nearly degenerate pairs of higher-order transverse modes induced by

polarization-dependent phase shifts (upon reflection from layers in a Bragg stack) that extend into the paraxial regime [19].

Calculations for a 60 μm cavity suggest that working slightly short of the hemispherical limit, where the modes are making the transition from paraxial to non-paraxial, may be beneficial. It appears that a Gaussian mode under paraxial conditions transforms into a p-polarized “V”- mode as the cavity length approaches the radius of curvature of the cavity ($L \approx R$).

A Gaussian beam has transverse spatial distribution and angular distribution (i.e. distribution of wave vector directions) that both obey Gaussian distributions. Figure 2.6 shows the growth of a p-polarized lobe as described in [18] for increasing cavity length. The parameter $z_1 = R - L$ measures the amount by which the length of the cavity is shorter than hemispherical. It can be regarded as a sort of paraxiality parameter in the sense that the modes become more and more paraxial for monotonically increasing z_1 .

Calculations of the field strength for various non-paraxial modes suggest that the field strength for this set of modes has a local maximum at a cavity length shorter than hemispherical. It is also found that of the low order ($|m| = 1$) modes, the maximum of the field strength lies on the optical axis ($\rho = 0$).

Figure 2.16a shows intensity contours for the field in the plane $y = 0$ in a cavity matching our cavity configuration. The mode plotted is similar to a paraxial Gaussian mode but with a non-Gaussian angular distribution of the p-polarized

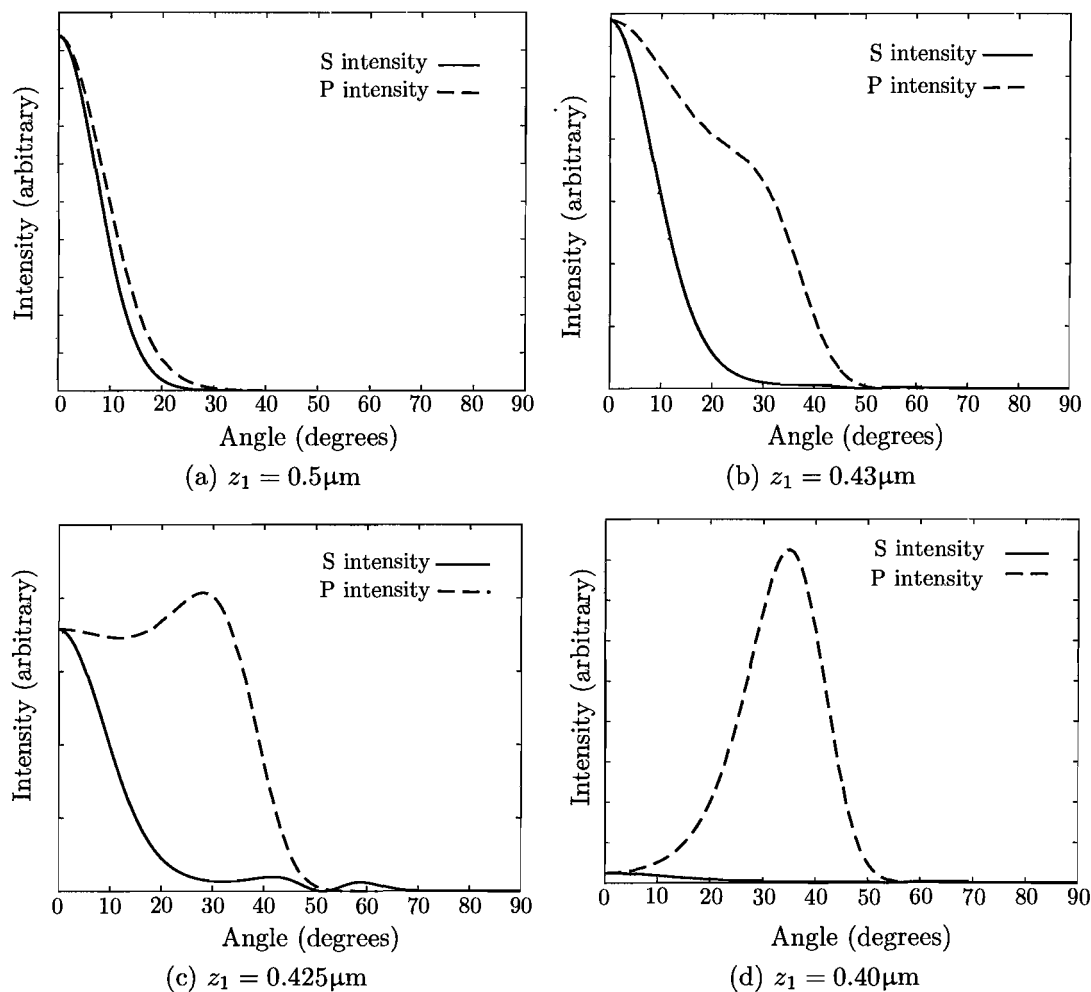


FIGURE 2.15: Gaussian to V-mode transition [17] and [18]. The sequence of plots shows the modification of angular distribution of the lowest order mode as paraxiality of the system is reduced. The angular distribution begins as a Gaussian (a) when $R - L = z_1 = 0.40\mu\text{m}$. The angular distribution becomes non-Gaussian in (b) and (c) and eventually the central lobe disappears, leaving a V-mode in (d).

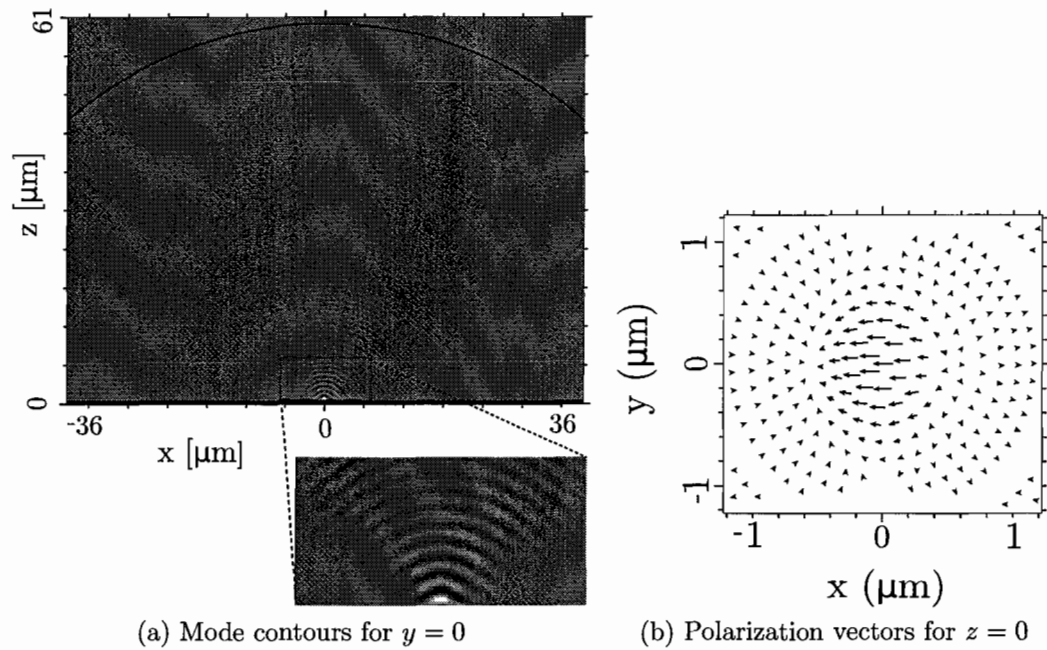


FIGURE 2.16: Amplitude at $y = 0$ and polarization for $z = 0$. In (a), a contour plot shows the amplitude of the field in the plane $y=0$. The calculation assumes a mirror with radius of curvature 60 μm , as used in the experiment, and a cavity length of 59.575 μm , corresponding to 2.15c. Polarization vectors in the plane $z=0$ are shown in (b).

(i.e. transverse magnetic (TM)) component. This mode is the one plotted in figure 2.15c.

Figure 2.16b shows the waist of the mode and demonstrates a couple of things:

- The polarization is linear and the amplitude maximum at radial polar coordinate $\rho = 0$.
- The polarization is slightly non-uniform, with components along the y-axis for points along the $\pm 45^\circ$ directions.

As a result of these investigations we have a good idea of the electric field strength at the location of the quantum dots. Fortuitously, the simulations also indicate that the mode with the largest amplitude is a continuation of the paraxial Gaussian mode, at least for the NA supported by the current set of mirrors.

Another mode, called VTE (V-mode with transverse-electric polarization) has even higher amplitude on the optical axis but is inaccessible to the current optics because the angular spectrum extends to angles not covered by the current mirrors.

For the hybrid Gaussian-VTM mode, the polarization on the optical axis is linear and this may be easily oriented to align with the dipole moment of the IFQDs.

For cavity lengths very close to hemispherical the amplitude of the field on the optical axis actually decreases, suggesting an advantage to working slightly shorter than hemispherical. A further advantage is that higher-order modes

remain spectrally distinct and the situation is better described in terms of a single mode of the field interacting with a two-level system. At the hemispherical limit the transverse modes with even parity all become degenerate, and treating this situation as a two-level system coupled to a single mode of the electric field becomes less justified. Even though a probe beam can be mode-matched so that it couples to only a single intracavity mode, the QD will still have a set of cavity modes with which to interact and the situation would be better modeled by a set of modes with different coupling constants.

CHAPTER III

THE HEMISPHERICAL MICROCAVITY

In this chapter the various components of the apparatus will be described. Discussion will begin with the microcavity and proceed outward to the larger scale support structure and auxiliary components. Design, construction and assembly considerations will be discussed. The results of characterization measurements, where applicable, will also be provided.

3.1 Flat Semiconductor DBR Containing QDs

One of the reflective surfaces bounding the resonant cavity is a semiconductor DBR containing GaAs QDs. These structures were designed, fabricated and characterized by our collaborators, Hyatt Gibbs and Galina Khitrova, at the University of Arizona.

3.1.1 Semiconductor DBR

Semiconductor planar DBR mirror with exceptionally good surface smoothness and high reflectivity can be grown by molecular beam epitaxy (MBE) techniques [56]. The surface roughness on transverse length scales relevant for our needs ($\sim 1\mu\text{m}$) competes favorably with that of the best super-polished dielectric mirrors

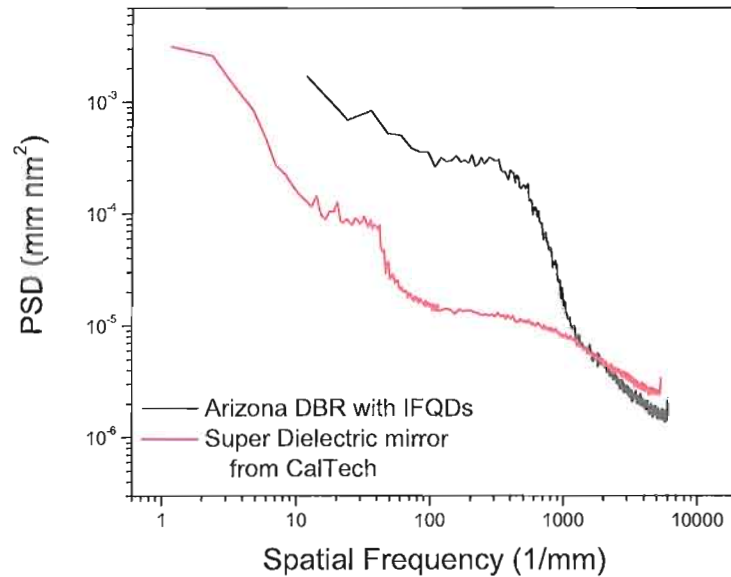


FIGURE 3.1: DBR surface roughness compared with SuperDielectric mirrors. This plot shows the spatial power spectral density for a University of Arizona semiconductor DBR containing IFQDs. A reference SuperDielectric mirror from CalTech is shown for comparison.

of the type used in atomic CQED experiments. Figure 3.1 shows a comparison of the two kinds of mirrors — the MBE-grown DBR and a super-polished dielectric mirror (made by the Kimble group at Caltech). The figure plots the power spectral density (PSD) of surface roughness versus transverse spatial frequency, measured with a Wyko interferometer. It is seen that the planar semiconductor mirror has far larger roughness for low spatial frequencies, while the commercial dielectric mirror is slightly rougher at spatial frequencies above 1000 mm^{-1} ; the region of interest for our cavity, since the mode waist has a radius of less than $1 \mu\text{m}$.

The DBR in the simulation in figure 3.2 is composed of alternating $\frac{\lambda}{4}$ optical thickness layers of AlAs and $\text{Al}_x\text{Ga}_{1-x}\text{As}$. The simulation is of a sample with mole fraction $x = 0.24$ and a stack formula of $(\text{LH})^{30}\text{LHHWHHC}$ where L (H) represents a quarter wave optical thickness layer of the low (high) index of refraction material. W represents a 4 nm quantum well and C represents a thin capping layer of GaAs to discourage oxidation of the the spacer material, which is $\text{Al}_{0.24}\text{Ga}_{0.76}\text{As}$. The second stack adds an anti-reflection coating¹.

Both DBRs used in this work were grown on a GaAs substrate by MBE. Both samples were grown with a stack formula of $\text{LH}^{22}\text{LHHWHHC}$. One sample involves an alloy of $\text{Al}_{0.25}\text{Ga}_{0.75}\text{As}$ for H. The other sample has an alloy of $\text{Al}_{0.24}\text{Ga}_{0.76}\text{As}$ acting as H. W and C denote layers of GaAs; a QW of 3.86 nm thickness and a cap-layer of 3.28 nm thickness, respectively.

Several different mirror structures were grown for use in the cavity-QED study. Several bare DBRs, a DBR with spacer layer but no QDs, and a couple of DBRs containing IFQDs. Each of these structures was grown on a substrate of GaAs via MBE.

While the properties of a stack generally depend on the entire arrangement of layers (indices of refraction, absorption, layer thickness, etc.), in this situation the behavior can roughly be factored into two distinct pieces. A highly reflective

¹The simplest form of this is a $\lambda/4$ thick layer of a material with a lower index of refraction. Optimal performance is achieved when the index of refraction is the geometric mean of the two materials forming an interface.

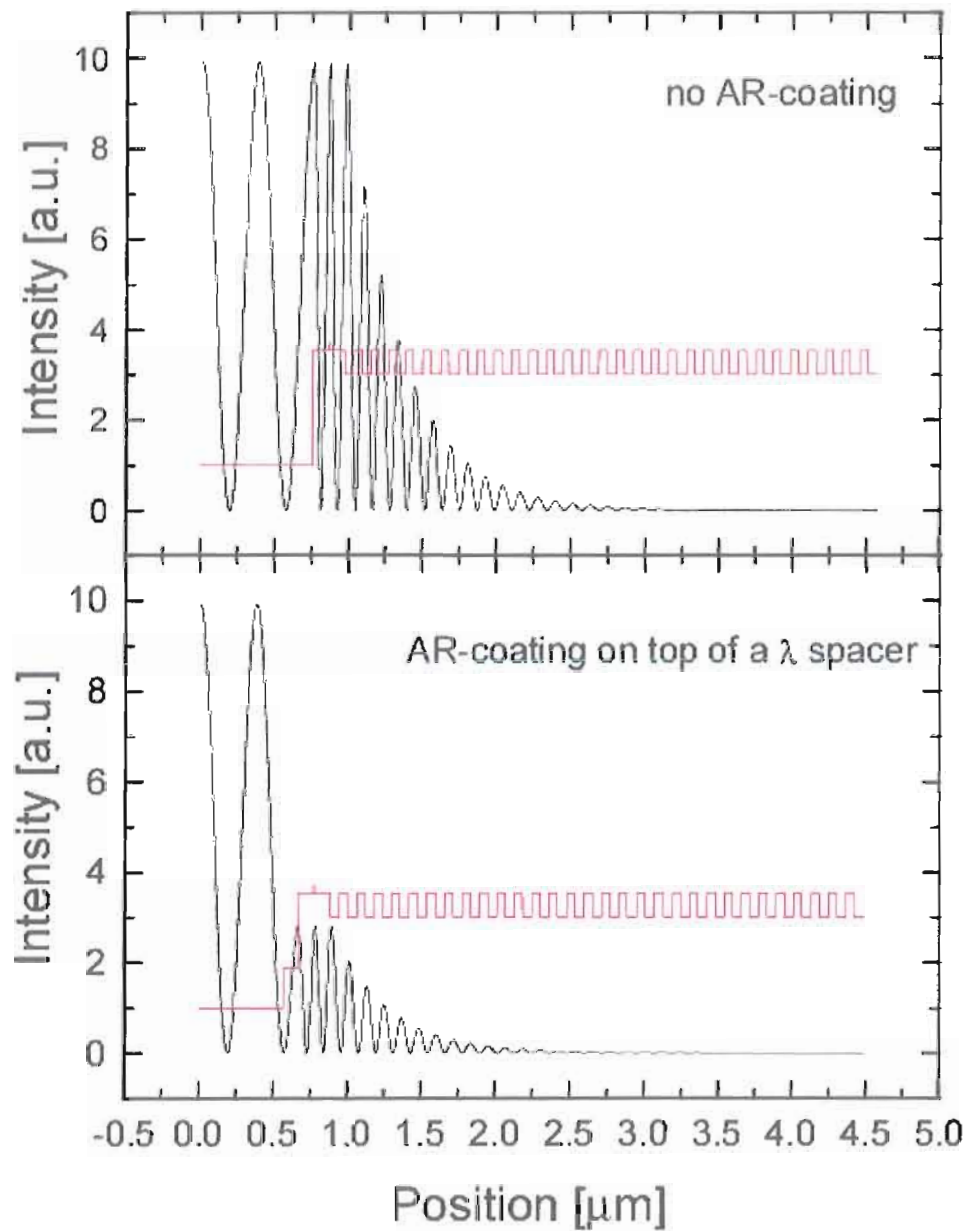


FIGURE 3.2: DBR reflectivity as a function of distance. The red line shows the index of refraction of the structure. The black line shows the electric-field intensity (in arbitrary units). This figure shows the comparison of a DBR with lambda spacer and a DBR with lambda spacer and an anti-reflection coating. This figure illustrates the basic design, though it does not represent the particular stack formula for the sample measured in the accompanying discussion.

stack and a spacer layer of thickness equal to one wavelength of optical path length containing a rough quantum well at its center.

The high-reflector portion of the stack corresponds to $(LH)^{22}L$. Its terminal layers are L to provide for proper inclusion of a spacer layer made of the H material (AlAs). The portion corresponding to HHWHH is a one wavelength spacer layer with a quantum well at its center. This structure will be discussed in the next subsection.

The decay of the transmitted field is evident in both plots. The formula that includes an anti-reflection coating actually has faster attenuation, but the intensity at the location of the quantum dot is reduced. Because the aim is to maximize the coupling constant, g , it is important to maximize the field amplitude at the location of the quantum dot. The samples used in this work do not include an anti-reflection coating for this reason.

3.1.2 Spacer-Layer Containing Quantum Dots

As mentioned in the discussion in chapter 2, the GaAs QDs that we use are interface fluctuation quantum dots. They are formed through the influence of monolayer-thick interface fluctuation during the MBE-growth of a quantum well (QW), creating elliptically shaped regions about 50–100nm across [63, 22].

In order to integrate the emitters into a monolithic mirror structure, the DBR is grown with a quantum well located at the center of a one wavelength (of optical path length) thick spacer layer. The bounding layers of the quantum well are grown

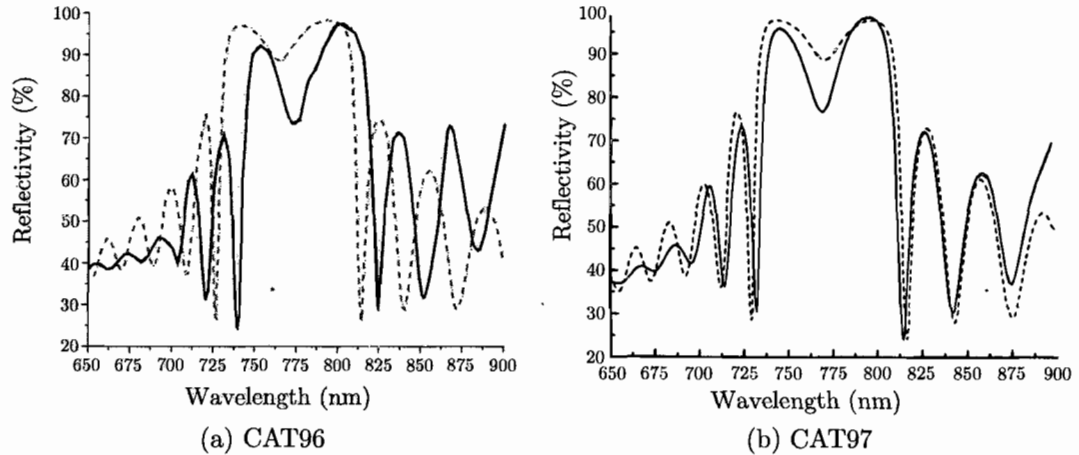


FIGURE 3.3: Reflection spectrum for CAT96 and CAT97. The spectrum for both of the DBRs used in this work are shown. The dip near the center of the stop-band is due to the low-finesse etalon mode.

with two minute growth interruptions. This produces surface irregularities in the quantum well. The purpose of this spacer layer is to enforce that light of the design wavelength will have an antinode occupying the location of the quantum well, as indicated in figure 3.2. Of course, a layer of material of thickness equal to one wavelength of optical path length can be thought of as a Fabry-Perot etalon. Due to the small length of the etalon only one mode is present within the wavelength range probed by this experiment. The reflection spectrum from the mirror exhibits a dip due to the presence of this etalon mode. Free-space measurements taken at room temperature show a reflection coefficient of only about 80%. This dramatic drop is due to buildup of energy in the etalon mode and absorption by the GaAs QW at the antinode. When the semiconductor structure is cooled the etalon resonance shifts to higher energies (shorter length scales), allowing for high-finesse operation of the cavity.

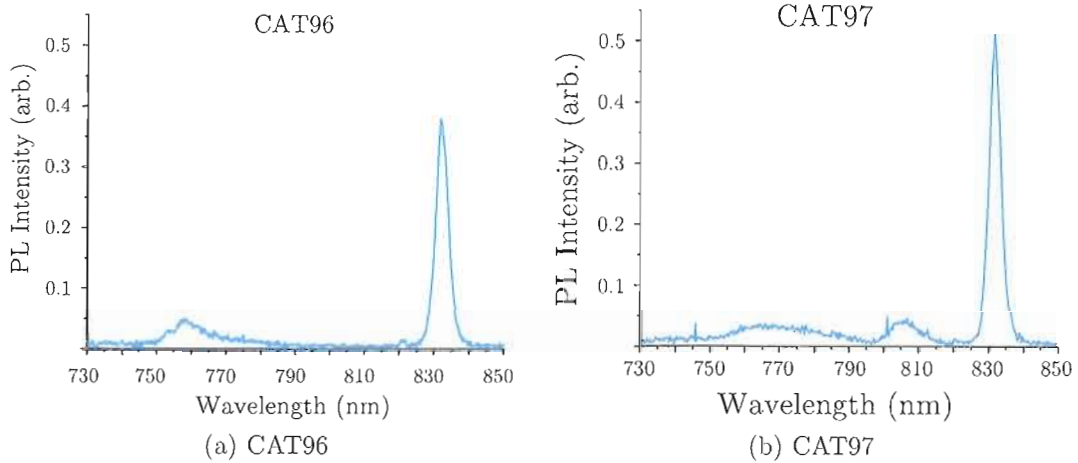


FIGURE 3.4: Micro-PL for CAT96 and CAT97.

The reflectivity of the DBRs is shown in figure 3.3. The theoretical peak is $R = 98.97\%$ for both mirrors.

Micro-PL spectra have also been recorded for both, giving a good idea of the distribution of sizes of the quantum dots. Figure 3.4b shows that the DBR labeled as CAT97 exhibits a broader distribution, as well as a contribution near 805 nm from an unidentified source (possibly some impurities in the substrate).

The areal density of the IFQDs is such that tens to hundreds of them are expected to be found within an area corresponding to the waist of a cavity mode. This rules out spatial selection as a viable method of choosing an individual QD. However, nano-PL measurements indicate that certain positions on a DBR exhibit features consistent with emission from spectrally isolated IFQD.

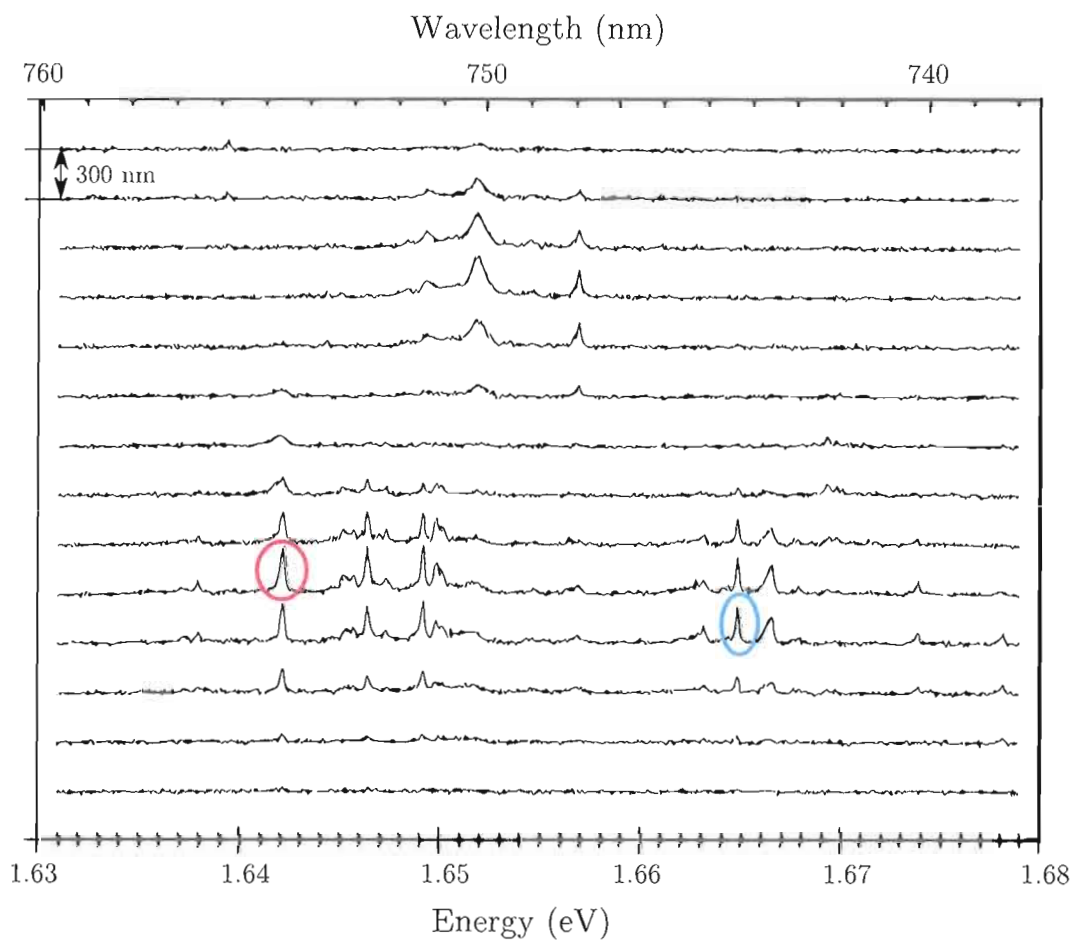


FIGURE 3.5: Nano-PL from CAT97. Each horizontal trace corresponds to nano-PL collected from a different spot on the sample. Each trace is produced by translating the spot by 300 nm and measuring the PL for a particular integration time. The size of the spot is between $0.8 \mu\text{m}$ and $0.44 \mu\text{m}$, as produced by a focused beam from an objective coupled to the surface through a solid-immersion lens. The two circled peaks are good candidates for single, spectrally-isolated quantum dots.

3.2 Large Solid-Angle Micro-mirrors

The cavity is nominally a 50 μm radius of curvature hemispherical cavity. The mode volume for this cavity is of the order of 50 μm^3 .

One of the technical achievements of this experiment is the successful construction of small radius of curvature micro-mirrors. They are constructed of borosilicate glass through a process that will be described below.

3.2.1 Micro-mirror Fabrication

The substrates for the micro-mirrors are the surfaces of tiny bubbles of nitrogen formed in molten glass. The process is outlined below:

- A. Place 50 micro-capillary tubes in a graphite crucible
- B. Bake under dry nitrogen at 1100°C
- C. Polish front side with diamond disc to 6 μm surface roughness to open some dimples
- D. Inspect with a microscope to verify the presence of suitably sized bubbles polished to the correct depth
- E. Polish backside of sample to a thickness of 150–170 μm
- F. Fine polish backside with abrasive slurries to achieve optical finish
- G. Coat surface with high-reflectivity dielectric coating

The bulk of production was done in our lab: Willamette Hall, Room 242; University of Oregon. The bubble formation (glass fusing) was carried out using tube furnaces located in the basement of Klamath Hall at the University of Oregon. The coatings were produced by Spectrum Thin Films Corp..

The micro-capillary tubes are commercially available Drummond Microcaps. The glass is manufactured by Kimble Glass. Manufacturer data is given in the table below.

Glass	Type	Working Pt.	Soften Pt.	Anneal Pt.	Strain Pt.	ρ (g/cc)	n
N-51A	Boro	1140	785	570	530	2.33	1.49

TABLE 3.1: Properties of borosilicate microcaps as reported by Kimble Glass.

Approximately fifty of these tubes are placed in a graphite crucible, which is inserted into a fused-quartz tube for baking. The fused-quartz tube is placed into a programmable tube furnace. A baking program, which consists of a ramp up to 1100°C followed by steady baking at temperature and a slow ramp down (several degrees per minute) was devised, which optimized the bubble size and density for our purposes. By adjusting the baking parameters it is possible to produce samples with bubbles in the range of several tens of microns up to a few hundred microns.

After cooling, the samples are returned to our lab for further preparation. At this stage, the sample is a rounded chunk of glass containing voids of various sizes. The sample is bonded to an aluminum plate with CrystalBond 509 wax (from SPI

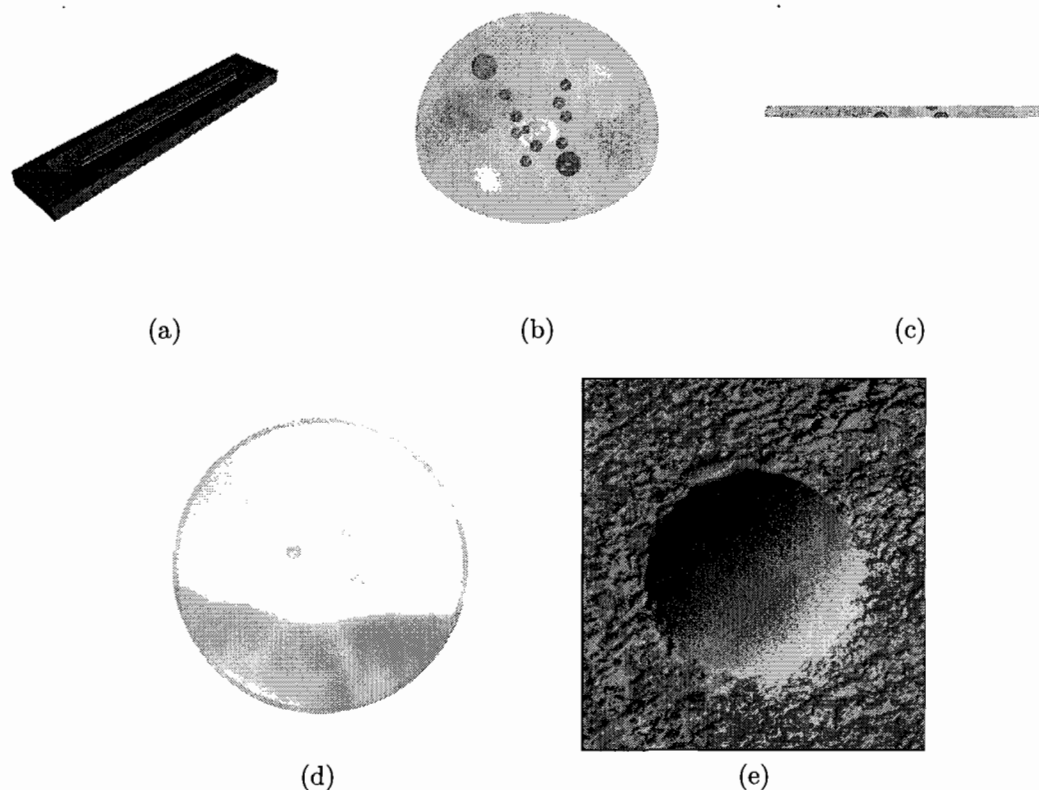


FIGURE 3.6: Micro-mirror substrate preparation. Borosilicate micro-capillary tubes are placed in a graphite crucible (a) and heated under a nitrogen atmosphere in a tube furnace to produce a lump of glass containing bubbles of various sizes (b). This piece of bubbled glass is ground down on both sides to produce a slip of glass of suitable thickness and at least one exposed bubble of suitable radius of curvature and depth (c). The slip of glass has been rotated so that the flat surface faces the page in (d). A photograph shows the surface surrounding one such bubble in (e). The photograph was taken under 40x magnification and shows a bubble with, approximately, a $60\mu\text{m}$ radius of curvature.

Supplies) and ground at a lapping station on a rough diamond wheel (grit size = 15 μm).

When roughly half of the sample has been polished away, the wheel is switched to a 6 μm -grit wheel to reduce the roughness of the surface of the polished surface and to more finely control how much material is removed. At this time, the substrate is inspected under a microscope for candidate bubbles of an appropriate radius of curvature. Polishing proceeds with periodic pauses to check the depth of the remaining bubble surface.

Surfactants are introduced in the water stream to help reduce the chance of glass chips coming into close contact with the bubble surface and adhering due to van der Waals interactions. We have observed that introducing a small amount of dish detergent into the water stream reduces the relative frequency of such glass chips considerably. One may hypothesize that this is due to formation of bilayer and micelle boundaries separating bits of glass from the bubble surface.

Once the depth of the remaining bubble is equal to about half of the radius of curvature of a bubble of suitable size, the sample is inspected for glass chips. We discovered that elastomers may be used to remove some glass chips that remain. The effectiveness of this procedure depends on the shapes of the contaminating glass chips. We used a two-component formulation — liquid PDMS mixed with a cross-linking agent (Sylgard 184 from Dow Corning) — to produce an elastomeric mold of the substrate. Once the elastomer had cured it was carefully pulled away

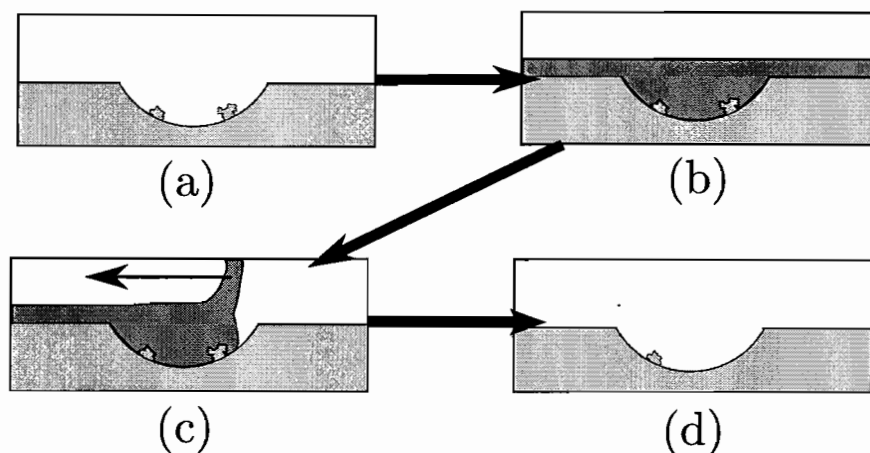


FIGURE 3.7: Procedure for removing glass chips with PDMS films. A view of a bubble surface with glass chip contaminants is shown in (a). First, some PDMS and cross-linking agent are mixed in the prescribed quantities. This is applied to the surface of the glass substrate containing the open bubbles we wish to clean (b). After the elastomer has cured, it is peeled from the surface (c), lifting some glass pieces away with it. In (d) the surface is shown with one of the contaminating glass chips removed.

from the mirror substrate. This process proved to reduce the number of remaining glass particles by about 1/2.

After this process is completed, the substrate is flipped over and mounted to an aluminum disc with Crystalbond 509 wax. The back side is then polished down in a similar fashion. When the thickness is on the order of 150–170 μm , a polishing pad is mounted on the lapping station and polishing continues, using abrasive (colloidal silica) slurries. The process terminates with the use of a slurry with a colloidal suspension of 0.05 μm diameter silica particles, leaving a high-quality optical finish.

It is of interest that the mirror surfaces, themselves, are not polished. Optical finishes are produced naturally as the hot glass seeks equilibrium. This is important

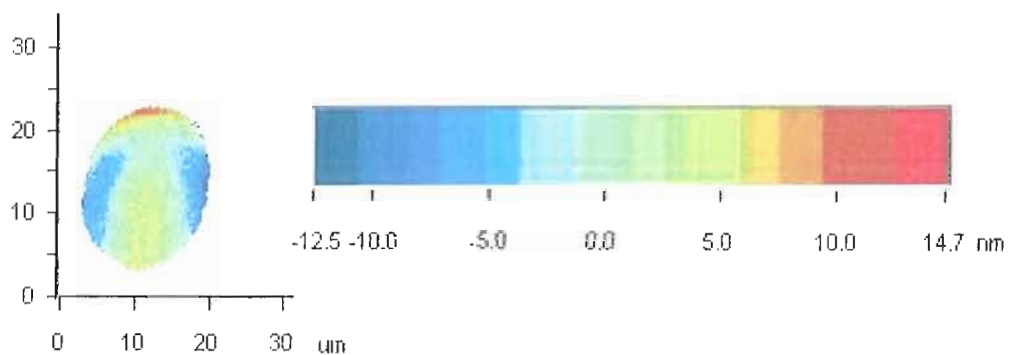
since a good technique for polishing small spherical voids is unknown at this time. There do exist certain schemes for creating spherical voids by wet-etching through apertures but these are expected to produce surfaces with much greater roughness [28].

The rough surface surrounding the dimple is shown in figure 3.6e. This is the surrounding glass substrate which has been polished by the 6 μm grit diamond wheel. The actual surface of the dimple is out of focus due to the depth of focus of the microscope objective. It is important not to apply abrasive slurries to this side of the glass slip, otherwise abrasives will degrade the surface quality of the mirror substrate.

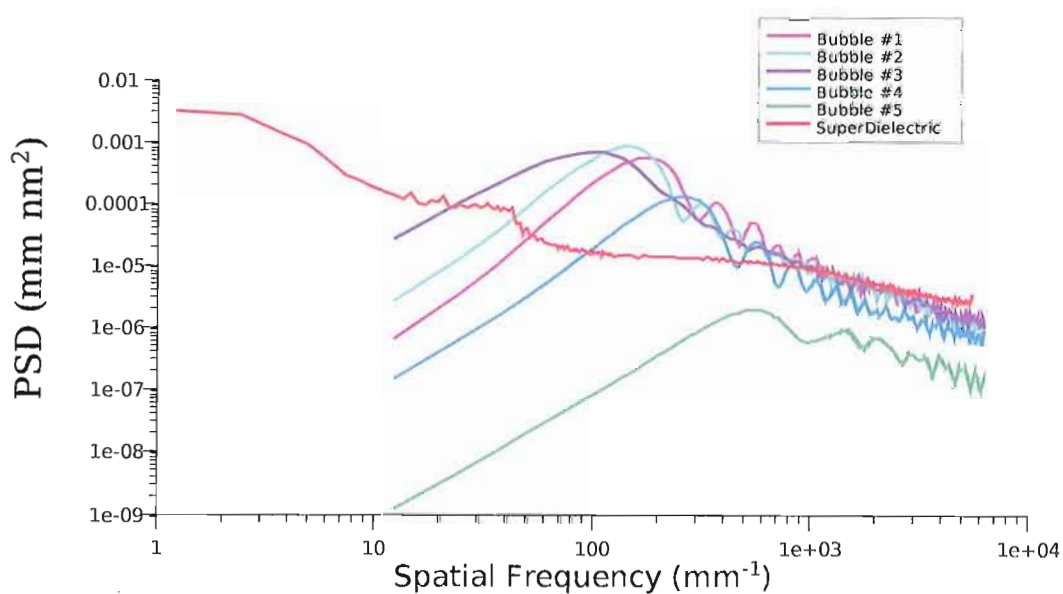
Due to the tiny ratio between the radius of a bubble and the radius of Earth, the magnitude of the tidal force at any point on the bubble's surface will be small. The equilibrium shape of the bubbles is expected to be very close to spherical for this reason. The sphericity has been measured with a Wyko interferometer, see figure 3.8a. At the bottom of a dimple, in a circle of 15 μm diameter, the deviations from spherical were found to be less than 10 nm across the measured region.

3.2.2 Micro-mirror Coating Design

As is clear from the analysis in the theory portion of this dissertation it is important to have high reflectivity (low κ). Moreover, in order to be able to communicate with the device we need the transmission rate to be much larger than



(a) Micro-mirror sphericity



(b) Surface roughness of several (5) micro-mirror substrates compared with the same SuperDielectric mirror as the DBR in figure 3.1.

FIGURE 3.8: Micro-mirror sphericity and surface roughness. This plot shows the deviations of a micro-mirror from spherical (a) and surface roughness (b), as measured by a Wyko interferometer.

absorption or scattering rates. Briefly, we require that $R \gg T \gg A, S$. Moreover, there is a requirement that this hold over a wide range of wave-vector directions, so that high finesse operation can be achieved near the hemispherical limit.

The mirror coatings were produced by Spectrum Thin Films Corporation. The coatings specifications called for greater than 99.5% reflectivity across a frequency range of 740 – 810 nm. A coating deposited by a directional source is expected to exhibit cosine variations in the layer thicknesses. For large angles (away from the center of the concave surface) the thinning of the layers will lead to shifting of the stop-band toward shorter wavelengths. In the interest of maintaining performance out to high angles, it is reasonable to specify a longer wavelength for the center of the stop-band compared with a flat mirror to account for layer thinning at higher angles.

To characterize the performance of the coatings at points away from the center of the concave surface, measurements of the transmission through the mirror coating were made for meridional beams with varying angles with respect to the substrate normal.

Figure 3.9b indicates that the reflectivity is large over a large solid angle.

3.3 Mounted Micro-mirrors

To ease handling and coupling into the cavity, the slip of glass containing the coated micro-mirror is mounted directly to an immersion objective. Norland 88

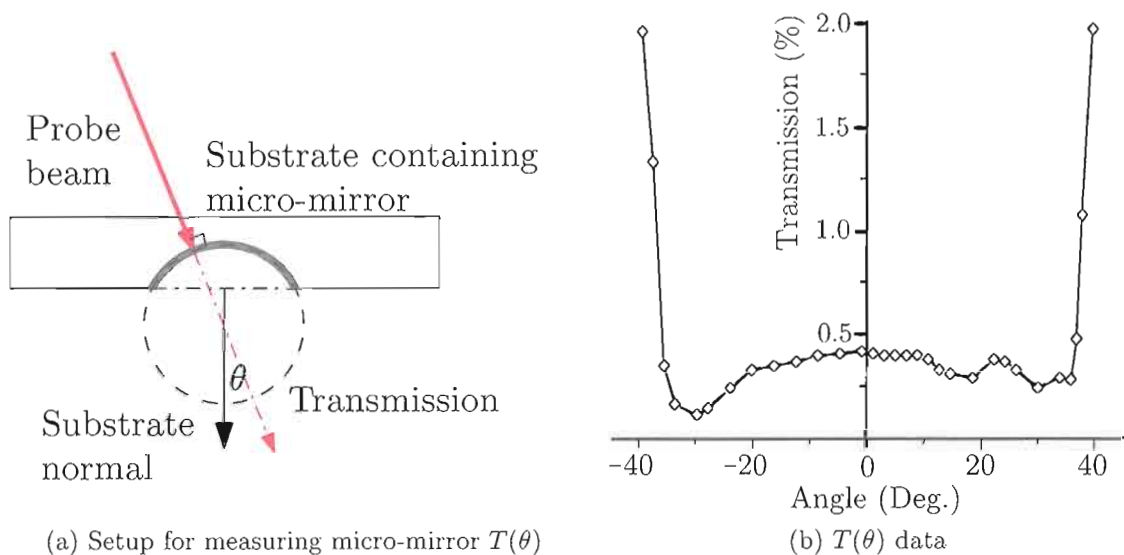


FIGURE 3.9: Micro-mirror $T(\theta)$: Setup and data. In (a) the geometry for measuring transmission is shown. In particular, it defines the angle θ . To collect this data, the beam was focused to a spot and incident at normal incidence to the mirror surface. Each data point was recorded by changing the angle between the mirror substrate normal and the optical axis of the probe beam while maintaining normal incidence with the mirror surface. In (b) the transmission coefficient is plotted for various points along the surface of a micro-mirror. The data shows that transmission remains less than 0.5% for a half-angle greater than 40 degrees.

optical adhesive has an appropriate index of refraction to be used as a kind of rigid immersion fluid. It also has low vapor pressure and is suitable for inclusion in a UHV environment. It is only rated for operation between -60°C and 90°C , yet we have found it to provide good adhesion properties through repeated cycling between room temperature and an operating temperature of about 16 K.

The correct position (working distance) of the micro-mirror is determined with the aid of a Twyman-Green interferometer. This allows reliable positioning of the curved surface to make the job of mode matching easier. Once the correct position has been determined the adhesive is hardened² by illuminating under an ultraviolet lamp. The result is a microscope objective with a highly reflective spherical surface matched to the wavefronts produced when a collimated beam is introduced to the objective's aperture.

This objective can simply be threaded into an appropriate mount and pumped with a collimated beam. If the beam has the correct trajectory then the wavefronts will automatically match the curved mirror. Mode matching is now primarily an issue of steering a collimated beam so that it follows the correct trajectory into the objective.

The mounting process is illustrated in the attending diagram.

²Care should be taken to compensate for the change in the index of refraction of the optical adhesive as it hardens.

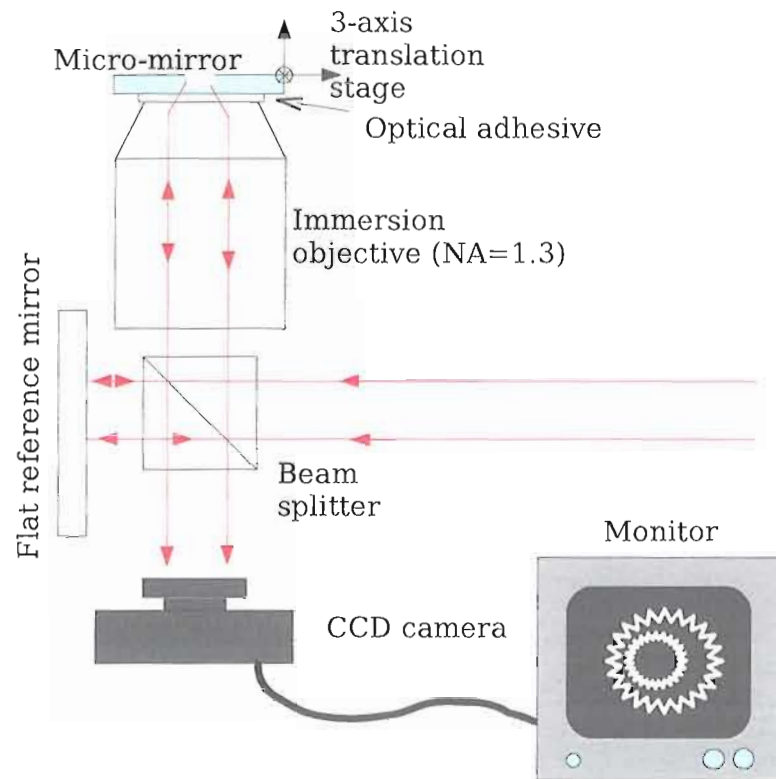


FIGURE 3.10: Twyman-Green interferometer for mounting micro-mirrors. The diagram shows the alignment setup for the micro-mirrors. The interference pattern is collected by a CCD and displayed on a monitor. Proper positioning is achieved when the output interference pattern corresponds to plane wave interference.

3.4 The Near-hemispherical Microcavity

The result of moving the mounted micro-mirror within a suitable distance of the DBR containing QDs is a unique half-monolithic, hemispherical micro-cavity for semiconductor cavity-QED. For mirror separations such that $L \leq R$, the mirror surfaces define a stable resonator. The stability parameters for the resonator are

$$g_1 = 1 - \frac{L}{R_1}$$

$$g_2 = 1 - \frac{L}{R_2},$$

where $0 \leq g_1 g_2 \leq 1$ for a stable resonator. This cavity operates with $g_2 = 1$ due to the flat mirror. At hemispherical, $L = R_1$, so $g_1 = 0$. For decreasing cavity length, g_1 should increase monotonically and the cavity stability parameters approach those of a planar cavity. The shape and solid angle of the micro-mirrors used here prevent $L \ll R$ and an upper bound exists for g_1 . In practice, since the depth of the mirror is roughly half of the radius of curvature, $L \leq R/2$, so that $0 \leq g_1 \leq 1/2$. The range of possible cavity configurations forms a line segment in the first quadrant of the plane parametrized by the cavity stability parameters.

The cavity parameters are in a novel range, tabulated in table 3.2. Cavity-length is limited by the minimum separation allowed by the geometry of the curved mirror.

This cavity design contains two unique features:

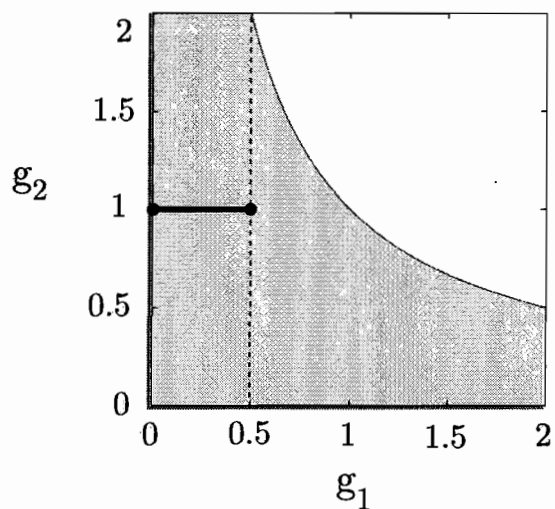


FIGURE 3.11: Cavity stability parameters. The black line segment indicates the range of possible stability parameters for the micro-cavities described here.

Mode Parameter	Symbol	Quantity
Cavity length (μm)	L	40 – 60
Finesse	\mathcal{F}	200 ^a
Waist radius (μm)	w_0	≈ 1
Divergence angle (deg.)	θ_D	± 40
F/number	$f/\#$	≈ 1

TABLE 3.2: Micro-cavity parameters. Properties of modes supported by a near-hemispherical micro-cavity.

^aThis should be amenable to increase by an order of magnitude by using higher reflectivity coatings.

1. The use of a concave micro-mirror with high-reflectivity over a large solid-angle.
2. The use of an integrated DBR mirror containing the QD sample in an external-cavity configuration.

The 40 – 60 μm curved-mirror substrate has a high degree of sphericity and an excellent surface quality, enabling the application of a custom-designed, multilayer, dielectric coating with 99.5% reflectivity over a high solid angle. Such large solid angle is unique compared with, for example, a recently reported half-monolithic micro-cavity design [59].

The radius of the mode waist, located at the planar mirror, is denoted w_0 . Since the QD is to be placed in this waist, this radius should be minimized in order to maximize the coupling between the QD and the field. The angular half-width of the cavity mode is θ_C . Diffraction dictates that the smaller w_0 is made, the larger θ_C becomes. When w_0 equals one optical wavelength, the angle θ_C is roughly 40 degrees.

The effective mode volume V_{eff} , which depends on the location of the QD, is defined as a spatial integral of the field intensity, normalized to unity at the location of the QD. For example, if the transverse spatial distribution of the field amplitude can be described as a (paraxial) Gaussian function (or equivalently, if the angular distribution of the mode is Gaussian) with 1/e contours that define a

spot size $w(z)$ at a position z along the cavity axis, then the effective mode volume will be $V_{\text{eff}} = \frac{\pi w_0^2 L}{4}$, as determined in appendix B.

3.5 Tripod Support System

The mirrors of our cavity must be positioned with respect to each other. For this purpose a tripod system has been devised which will allow positioning of the flat semiconductor DBR with respect to the curved micro-mirror. This structure must allow for coarse as well as fine positioning of the sample mirror. The design must also allow the sample to be cooled to cryogenic temperatures. To avoid cooling the entire experiment this mirror must be thermally isolated from the rest of the experiment.

The requirements for the support system include:

- A. Control over translations and rotations
- B. Long range of travel in z-direction
- C. Low vapor-pressure materials to comply with UHV requirements
- D. Remotely operable [via computer]
- E. Minimal vibrational coupling to environment
- F. Suitable thermal isolation to allow cooling of a minimal amount of material

Operation	Role
Lateral translations (along \hat{i} and \hat{j})	Lateral translations provide a means to include different populations of quantum dots in the optical cavity.
Translation along \hat{k}	Translation along \hat{k} are necessary for controlling the cavity length, since \hat{k} roughly points along the optical axis of the cavity. It is also necessary to correct for thermal expansion during cooling, warming.
Pitch and yaw	Pitch and yaw provide for angular pointing of the cavity's optical axis. In principle, they provide a way to align the input optical axis with the cavity's optical axis. These degrees of freedom play a role in mode matching.
Roll	Roll provides a way to rotate the dipole moment of the IFQDs with respect to the polarization axis of the electric field.

TABLE 3.3: This table lists the relevant degrees of freedom for the cavity along with a description of the role they play in the experiment.

To address item A, the various degrees of freedom and the role they play in this experiment will be enumerated.

The support structure is designed to manipulate the flat semiconductor mirror with respect to a fixed curved mirror. Translations along \hat{k} provide for control over the length of the cavity. Cavity length must be controlled precisely as it directly affects the detuning between cavity modes and a dot. Additionally, the large temperature range experienced by parts of the structure when cryogens are introduced means that the ability to translate the mirror over large distances is

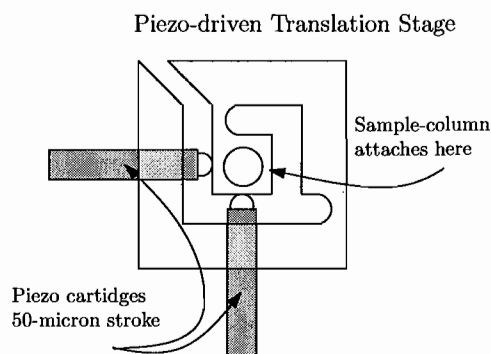


FIGURE 3.12: Flexure mount for X-Y translation. The structure used to allow X-Y translations of the DBR is shown. The optical axis of the transmitted beam passes through the hole at the center of the stage.

required: The position of the flat mirror changes by more than $100\ \mu\text{m}$ as the structure is cooled down from room temperature to about 15 K. Actuation of a tripod provides for translations as well as pitch and yaw. In practice roll (rotations of the flat mirror around the z-axis) turns out to be unnecessary. While it would allow for orientation of the quantum dot dipole moments, it is much easier to simply rotate the polarization of the electric field using waveplates.

By placing the flat mirror in the pivot plane (the plane that includes the support bearings) the tilt becomes decoupled from translation. This comes at the expense of the lateral translation. Lateral translation capability is restored by the inclusion of a simple flexure stage that allows lateral movement of a central flange with respect to the center of the tripod's base. The face of this structure is shown in figure 3.12. The face of the structure attaches to the base of the tripod and contains threaded holes (not shown) that allow the sample column to be bolted to the center portion of the structure.

Because of a lack of position readout on each leg of the tripod we did not actively control for pitch and yaw. The tripod essentially was used as a piston and changes in the pitch and yaw were dealt with by adjusting the trajectory of the input beam.

A series of flanges are mounted to a set of tube components. This provides a modular way of attaching components together. Extending from the bottom of the tripod's base, the following components are bolted together:

1. Tube-shaped piezoelectric transducer
2. Vespel (polyimide) tube for thermal isolation
3. High purity aluminum sample holder
4. Sapphire disk with semiconductor DBR attached

Moving from the end of the list backward, the semiconductor DBR was attached to a sapphire disk oriented with the c-axis normal to the surface to minimize the effects of birefringence. Sapphire was chosen for its combination of transparency and large thermal conductivity at low temperatures. This was attached to a high purity aluminum sample holder with Epo-Tek T7110 thermally conductive epoxy from Epoxy Technologies. Aluminum offers a favorable combination of low density and high conductivity. This aluminum sample holder provides the attachment points for the cold finger. This is discussed in further detail in section 3.6.

A Vespel (polyimide) tube supports a large thermal gradient and allows the tripod, support structure, and piezo element to remain at room temperature while the sample and holder are brought to cryogenic temperatures. This stage is bolted to a tube-shaped piezoelectric transducer. The transducer is a multilayer Lead-zirconate-tantalate (PZT) stack operated at low voltage (0–150V), which is responsible for the controlling the cavity length on small length scales.

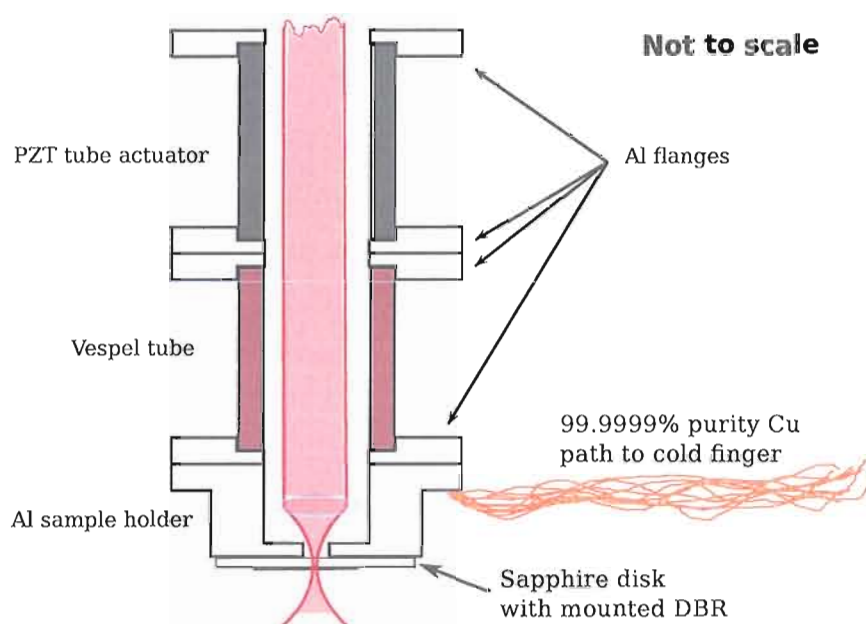


FIGURE 3.13: Schematic of sample column: This shows a schematic representation of the column that contains the sample holder and attaches to the base of the tripod. High-purity copper wires connect the sample holder to the cold finger.

The Invar tripod is supported on a kinematic mount consisting of a set of ruby bearings that contact a cone, a groove and a plane (respectively). This properly constrains the position and orientation of the tripod and allows it to be

manipulated by adjusting the heights of the support bearings. Burleigh Inchworm UHVL motors were chosen to control the tripod positions because of a few factors:

1. They are capable of long travel when compared to other piezo based actuators.
2. They do not require any lubricants to operate properly. Thus, they are well suited to a UHV environment.
3. They can support a modest load even without any drive power. By design, they clamp down when voltage is absent.

The design of this structure was performed on a computer running TurboCAD. The alloy Invar36 was selected for the bulk of the apparatus due to its extremely low coefficient of thermal expansion. Parts were made of Invar36 where possible to avoid bi-metallic junctions and improve the stability of the system during baking.

An isometric drawing of the assembled mechanical support structure is shown in figure 3.5. This includes a set of three Burleigh UHVL Inchworm stages designed for UHV operation. A damping structure consisting of two plates with matching "V"-grooves separated by 0.5" diameter Viton cylinders is visible, near the bottom of the drawing. This structure proved to be instrumental in getting the vibrations of the cavity to a tolerable level.

A photograph taken from the main port of the vacuum chamber is shown in figure 3.17a. The cold-finger and radiation shield are visible to the right of the cavity and support tripod.

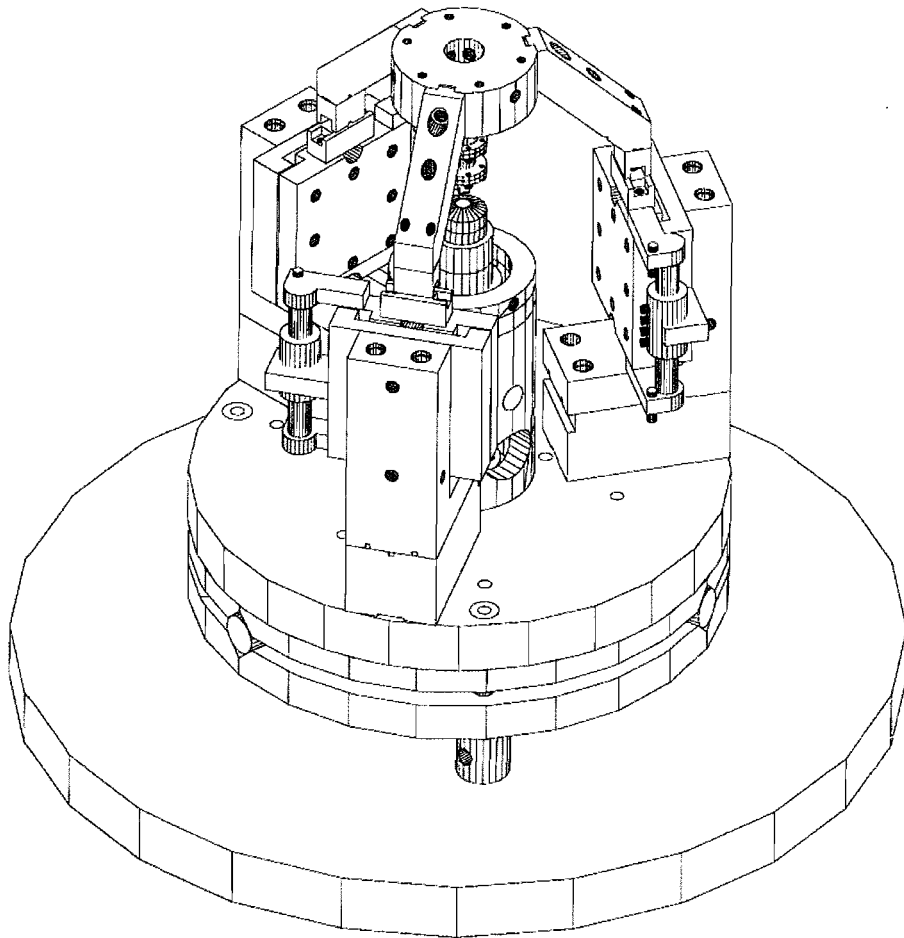


FIGURE 3.14: Hidden-line drawing of the support structure. The figure shows an isometric line drawing of the support structure. The drawing was produced by TurboCAD.

3.6 Cryostat and Cold-Finger

As is mentioned in footnote 1, the existence of the quantum dots as well as the optimization of their individual coherence times depends upon attainment of a suitably low temperature. Heat is pumped out via a cold-finger attached to the aluminum sample holder with a collection of high purity (99.9999% pure) copper wires.

The cold-finger brings the proximity of the cold reservoir a short distance from the DBR.

The temperature is maintained by cold helium pumped out of a helium dewar, through a transfer tube (Oxford LLT) and into an Oxford Ultrastat — a low-vibration, continuous-flow cryostat. Cold helium gas is drawn back through a return pathway in the transfer tube, which helps to keep the helium cold while it is sent to the cryostat. The liquid helium absorbs heat from a heat transfer block at the end of the cryostat. The temperature of the heat transfer block can be controlled by throttling the flow rate of the helium, which provides a coarse level of control, or by using a heater attached to the block. The controller for the system reads a temperature sensor mounted to the transfer block and can drive the heater with a proportional-integral-derivative (PID) circuit to control the temperature to within ± 0.1 K. The temperature at the sample holder is measured by a 4-probe measurement on a diode (Lakeshore DT-470) bolted to the sample holder.

One of the difficulties we faced is that a pathway used for heat conduction can also conduct vibrations into the structure that it cools. In this apparatus, only the DBR is cooled, while the curved micro-mirror and surrounding structures remain at room temperature. The cold finger connects only to the aluminum sample holder, to which the semiconductor DBR is mounted. The length of the optical cavity is, therefore, sensitive to vibrations in the direction of the cavity's optical axis that propagate to the cavity from the cryostat. In order to stabilize the cavity, it was necessary to mount the cryostat with a vertical orientation. This provided for a slightly longer path for the cold finger, but it effectively decoupled the main vibrational modes of the cryostat from changes in the cavity length.

A schematic representation of the cooling system is shown in figure 3.15. Before installation in the UHV chamber, all copper parts were polished and treated with an acetic acid solution to remove any residual oxide or hydroxyl layers [10] in order to improve thermal conductivity at the metallic interfaces.

3.7 Ultra-high Vacuum Chamber

The low temperature of the sample necessitates an UHV environment. Atmospheric components will adsorb onto cold surfaces, spoiling surface quality of the cold mirror. For this reason, cryostats generally operate in high or ultra-high vacuums.

The main chamber is pumped out by a Varian Turbo-V 70 turbopump backed by a Varian SD-90 mechanical pump. This arrangement is capable of bringing the

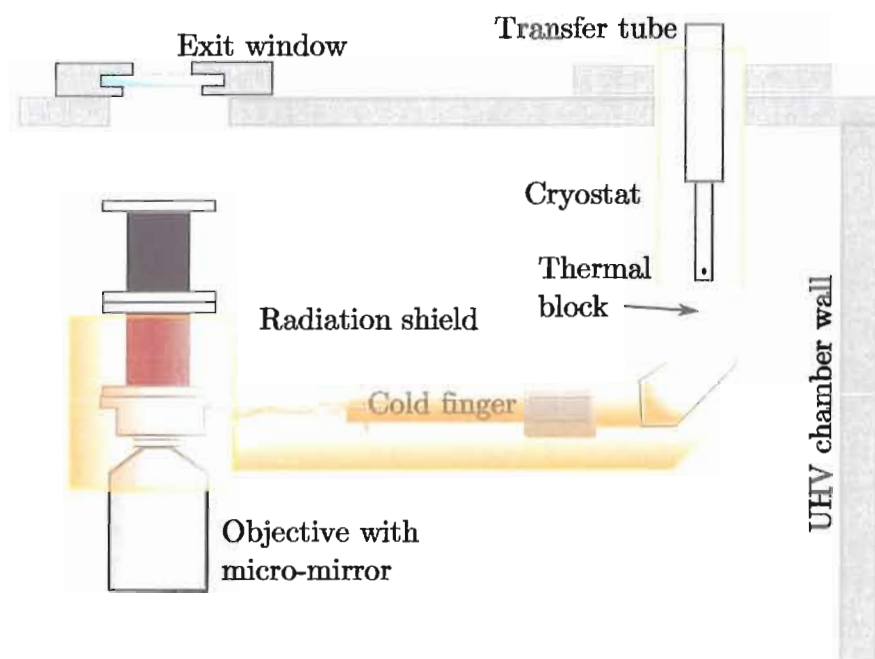


FIGURE 3.15: Schematic of cooling system. The sample column is depicted on the left side above the objective with mounted micro-mirror. The support tripod has been omitted. The walls of the UHV chamber are shown, along with the feedthrough for the cryostat and the attached cold finger. A radiation shield of polished, OFHC copper surrounds the cold finger and the cooled sample holder to reduce heating by blackbody radiation.

chamber pressure down to a pressure of the order of about 10^{-6} Torr. To proceed beyond a high vacuum to an ultra-high vacuum the turbopump and roughing pump are isolated from the chamber with a pneumatic-actuated inline valve. Finally, a gate valve is opened to expose an ion-pump to the main chamber. The base pressure in this configuration is several nTorr.

The layout of the vacuum system is indicated in the following diagram:

3.8 Summary

The apparatus may be roughly considered to be the preceding materials and the associated electronics and control software. We may consider this to constitute the environment in which the experiment takes place. We have identified experimentally important degrees of freedom and addressed how they are to be controlled in the experiments.

The laser sources, and beam-control and detection systems will be described in the next chapter, since the configurations of these are subject to change depending on which measurements need to be made. Except for the use of two different DBRs, the components described in this chapter are not subject to change and may be roughly considered to constitute the apparatus that we seek to manipulate and whose optical properties we wish to measure.

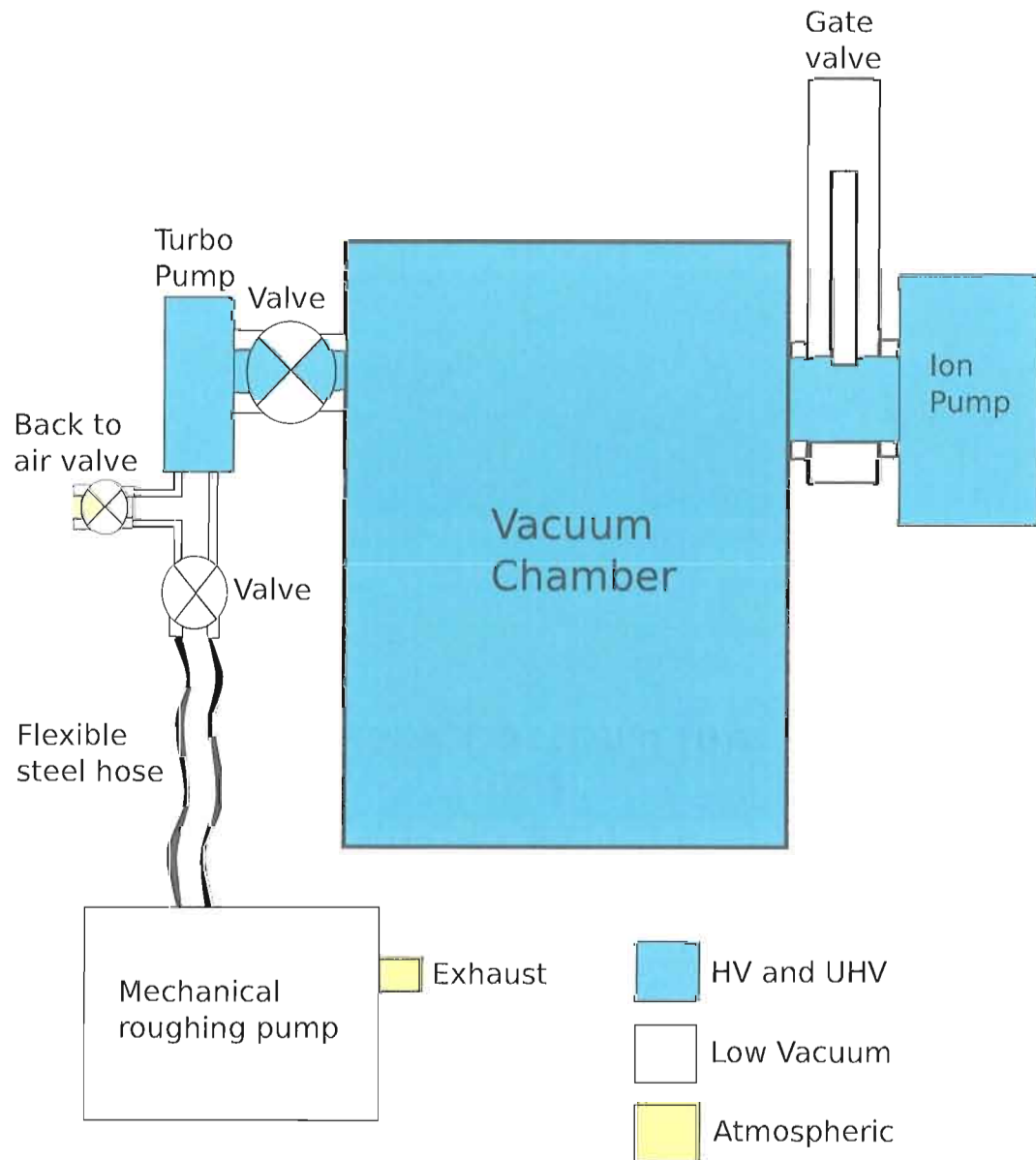
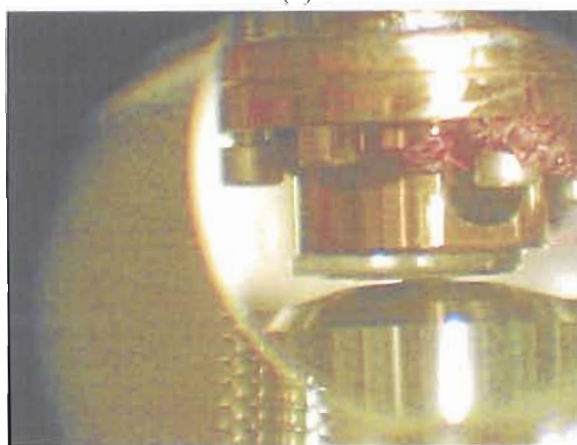


FIGURE 3.16: Schematic: UHV system. This block diagram shows the layout of the ultra-high vacuum system.



(a)



(b)

FIGURE 3.17: Photograph of the support tripod and cooling system taken from the main port of the vacuum chamber (a) and a magnified view (b).

CHAPTER IV

EXPERIMENTS AND DATA

4.1 Introduction

In this section, account will be made of efforts to observe vacuum Rabi splitting in this system. A description of both the input-beam preparation and the collection/detection system will first be provided. Later, we examine some data from each of three lasers used as a probe for the microcavity system.

4.2 Input Beams

Here we briefly describe how the lasers are prepared for entry into the CQED system.

4.2.1 Laser Sources

In order to measure the transmission spectrum for the coupled cavity-QD system, two different diode lasers were used. One of them, a Velocity 6312 tunable diode-laser from New Focus, was capable of emission over a range from 771 – 789 nm and was used as a reference laser to fix the length of the optical cavity. Because it could be tuned to energies lower than either the ground state

excitons of the IFQDs or the continuum of QW states, it can be used without fear of generating excess excitations in the CQED system.

In the initial runs, a tunable diode laser from Newport (a 1040A motor-driven Littman-Metcalf) was used as a probe. It was capable of emission across a range from 748 nm to about 759 nm. Later, a Ti:Al₂O₃ and another diode laser (LiON by Sacher Lasertechnik) were used to investigate the system in the vicinity of the design wavelength of the spacer-layer. The Ti:Al₂O₃ laser was determined to have an inhomogeneous linewidth in excess of 2 GHz as measured with an optical spectrum analyzer (a scanning Fabry-Perot). Because the output of this laser was found to be spectrally broad due to the presence of multiple modes, data from these scans will not be included here. These scans did not yield any useful data.

In an effort to provide clean mode matching from free-space modes into micro-cavity modes, both lasers (probe and reference) were coupled through a length of polarization-maintaining single-mode fiber (SMF). The output from the fiber should correspond closely to a single Gaussian mode.

By preparing both probe and reference beams with orthogonal polarizations they can be efficiently combined onto a common path with a polarizing beam splitter (PBS). Both beams are then launched into a polarization-maintaining SMF. This maintains the purity of the polarizations (along with relative orientations) and provides a common optical axis for each beam as each one couples to a free-space mode at the other end of the fiber.

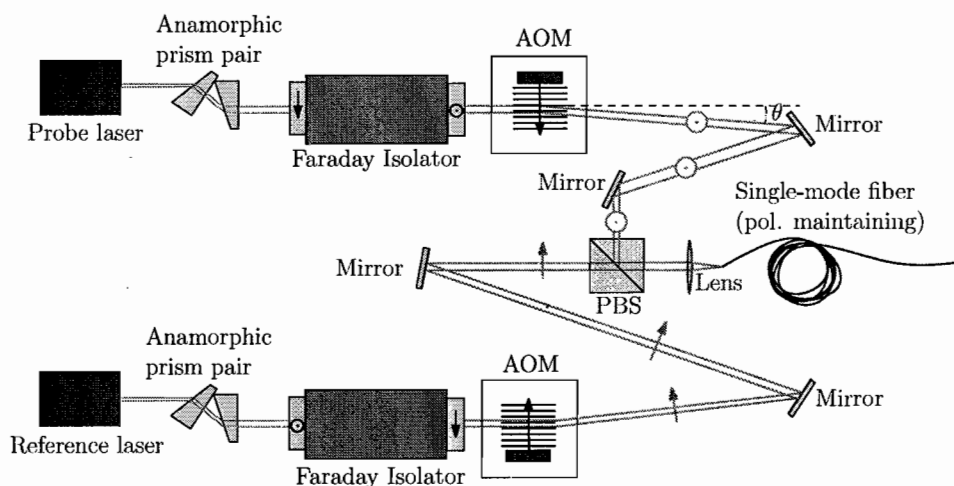


FIGURE 4.1: Laser sources filtered by single-mode fiber. Probe and reference lasers are prepared with orthogonal polarizations and combined on a PBS. Both beams then enter a single-mode fiber.

Because both the reference laser and the probe laser are diode lasers whose beams emerge with large aspect ratios, anamorphic prism-pairs are used, as indicated in figure 4.1, to correct beam shape and improve coupling into the optical fiber. Each beam is passed through a Faraday isolator to prevent retro-reflected light from entering the laser cavity. An acousto-optic modulator (AOM) is inserted into each beam to allow for lock-in detection at the output. The probe AOM operates at 80 MHz, the reference AOM at 100 MHz.

Examining the beams that emerge from the SMF, we verify that the beams have smooth Gaussian spatial distributions and well-defined, linear polarization. The probe beam is polarized vertically (V), with respect to the table and the reference beam is polarized horizontally.

These beams are both roughly collimated. Because a microscope objective is used to collect the output from the SMF, the focal length for the two beams is slightly different due to dispersion and different indices of refraction for the two beams.

A periscope brings the combined beam to the correct height and a pair of steering mirrors is used to send it through an optical window in the side of the UHV chamber. From here it strikes a mirror at 45° and propagates vertically, approximately along the cavity optical axis defined by the orientation of the flat mirror. The beam now enters the Zeiss Plan-Neofluar immersion objective with integrated micro-mirror.

4.3 Output Beams

The emission from the cavity in the forward direction is collected by an aspheric collection lens. Aligning the collection lens is a delicate matter because it must be aligned while the mirror separation is small enough for a stable resonator to exist so that there are modes to collimate.

The collimated modes exit the UHV chamber through an anti-reflection-coated window. The cavity emission, which contains both probe and reference beams, is steered through a pair of irises that defines the optical axis of the collection system. The probe and reference beams are then separated in one of two ways, depending on whether active stabilization is required or not.

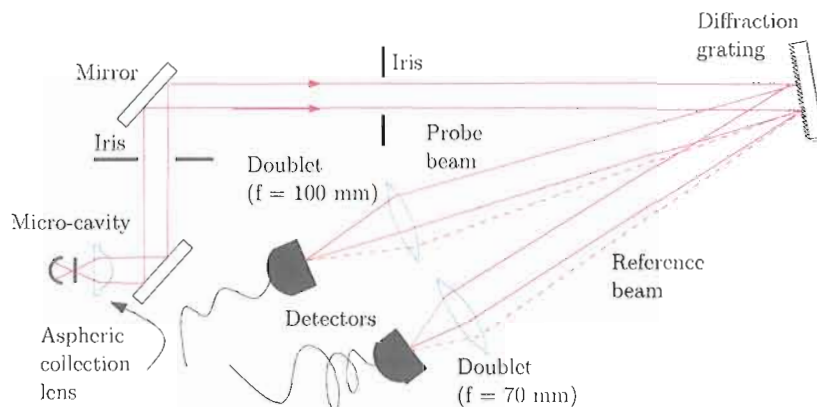


FIGURE 4.2: Detection setup for active control of cavity length. The emitted light is collected by an aspheric lens and steered through a pair of irises. The probe and reference beams are separated by reflection from a diffraction grating (with 1800 lines/mm). Doublets are used to image the grating to photo-detectors located in each first-order diffracted beam. The solid lines indicate the short wavelength end of the respective tuning ranges. The dashed line indicates the long wavelength end. The doublets image the surface of the grating to the detectors, regardless of which wavelength of light is used for the reference or probe.

4.3.1 Active Configuration

If active stabilization is used then a grating must be used to separate the two beams based on wavelength. A blazed grating separates the two beams and each one is sent to a separate detector.

Doublet lenses are used in each first-order diffracted beam to image the surface of the diffraction grating to the surface of a photo-detector. These doublets have sufficient numerical aperture to accept angular variations in the diffracted beams due to changes of the laser wavelengths.

In this configuration, we implement a form of the Pound-Drever-Hall method of laser stabilization [3]. The version of this method used here involves slow dithering

(at 5 kHz) of the laser frequency around the target wavelength. The frequency modulation is produced by dithering the laser frequency by several GHz via a sinusoidal signal applied to the piezo element attached to the laser cavity's end-mirror.

An error curve is produced by mixing the cavity transmission signal with the sinusoidal signal used to drive the piezo. This is done using a lock-in amplifier.

By applying appropriate gain and phase shifts to the error curve, a control signal is produced and fed to the piezo actuator that controls cavity length. A circuit was built up using a board designed by Dan Steck (University of Oregon) for the purpose of driving laser diodes. This circuit contains proportional and integral response stages and permits stabilization against thermal drift and low-frequency noise over long time scales.

4.3.2 Passive Configuration

There is a loss of efficiency from collecting the light from a single diffraction order. (Typically, one can expect to get at most half of the energy in the first diffracted order.) If active stabilization is not needed, then efficiency can be improved by using a PBS to separate the two polarization components. In this configuration, there is too much cross-talk to run both beams simultaneously. The reference laser is used to set the cavity length at the beginning of a scan and then it is blocked while the scan is carried out.

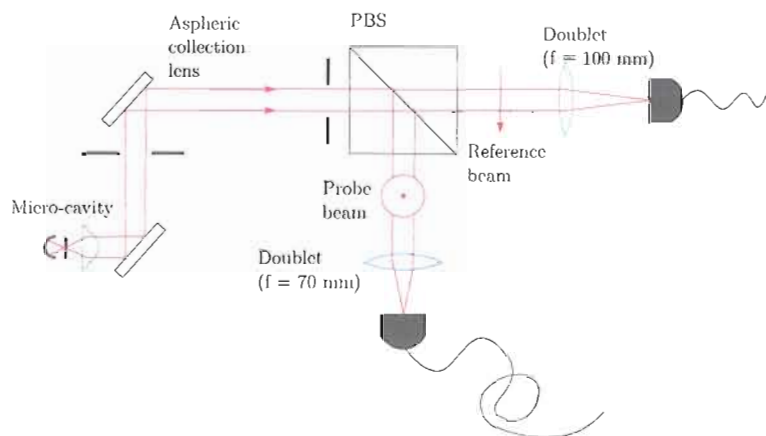


FIGURE 4.3: Detection configuration for passive cavity control. A PBS separates the transmitted light into two orthogonal polarization components. This gives more detail about the polarization properties of the mode, but does not permit the reference beam to occupy the cavity while data is being collected.

Once vibration issues had been properly dealt with by inclusion of Viton supports, the cavity was found to be stable enough on the time scale of a scan, so this configuration was used to collect all data after July 2, 2007.

4.4 Mode Matching

From experience with paraxial modes it is expected that higher order modes will distribute the energy across a larger radial distance and provide a larger effective spot size and consequently, a larger effective volume. Numerically, modes with higher total angular momentum (necessarily higher order modes) have turned out to have smaller field strength than the on-axis strength of the VTM_0^1 mode. In accordance with the findings in section 2.6, the mode exhibiting a small spot and non-Gaussian angular spectrum should give the best coupling strength.

At the hemispherical limit, the modes sort themselves into two groups, according to two-dimensional parity inversion symmetry, each separated from the next by half of the free spectral range. In order to be able to probe one mode alone, even when the cavity length is such that two or more modes align at the same frequency, it is important to be able to exercise some control over the mode matching from free-space traveling modes into modes of the micro-cavity.

Angular misalignment of the input beam will tend to put energy into odd modes. Consider that the phase front of the input beam will exhibit a gradient when compared with the equipotential imposed by the surface of the mirror. I.e. the phase at the equipotential surface will have an advanced lobe and a retarded lobe.

Translational misalignments of the input beam with respect to the cavity optical axis will tend to drive combinations of the lowest order odd-modes along with the fundamental.

To lowest order, driving the odd modes can be eliminated by placing the input beam onto the correct trajectory; centered properly and angularly aligned to be collinear with the cavity optical axis. This can be accomplished with a pair of steering mirrors.

Not including the fundamental, which simply has a constant phase across a certain region of the input mirror, the lowest order even modes correspond to errors in the Rayleigh range of the input beam. The input beam should be the correct

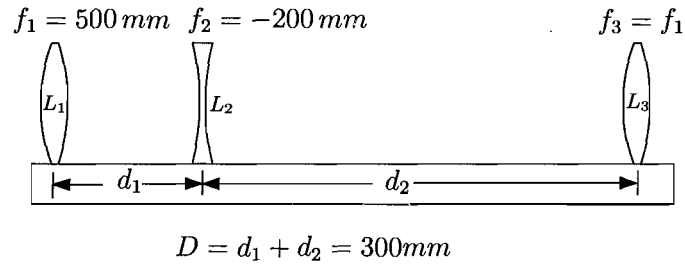


FIGURE 4.4: Lens system schematic. The total distance between L1 and L3 may remain fixed. Different configurations may be achieved by modifying, for example, d_1 .

Gaussian to match the curvatures at the two mirror surfaces that form the cavity, thus it should have a Rayleigh range that matches the cavity.

Running some calculations of ray transfer matrices led us to a configuration of lenses that allowed a range of modification of curvature without substantially altering the diameter of the beam at the location of the cavity. The arrangement of lenses is shown in figure 4.4.

The effect of the lens system is shown for three different configurations in figure 4.5. Figure 4.5d shows the reduction of the transmission spectrum to a single mode output. Conveniently, the reference laser also experiences effectively single-mode throughput in an overlapping range of configurations (i.e. we see single-mode throughput for $d_1 = 90 \text{ mm}$).

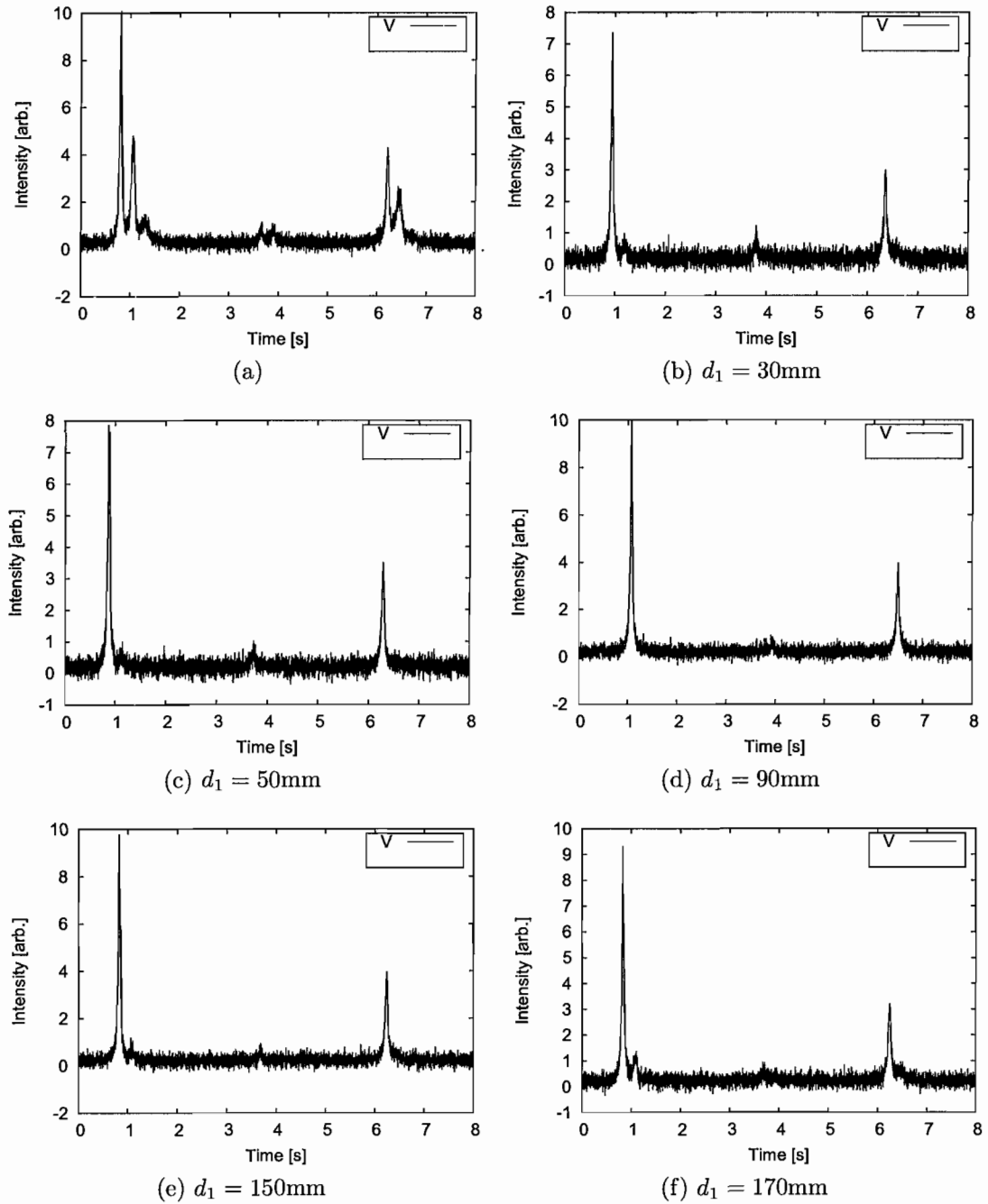


FIGURE 4.5: Effect of the lens system. The effect of the lens system on the Newport laser is shown for 5 different configurations. For reference, (a) shows the transmission spectrum without lenses. All scans cover a range of 750 – 758 nm of wavelength. For a fairly broad range of values of d_1 around 90 mm the throughput is effectively single-mode (i.e. the higher modes do not rise above the noise floor).

4.5 Cavity-Modified Photoluminescence

In order to check the population and distribution of dots on the sample, we measured the cavity-modified PL. We pumped the dots with a red diode laser at 658 nm coupled through the SMF shown in figure 4.1. The pump laser was inserted into the probe arm with a collimating lens and an anamorphic prism pair to improve coupling into the SMF. The SMF is not single-mode for the pump wavelength. Nonetheless, it provides good collinearity of the pump with the reference laser path.

The cavity mirrors are not high reflectors at the wavelength of the pump. The free pump beam emerges from the other side of the cavity and is separated from the PL light by a colored-glass filter that transmits light longer than CHECK THIS 700 nmCHECK THIS. This allows the PL to pass unimpeded, while absorbing the transmitted pump light.

In order to analyze the polarization properties of the PL, a polarizer was placed in the path of the beam; just before the fiber in figure 4.6. The peak signal was recorded for a set of polarizer angles to determine the orientation corresponding to maximum oscillator strength. This provides an in situ method of verifying the orientation of the dipole moment for the IFQDs. The result of this investigation is shown in figure 4.9.

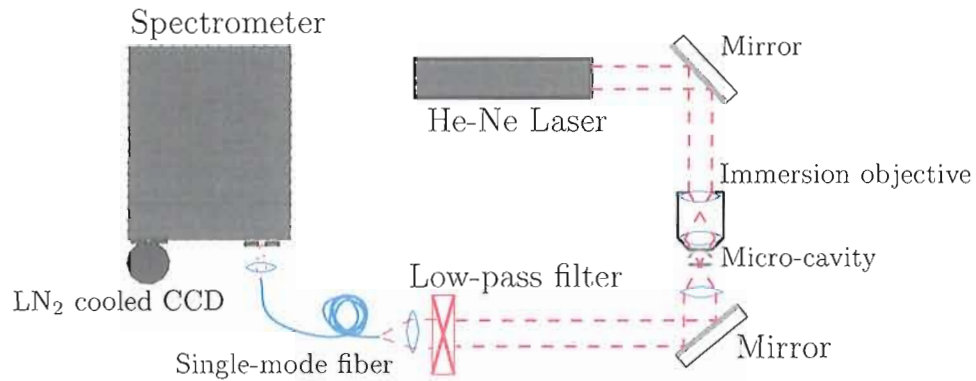


FIGURE 4.6: Cavity-modified PL — setup. This figure shows the setup for measuring cavity-modified PL. A red diode laser pumps the QDs, producing luminescence. Resonant luminescence will be collected into cavity modes and transmit through both cavity mirrors. PL is collected from the side of the cavity bounded by the semiconductor DBR. After transmission through a low-pass filter that screens out the pump light, the PL is coupled through a single-mode fiber and sent to a spectrometer where the frequency components of the PL are resolved and integrated on a liquid-nitrogen-cooled CCD.

The signals are peaked around a vertical polarization (90°). This verifies that the primary dipole moment of the IFQDs points in a direction corresponding to vertical polarization of the input beam.

4.6 Using the Newport Laser as Probe

Under the original scheme, the New Focus laser acts as a reference and the Newport laser is tuned between 748 nm and 760 nm to look for vacuum Rabi-splitting.

Figure 4.10 shows the complete absorption of a mode near the hemispherical limit under a small change in the cavity length. This indicates that the absorption

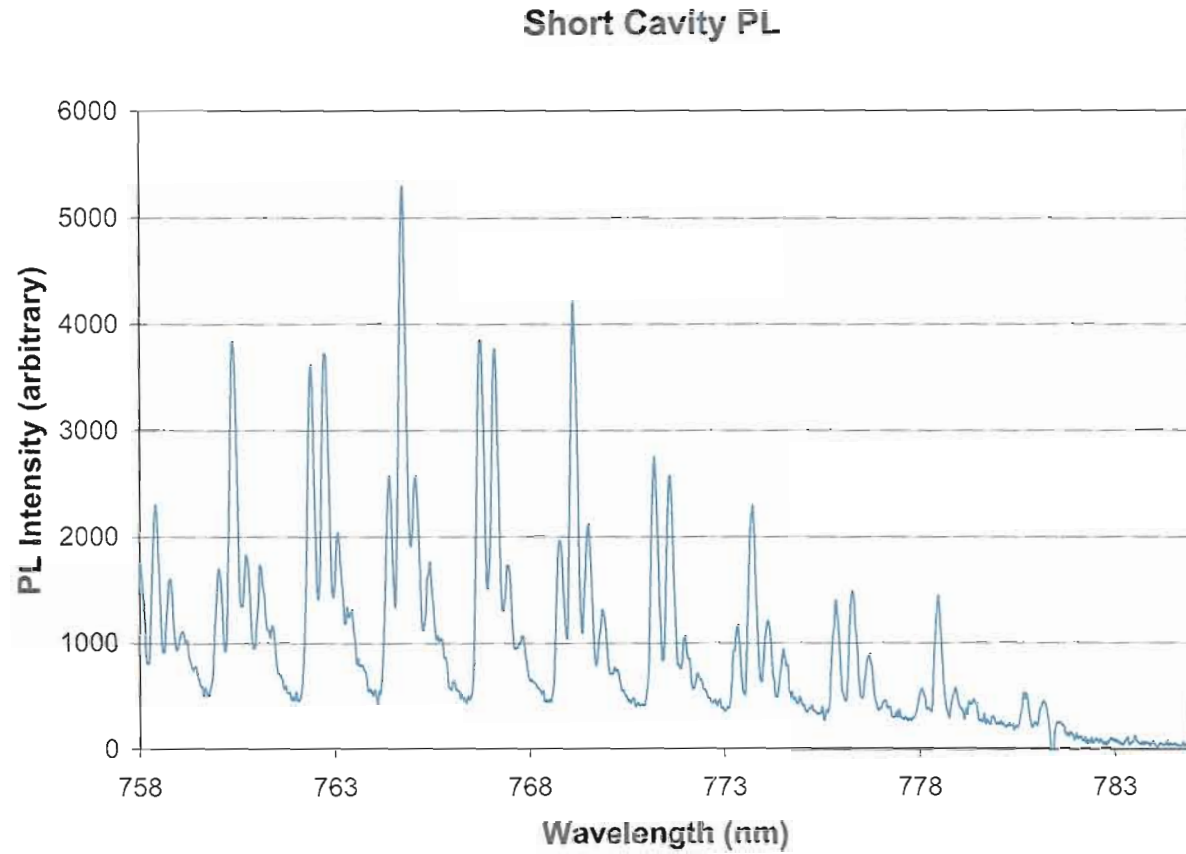


FIGURE 4.7: Cavity-modified PL — short cavity. This plot shows PL emitted by intracavity IFQDs. The cavity has been shortened so that the transverse mode spacing is larger than the linewidth of the spectrometer. The QDs are pumped with a red diode laser at 658 nm. The pump power is 318 μW .

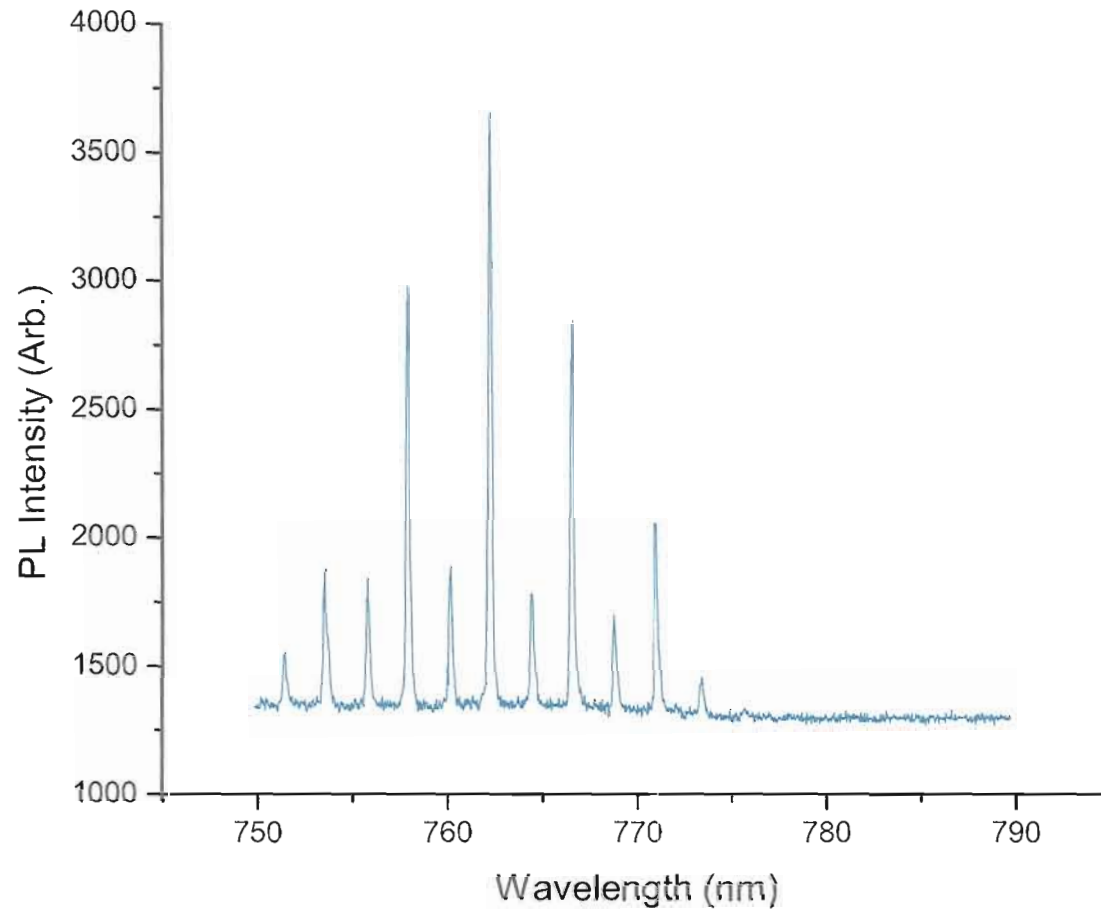


FIGURE 4.8: Cavity-modified PL — long cavity. Compared with figure 4.7, the spectrum here is much simpler. All emission comes out in peaks spaced by half of the cavity FSR.

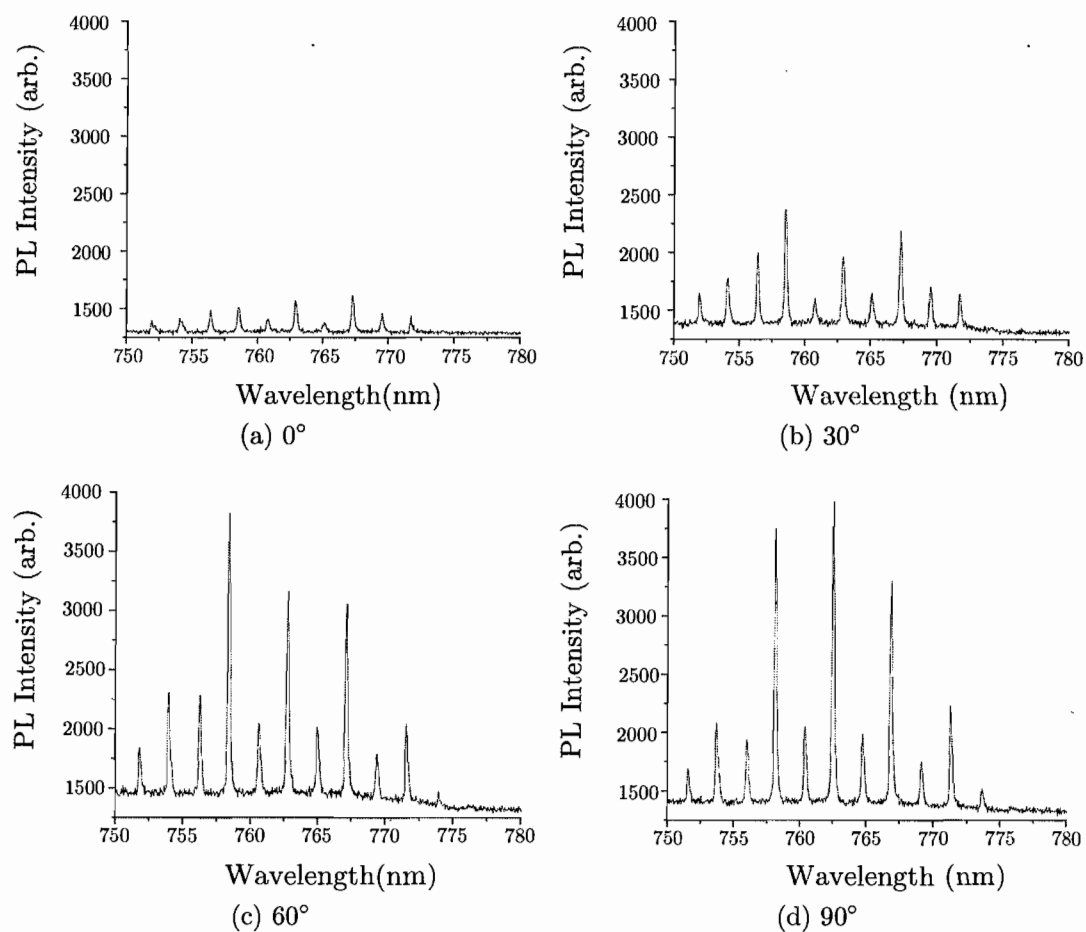


FIGURE 4.9: Polarized PL from intracavity IFQDs. This sequence of PL spectra shows the effect of rotating a polarizer introduced into the beam measured by the spectrometer in figure 4.6. The polarizer angle is measured with respect to the table horizontal.

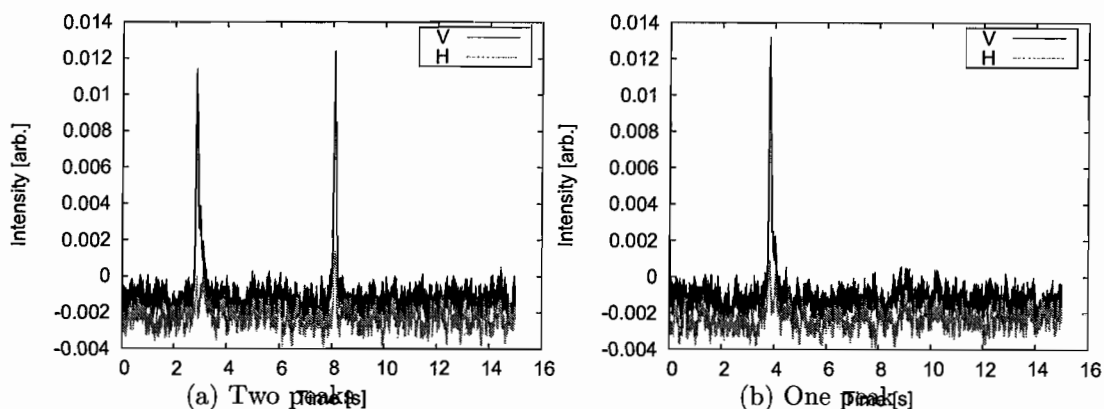


FIGURE 4.10: A missing peak. Two scans at the same location on the sample but different cavity lengths. Both scans cover a wavelength range of 748 – 763 nm at 450 nW. The longer wavelength peak in (b) has been completely absorbed.

spectrum is non-uniform and it should be possible to locate regions in which only one IFQD interacts with the mode.

The cavity in figure 4.10 has $L \approx R$. We have also seen narrow absorption features interact with groups of modes in a slightly shorter cavity. In certain places, where narrow absorption features overlap with modes of a shorter cavity, we can see similar behavior in more detail.

Figure 4.11 shows the presence of a narrow absorption feature as revealed by scanning a group of modes through the spectral region containing the absorption via incremental changes in the cavity length. In this set of scans we can see the gradual absorption of the fundamental and a gradual increase in the intensity of the neighboring higher-order mode. While situations like this were encountered on a few occasions, we were never able to observe any splitting of the fundamental.

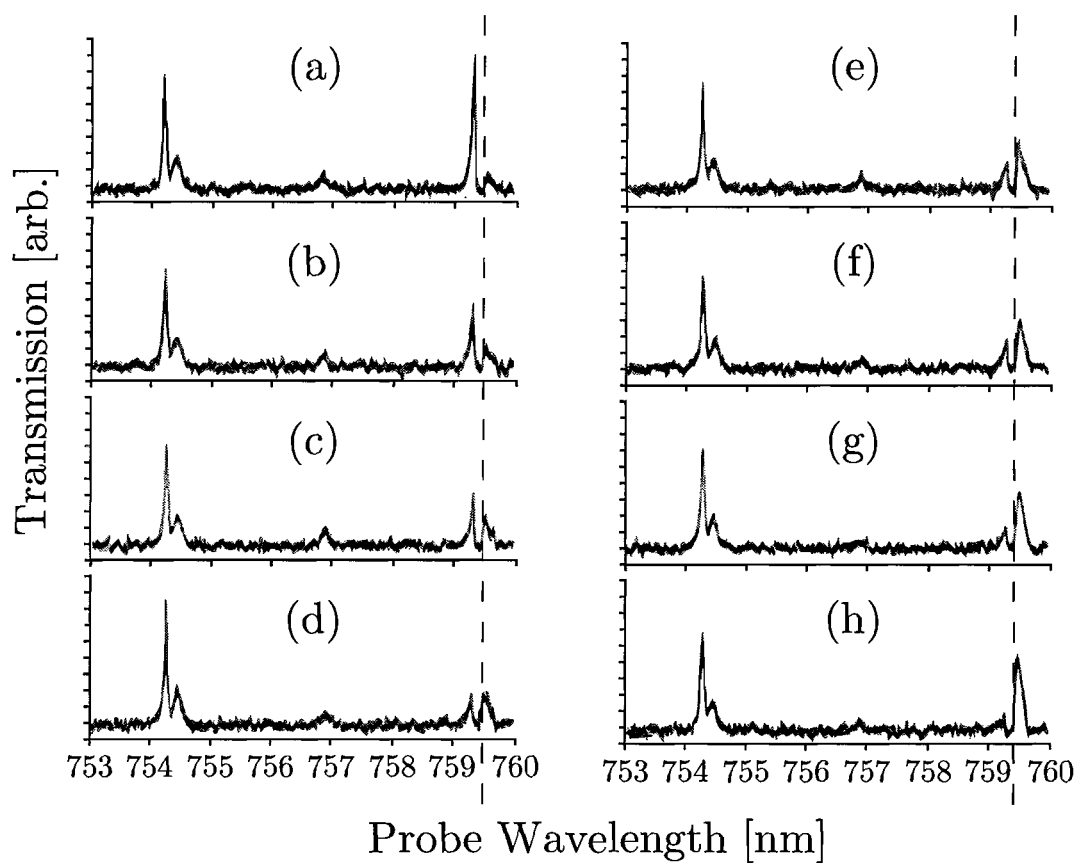


FIGURE 4.11: Narrow absorption tuned through modes. A set of scans with incremental increase of cavity length is shown in (a) – (h). The dashed lines indicate the spectral location of the absorption feature.

4.7 Using the New Focus Laser as Probe

The spectrum of micro-PL from the IFQDs (figure 3.4) shows a long, inhomogeneously broadened tail out to about 775 nm. This indicates a small population of dots with longer lengths, suggesting a better possibility for finding spectrally isolated dots, compared to probing near the maximum of the inhomogeneously broadened PL signal. Additionally, the lower density of dots in this spectral range is expected to improve dissipation induced dephasing rates. The idea is that lower abundance of neighboring dots at or below the energy of a given, excited dot should lead to reduced non-radiative transition rates from a Fermi's Golden Rule type of argument. However, moving to longer wavelengths also reduces the coupling strength between the cavity mode and the dots due to movement of the antinode out of the plane of the QW.

4.7.1 Splittings in Transverse Modes

Some of the data collected using the longer wavelength **New Focus** laser exhibited splittings in the higher-order transverse modes. These modes are already known to be non-degenerate, so this is not intrinsically new behavior. However, there are still some interesting features in this batch of data.

There appears to be a splitting of the higher-order transverse modes that is not easily seen with the other probe lasers. This splitting does not appear to have

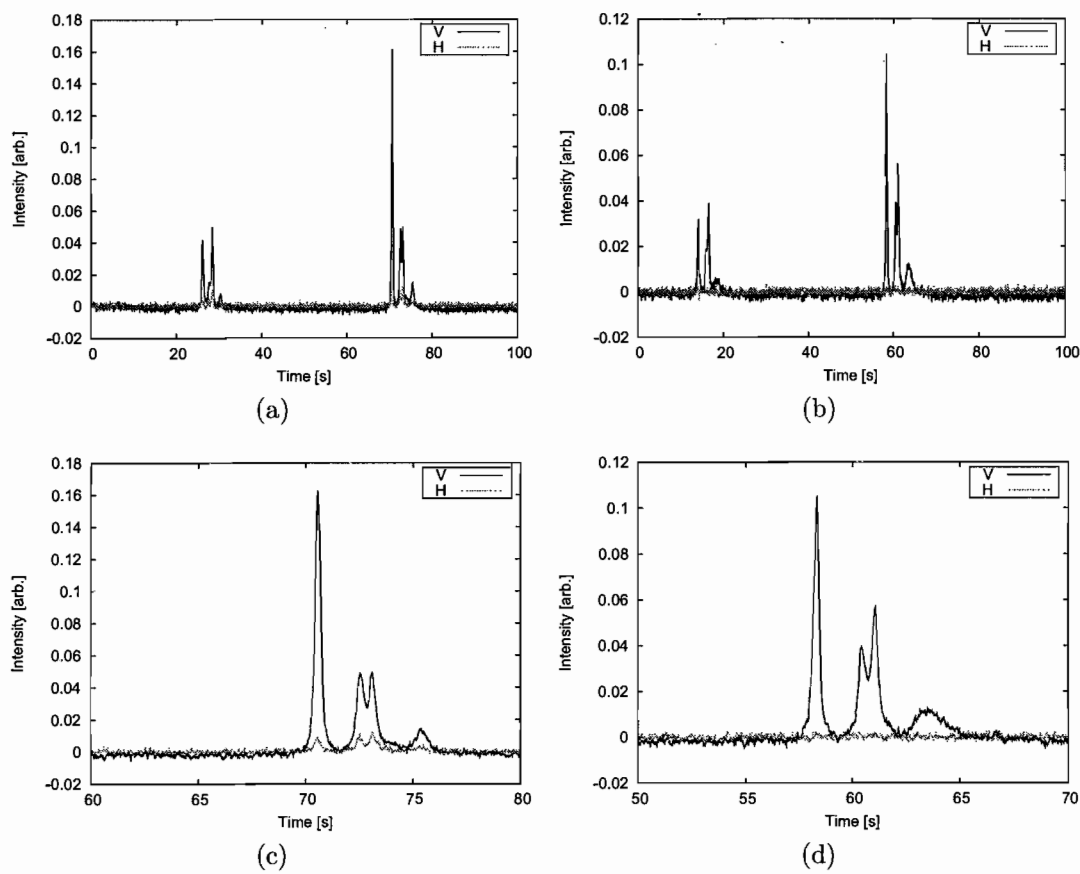


FIGURE 4.12: Doublets except on the fundamental. Long range scans are shown in (a) and (b). The doublets are clearly evident on the N=2 modes in (c) and (d), which show portions of the same scans in finer detail. The laser scan rate is 1 Å/s.

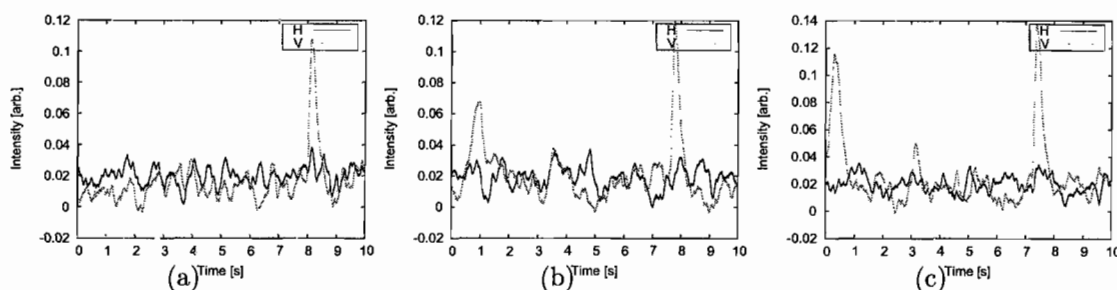


FIGURE 4.13: Sacher single peaks. Data from the early part of the run on November 17, 2008.

anything to do with interactions with QDs due to its appearance at many different locations and cavity lengths.

4.8 Sacher LiON as Probe

The Sacher laser lases over more than 10 nm of wavelength, centered at 765 nm. It appeared to offer the best chance to see strong coupling in this experiment.

Initial scans with the Sacher diode laser exhibited single peaks, reminiscent of a lot of data taken with the other lasers.

Data from the end of the run started to exhibit interesting features.

Beyond this date, all wavelength scans exhibited double peaks on every mode order. Representative scans are shown in figure 4.8

In order to ensure that the laser was lasing in a single longitudinal mode, an optical spectrum analyzer was used to measure the spectrum of the Sacher laser.

The spectrum didn't show any evidence of multiple frequency components and this

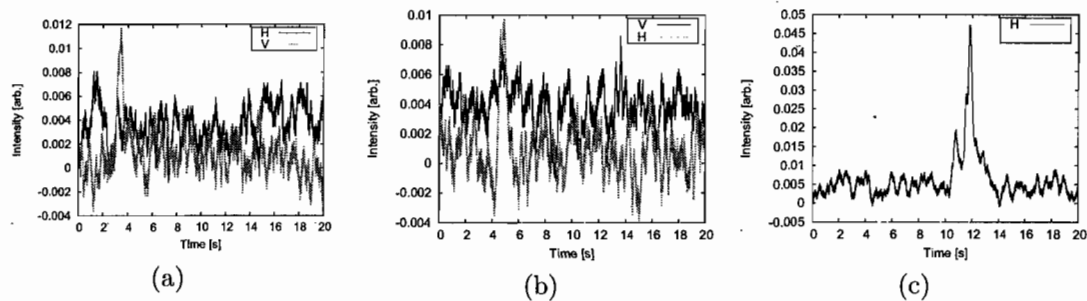


FIGURE 4.14: Sacher strange features. The data began to exhibit some non-Lorentzian lineshapes.

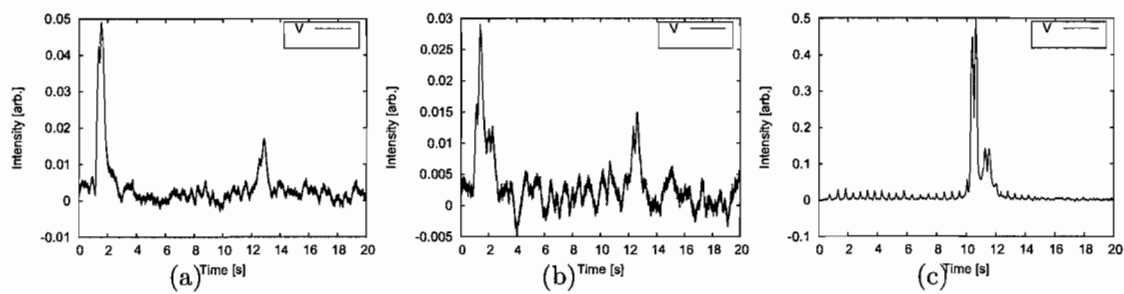


FIGURE 4.15: Sacher — double peaks. Now the data shows double peaks persistently, across multiple transverse orders.

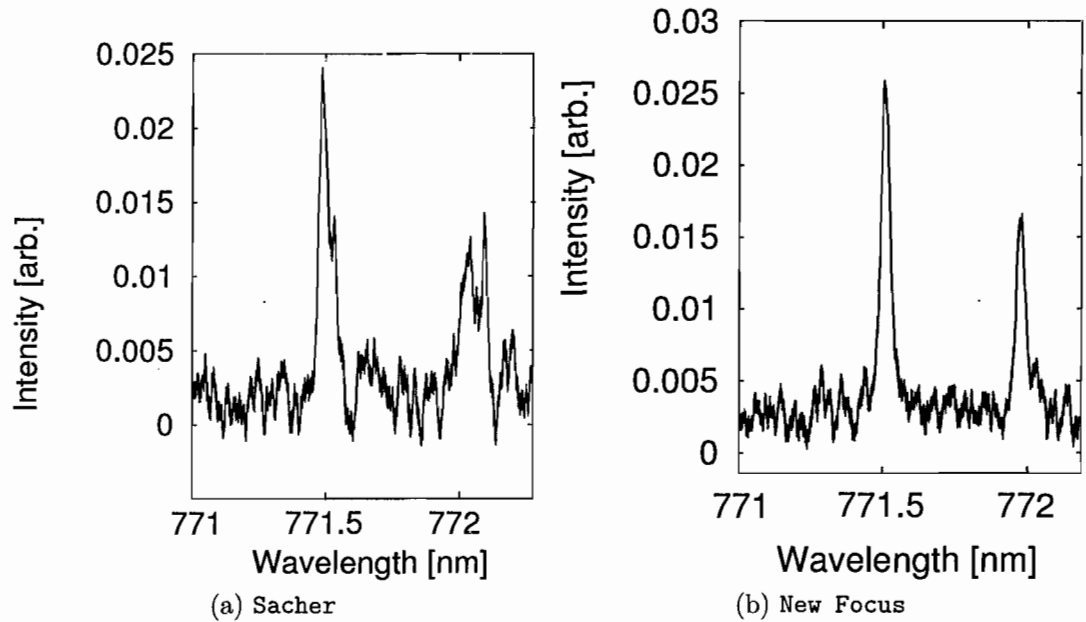


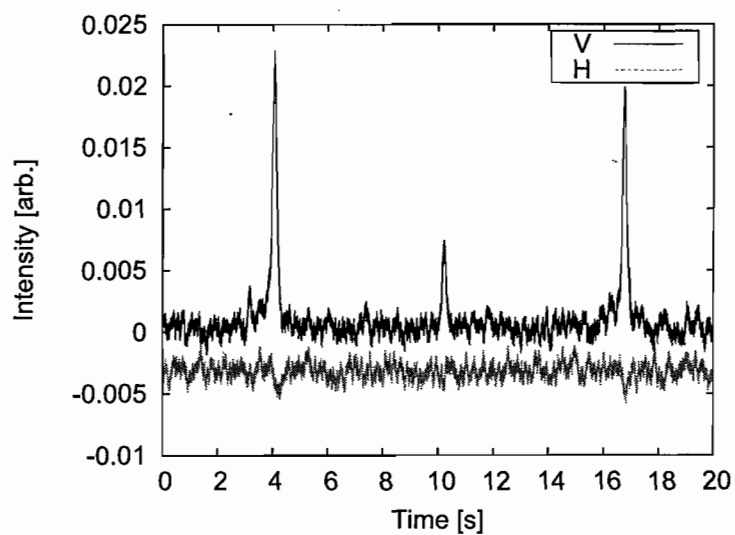
FIGURE 4.16: Sacher vs. New Focus spectra. The two scans overlap and are carried out at the same cavity length and transverse location on the DBR.

led to a temporary suspicion that the double peaks were associated with some kind of cavity effect.

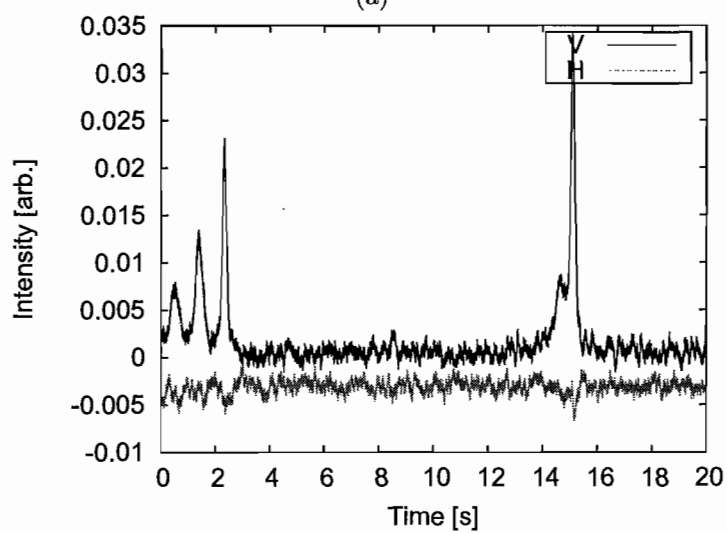
Comparison of overlapping portions of scans carried out with the New Focus laser as probe and the Sacher laser as probe demonstrated that the persistent doublets were due to the Sacher laser, not a property of the CQED system.

4.8.1 Length Scans

The final attempt to observe vacuum Rabi splitting employed the Sacher laser as a fixed-wavelength probe. Rather than scanning the probe energy, transmission as a function of varying cavity-QD detuning was measured. This did, indeed produce single, Lorentzian-like peaks.



(a)



(b)

FIGURE 4.17: Length scans with Sacher laser at 765 nm. Two scans are shown: with the mode-matching optics inserted (a) and without (b).

Figure 4.17 shows scans at the same probe wavelength with and without the mode-matching optics. The peaks show no evidence of the doublets evident when tuning the probe wavelength.

Some scans did show doublets even for the fixed probe wavelength under certain conditions.

Unfortunately, as shown in figure 4.18, these doublets appear to be associated with certain unstable wavelengths of the probe laser. Tuning the wavelength slightly causes the doublets to disappear, while large translations across the surface do not have an effect.

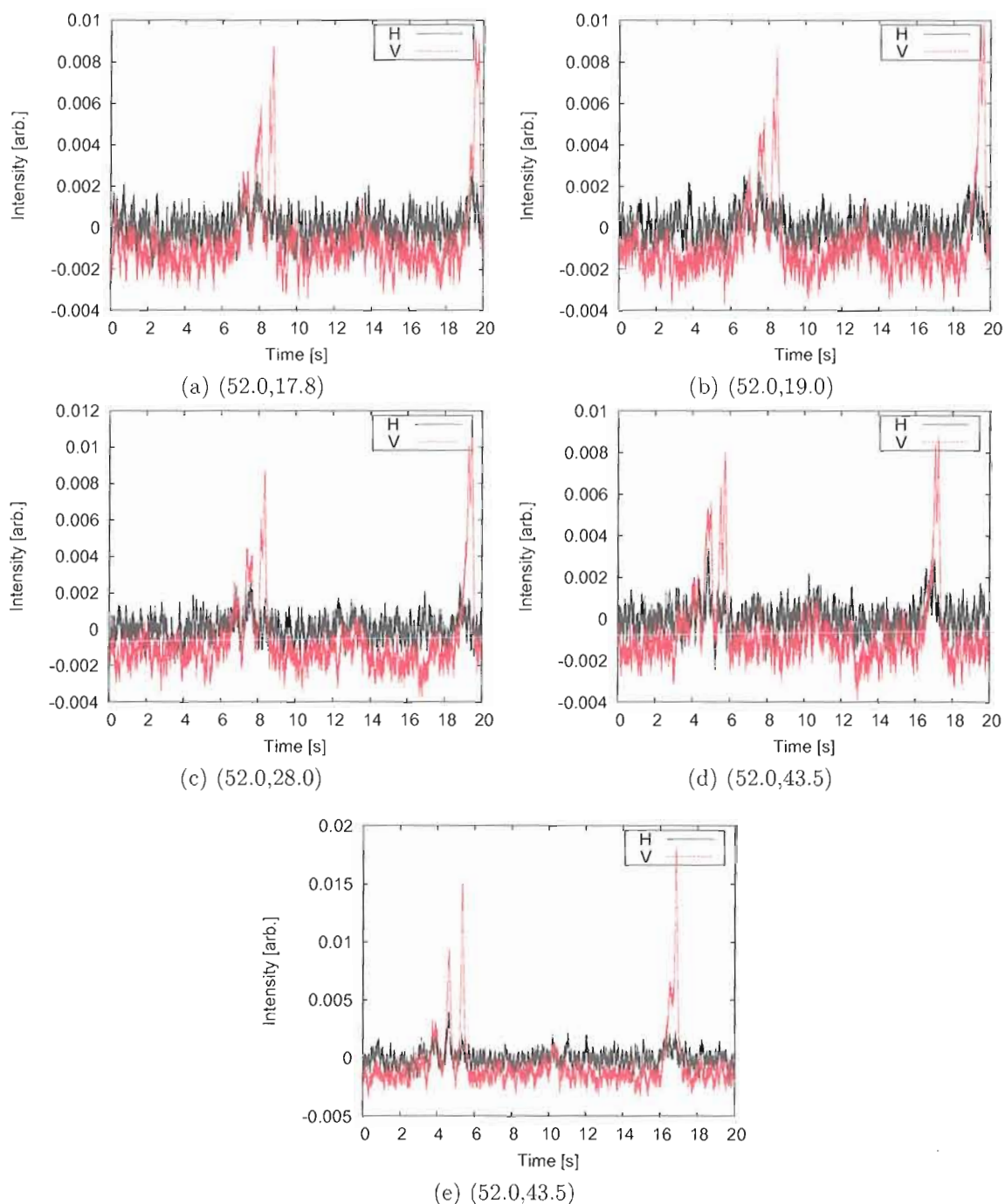


FIGURE 4.18: Length scans for fixed probe at various locations on the sample. The probe wavelength is fixed at $\lambda = 765.17$ nm. The coordinates that label each subfigure indicate the voltage applied to the X-Y piezos. Each volt corresponds to roughly 300 nm of translation. Doublets are evident in each of (a), (b), (c) and (d); each of them separated by at least several IFQD lengths. The final scan (e) is taken at the same location as (d) but for a probe wavelength of $\lambda = 765.19$ nm.

CHAPTER V

CONCLUSIONS AND OUTLOOK

In this chapter we seek to identify the accomplishments made in pursuit of our goals and to try to take stock of the difficulties that prevented the ultimate goals from being realized. We will also point out improvements to the apparatus that may help others wishing to pursue studies with a similar apparatus.

5.1 Conclusions

We successfully designed and fabricated micro-mirrors exhibiting high reflectivity over a large solid angle. The bubbles used to form the substrates for these mirrors range in size from 30 μm up to around 200 μm in radius. The highly curved mirrors offer high reflectivity over a large solid angle. We achieved mirrors with a half-angle of 60° . The mirror coatings were measured to have $R \geq 99.5\%$ out to about a 40° half angle. These micro-mirrors can readily be paired with a wide array of other mirror geometries. When paired with planar mirrors they can readily support non-paraxial modes. The mirror substrates can be ground to retain an arbitrary portion of a sphere, though at this time it's not known what the limits are for currently available coating techniques. Techniques like atomic layer epitaxy (ALE) offer highly conformal coatings, but tend to have lower surface quality that exhibits

higher scattering losses than conventional coating techniques. In any case, the solid angle supported here already provides for attractive confinement of the transverse field and could be used with a planar dielectric mirror to investigate predictions of non-paraxial mode properties such as described in [19, 18].

We also assembled a 5-axis support structure, capable of translation in 3 dimensions as well as pitch and yaw control. As described in chapter 3, roll is experimentally unimportant due to freedom (and ease) of controlling the polarization axis of the incident field.

We attached one side of the cavity to a cold-finger using high-purity copper wires. With high-purity copper components and an OFHC-copper radiation shield, we succeeded in cooling the sample to 15 – 17 K.

We were able to cut down the vibrations in the cavity to be on the order of an angstrom on short time scales, as evidenced by the amount of noise on the peaks in transmission scans. The linewidth of the mode in terms of cavity length depends on the probe wavelength. For a probe at 765 nm, the FSR in terms of cavity length is $\Delta L \approx 383$ nm. The linewidth is then $\delta L = \Delta L / \mathcal{F} = \frac{383 \text{ nm}}{200} = 1.9$ nm. Noise at the top of the transmission peaks is small compared to the peak height, indicating small fluctuations in cavity length during the time scale for the laser to cross a given peak. The Lorentzian appearance of the transmission peaks indicates that the amount of noise introduced by fluctuations of cavity length are small, at least on the time scale it takes for the probe to traverse the resonance. For fluctuations

in cavity length of $\delta x = 0.15 \times \delta L = 0.3$ nm we would expect to see fluctuations of about 2.2% in the amplitude at the peak of the resonance (assuming a Lorentzian lineshape).

We were also able to collect PL from the IFQDs in situ. Analyzing the polarization of the PL allowed us to verify the axis corresponding to maximum oscillator strength and align the polarization of the probe along this axis.

Scans made with the **Newport** acting as probe generally showed broader linewidth, consistent with coupling to more absorbers. At longer cavity lengths we could occasionally see places with selective absorption of a single mode, as in figure 4.10, or increases in the transmission of certain modes in the vicinity of an absorber, as in figure 4.11. This indicates that the spatial resolution is high enough to observe highly non-uniform absorption features. However, no indication of a splitting was ever observed for the fundamental.

The **New Focus** laser exhibits superior tuning stability but worse passive stability (e.g. against thermal drift) compared with the **Newport** laser, which was selected to be used as a probe laser. A more ideal scenario would have allowed the **Newport** laser to act as the reference laser and the **New Focus** to provide mode-hop-free tuning. However, availability of laser diodes for the respective lasers made our chosen configuration the only possibility.

Using the **New Focus** laser as a probe did reveal some interesting features, such as a splitting in the higher-order modes. Again, as for the **Newport** laser, we

never saw any evidence of a splitting for the fundamental. The persistence of the splittings in the higher-order modes across many cavity lengths and positions on the sample suggest that these effects have something to do with the mode structure of the resonator than with an interaction with QDs. In general, the scans using this laser as probe exhibited lower absorption but also fewer features like selective absorption of individual modes.

The initial data taken with the Sacher laser showed single peaks. Subsequent data indicated that the split peaks have to do with scanning behavior of the Sacher laser. This is further suggested by the ability to see single peaks for scans of cavity length with a fixed probe wavelength. Unfortunately, the confirmation that the laser scans were unreliable came after a lot of time spent ruling out other explanations.

A set of cavity-length scans was collected for various positions on the sample and various wavelengths close to 765 nm. This did uncover doublets, but they turned out not to depend on the position on the sample. The immediate disappearance of the split peaks upon a small change in the probe wavelength indicates that this too was due to an artifact of the probe output. It is certainly possible that something could have been uncovered with further, extensive length-scans after careful characterization of which wavelengths produce the doublet behavior. A better alternative, requiring both time and money would be to get the laser repaired. Unfortunately, due to time constraints, by the time the doublets had been

definitively traced to the Sacher laser there was not enough time to return it for repair.

Given the magnitude of the electric dipole moment, approximate mode volume and cavity and QD dephasing rates, we have a system that should be capable of strong coupling. Of course, the potential to observe signatures of strong coupling was not realized in this work and some attention should be given to possible reasons for this.

It should be acknowledged that there is quite a large parameter space to search through. In order to find a single dot, we must find the right location on the sample such that a single quantum dot is within the mode waist and has a size different enough from the others that it can be considered spectrally isolated from its neighbors. Furthermore, the design of the spacer layer means that not just any isolated dot will do. The dot should have an energy corresponding to the etalon mode for the spacer or else the cavity mode will have an antinode away from the position of the quantum dot when it is resonant with the exciton transition — i.e. the goal is to find a spectrally isolated dot that matches the spacer-layer design wavelength. With a maximum lateral translation range of 50 μm , it is also possible that a much larger translation is necessary to find a region with optimal overlap of spectrally isolated dots with the spacer-layer resonance.

5.2 Improvements to the Apparatus

The current apparatus supports lateral scanning over an area of $250 \mu\text{m}^2$, limited by the stroke length of piezo actuators. It would not be difficult to adjust this design to allow for much increased scanning ranges. Another major improvement would be the inclusion of position sensors on the tripod legs and on the lateral actuators. This would give a much better control over the orientation of the cavity and would also provide the ability to move to specific locations on the sample. Due to hysteresis in the piezo actuators as well as large thermal expansions each time the sample is cooled and reheated, we were not able to reliably return to the same point on the sample on successive runs.

A way to read out the positions of each leg of the tripod would allow it to be used to effectively control the yaw and pitch. In the absence of information about the particular leg positions, the tripod was essentially used as a piston without regard to the angular orientation of the DBR. In practice this was not a huge problem because the input beam could be steered to align with cavity optical axis (whose direction is defined by the pitch and yaw values). Nonetheless, with the benefit of hindsight, a “next-generation” apparatus would include digital encoders for each tripod leg.

The dominant source of vibrations in the current incarnation of the apparatus is helium boiling inside of the cryostat. Newer cryostat and transfer tube designs

are capable of keeping the helium liquid inside of the cryostat. The passive stability of the cavity would improve if the turbulence associated with the boiling helium could be moved out of the cryostat and into the return path of the transfer tube.

5.3 Outlook

The properties of this cavity make it a good candidate for investigating non-paraxial modes. If small flat mirrors could be built, such as coated (optical) fiber-tips, then truly hemispherical micro-mirrors could be used to form a stable cavity. This isn't possible with current mirrors because the lateral dimension of the flat mirrors is orders of magnitude larger than that of the curved micro-mirror. If mirror coatings could be produced with high reflectivity over the entire hemispherical surface, then a cavity formed with a small-diameter flat-mirror could probe short, paraxial cavities all the way out to a truly hemispherical cavity. While the mirror geometry described in this dissertation support non-paraxial modes, there are predicted modes with angular spectrum exceeding what these mirrors can support. If the aim is to probe non-paraxial optics, then it would seem worthwhile to attempt to produce a curved mirror with even larger numerical aperture.

Of course, a curved micro-mirror attached to an immersion objective as used in this work could be used to investigate any variety of emitter located near the surface of a flat mirror. There appears to be some interest recently in using diamond color-centers [41, 62] and it should be possible to integrate these into a

monolithic mirror structure in a similar fashion to the integration of IFQDs into the DBRs used in this work.

Additionally, the proposal [55] to use biexciton emission from an anisotropic quantum dot as a source of polarization-entangled photons seems readily attainable for a cavity similar to the cavity described here. In that scheme it is desirable to match the FSR of the cavity to the biexciton shift and the linewidth to the anisotropy splitting. The range of bubble sizes produced by the technique described in this dissertation covers the biexciton shift for GaAs QDs (both self-assembled dots and IFQDs). A linewidth of a few tens of μeV would suffice and for a given FSR, is easily accessible with conventional coating techniques.

Although signatures of strong-coupling eluded us, significant achievements were made in constructing new and novel micro-cavities that have applications involving cavity-QED, quantum information science and non-paraxial optics.

APPENDIX A

TIME-DEPENDENCE OF EXPECTATION VALUES

The Hamiltonian for an open subsystem consisting of a two-level system interacting via a dipole interaction with a single mode of the electric field is given by (2.64):

$$\hat{\mathcal{H}} = \frac{\hbar\omega}{2}\hat{\sigma}_z + \hbar\nu\hat{a}^\dagger\hat{a} - \hbar g(\hat{a}^\dagger\hat{S}_- + \hat{a}\hat{S}_+)$$

The time-evolution of the density operator is determined by a master equation in the Lindblad form provided the Born-Markov and rotating wave approximations are justified (2.79).

$$\begin{aligned} \dot{\hat{\rho}} = \mathcal{L}\hat{\rho} = & \frac{1}{i\hbar} [\hat{\mathcal{H}}, \hat{\rho}] + \frac{\gamma}{2}(2\hat{S}_-\hat{\rho}\hat{S}_+ - \hat{S}_+\hat{S}_-\hat{\rho} - \hat{\rho}\hat{S}_+\hat{S}_-) \\ & + \kappa(2\hat{a}\hat{\rho}\hat{a}^\dagger - \hat{a}^\dagger\hat{a}\hat{\rho} - \hat{\rho}\hat{a}^\dagger\hat{a}) \\ & + \frac{\gamma_p}{2}(\hat{\sigma}_z\hat{\rho}\hat{\sigma}_z - 1). \end{aligned} \quad (\text{A.1})$$

Then the time evolution of operators may be found by multiplying both sides of (A.1) by the operator under consideration and taking the trace over the open subsystem. The time evolution of a general operator is thus,

$$\langle \dot{\hat{O}} \rangle = \text{tr} \{ \mathcal{L}\hat{\rho} \cdot \hat{O} \}$$

In this appendix the goal is to compute the expectation values of the operators \hat{a} , \hat{S}_- , $\hat{a}^\dagger\hat{a}$, $\hat{S}_+\hat{S}_-$ and $\hat{a}^\dagger\hat{S}_-$. This provides results needed for calculating spectra in chapter 2.

The differential equations for the single-time averages (expectation values) depends on the trace. A couple of properties of the trace will be exploited in this pursuit.

$$\text{tr}\{ABC\} = \text{tr}\{CAB\} = \text{tr}\{BCA\} \quad \begin{array}{l} \text{Invariance under cyclic} \\ \text{permutation of the order of its} \\ \text{arguments.} \end{array} \quad (\text{A.2})$$

$$\text{tr}\{A + B\} = \text{tr}\{A\} + \text{tr}\{B\} \quad \text{The trace is a linear map.} \quad (\text{A.3})$$

Because of these properties and linearity of the commutator, each term in the system Hamiltonian will yield a null contribution for those cases where the time evolution is being calculated for an operator that commutes with said term. In other words, suppose that $[\hat{N}, \hat{O}] = 0$. Then

$$\begin{aligned} \text{tr}\{[\hat{N}, \hat{\rho}]\hat{O}\} &= \text{tr}\{\hat{N}\hat{\rho}\hat{O} - \hat{\rho}\hat{N}\hat{O}\} \\ &= \text{tr}\{\hat{\rho}\hat{O}\hat{N}\} - \text{tr}\{\hat{\rho}\hat{N}\hat{O}\} \\ &= \text{tr}\{\hat{\rho}\hat{N}\hat{O}\} - \text{tr}\{\hat{\rho}\hat{N}\hat{O}\} \\ &= 0 \end{aligned}$$

Because of this, begin by omitting each commutator term in the master equation whose system operators commute with the operator whose expectation value is being calculated. Also, notice that the dissipative terms enclosed by parentheses each evaluate to zero if multiplied by a commuting operator (an operator that commutes with all operators other than the density operator) and traced over.

Now write down some relevant commutators for use in the following calculations:

$$[\hat{a}, \hat{a}^\dagger] = 1 \quad (\text{A.4a})$$

$$[\hat{S}_+, \hat{S}_-] = \hat{\sigma}_z \quad (\text{A.4b})$$

$$[\hat{S}_\pm, \hat{\sigma}_z] = \mp 2\hat{S}_\pm \quad (\text{A.4c})$$

Since we work in the 3-state basis of $\{|0, b\rangle, |1, b\rangle, |0, a\rangle\}$, it follows that any product of two raising (creation) or lowering (annihilation) operator corresponds to a null operator in this Hilbert space.

A final result before determining the dynamical equations for the expectation values: Find two useful triple products of the 2-level operators.

$$\hat{S}_+ \hat{S}_- \hat{S}_+ = |a\rangle\langle b|b\rangle\langle a|a\rangle\langle b| = |a\rangle\langle b| = \hat{S}_+ \quad (\text{A.5a})$$

$$\hat{S}_- \hat{S}_+ \hat{S}_- = |b\rangle\langle a|a\rangle\langle b|b\rangle\langle a| = |b\rangle\langle a| = \hat{S}_- \quad (\text{A.5b})$$

First calculate the time evolution for the field operator, \hat{a} :

$$\begin{aligned}
\langle \dot{\hat{a}} \rangle &= \text{tr} \left\{ -i\nu [\hat{a}^\dagger \hat{a}, \hat{\rho}] \hat{a} + ig [\hat{a}^\dagger \hat{S}_-, \hat{\rho}] \hat{a} + ig [\hat{a} \hat{S}_+, \hat{\rho}] \hat{a} \right\} \\
&\quad + \text{tr} \left\{ \frac{\gamma}{2} (2\hat{S}_- \hat{\rho} \hat{S}_+ - \hat{S}_+ \hat{S}_- \hat{\rho} - \hat{\rho} \hat{S}_+ \hat{S}_-) \hat{a} \right\} \\
&\quad + \text{tr} \left\{ \kappa (2\hat{a} \hat{\rho} \hat{a}^\dagger - \hat{a}^\dagger \hat{a} \hat{\rho} - \hat{\rho} \hat{a}^\dagger \hat{a}) \hat{a} \right\} \\
&\quad + \text{tr} \left\{ \frac{\gamma_p}{2} (\hat{\sigma}_z \hat{\rho} \hat{\sigma}_z - \hat{\rho}) \hat{a} \right\} \\
&= \text{tr} \left\{ -i\nu \underbrace{\rho[\hat{a}, \hat{a}^\dagger]}_{=1} \hat{a} + ig \hat{\rho} \underbrace{[\hat{a}, \hat{a}^\dagger]}_{=1} \hat{S}_- + \kappa \hat{\rho} \underbrace{[\hat{a}^\dagger, \hat{a}]}_{=-1} \hat{a} \right\}.
\end{aligned}$$

The result is

$$\boxed{\frac{d}{dt} \langle \hat{a} \rangle = -(\kappa + i\nu) \langle \hat{a} \rangle + ig \langle \hat{S}_- \rangle}. \quad (\text{A.6})$$

Next, find the ODE governing the time evolution of the two-level lowering operator:

$$\begin{aligned}
\langle \dot{\hat{S}}_- \rangle &= \text{tr} \left\{ -i\frac{\omega}{2} [\hat{\sigma}_z, \hat{\rho}] \hat{S}_- + ig [\hat{a} \hat{S}_+, \hat{\rho}] \hat{S}_- \right. \\
&\quad \left. + \frac{\gamma}{2} (2\hat{S}_- \hat{\rho} \hat{S}_+ - \hat{S}_+ \hat{S}_- \hat{\rho} - \hat{\rho} \hat{S}_+ \hat{S}_-) \hat{S}_- \right. \\
&\quad \left. + \frac{\gamma_p}{2} (\hat{\sigma}_z \hat{\rho} \hat{\sigma}_z - \hat{\rho}) \hat{S}_- \right\} \\
&= \text{tr} \left\{ -i\frac{\omega}{2} \hat{\rho} \overbrace{[\hat{S}_-, \hat{\sigma}_z]}^{2\hat{S}_-} + ig \hat{\rho} \hat{a} \overbrace{[\hat{S}_-, \hat{S}_+]}^{-\hat{\sigma}_z} \right. \\
&\quad \left. + \frac{\gamma}{2} (2\hat{\rho} \hat{S}_+ \hat{S}_- \hat{S}_- - \hat{\rho} \overbrace{\hat{S}_- \hat{S}_+ \hat{S}_-}^{\hat{S}_-} - \hat{\rho} \hat{S}_+ \hat{S}_-^2) \right. \\
&\quad \left. + \frac{\gamma_p}{2} (\hat{\rho} \overbrace{\hat{\sigma}_z \hat{S}_- \hat{\sigma}_z}^{-\hat{S}_-} - \hat{\rho} \hat{S}_-) \right\}
\end{aligned}$$

$$= -i\omega\langle\hat{S}_-\rangle - ig\langle\hat{a}\hat{\sigma}_z\rangle - \frac{\gamma}{2}\langle\hat{S}_-\rangle - \gamma_p\langle\hat{S}_-\rangle.$$

The observant reader will notice that one of the expectation values involved here is $\langle\hat{a}\hat{\sigma}_z\rangle$. The 3-state basis offers a way to simplify this expression. First, the expectation value of the annihilation operator may be written down as

$$\begin{aligned}\langle\hat{a}\rangle &= \langle\psi|\hat{a}|\psi\rangle = \langle\psi|\hat{a}(c_{0b}|0,b\rangle + c_{1b}|1,b\rangle + c_{0a}|0,a\rangle) \\ &= c_{1b}\langle\psi|0,b\rangle.\end{aligned}$$

Meanwhile the desired expectation value is

$$\begin{aligned}\langle\psi|\hat{a}\hat{\sigma}_z|\psi\rangle &= \langle\psi|\hat{a}(|a\rangle\langle a| - |b\rangle\langle b|)(c_{0b}|0,b\rangle + c_{1b}|1,b\rangle + c_{0a}|0,a\rangle) \\ &= -c_{1b}\langle\psi|0,b\rangle.\end{aligned}$$

Direct comparison leads to the conclusion that in the context of the Hilbert space spanned by the current 3-state basis, $\langle\hat{a}\hat{\sigma}_z\rangle = -\langle\hat{a}\rangle$. This yields the corresponding, simplified differential equation governing the time evolution of the lowering operator's expectation value.

$$\boxed{\frac{d}{dt}\langle\hat{S}_-\rangle = -\left(\frac{2\gamma_p + \gamma}{2} + i\omega\right)\langle\hat{S}_-\rangle + ig\langle a\rangle} \quad (\text{A.7})$$

The equations for $\langle\hat{a}^\dagger\rangle$ and $\langle\hat{S}_+\rangle$ can be obtained by simply taking the Hermitian adjoint of (A.6) and (A.7), respectively. Now we turn to the matter of calculating

the projection operators ($\hat{a}^\dagger\hat{a}$ and $\hat{S}_+\hat{S}_-$) for the excited states of the field and the two-level system.

$$\begin{aligned}
\frac{d}{dt}\langle\hat{a}^\dagger\hat{a}\rangle &= \text{tr}\left\{-i\nu[\hat{a}^\dagger\hat{a},\hat{\rho}]\hat{a}^\dagger\hat{a}+ig\left[\hat{a}^\dagger\hat{S}_-+\hat{a}\hat{S}_+,\hat{\rho}\right]\hat{a}^\dagger\hat{a}\right. \\
&\quad \left.+\kappa\left(2\hat{a}\hat{\rho}\hat{a}^\dagger\hat{a}-\hat{a}^\dagger\hat{a}\hat{\rho}\hat{a}^\dagger\hat{a}-\hat{\rho}\hat{a}^\dagger\hat{a}\hat{a}^\dagger\hat{a}\right)\right\} \\
&= \text{tr}\left\{-i\nu\left(\hat{\rho}\hat{a}^\dagger\hat{a}\hat{a}^\dagger\hat{a}-\hat{\rho}\hat{a}^\dagger\hat{a}\hat{a}^\dagger\hat{a}\right)+ig\left[\hat{\rho}\hat{S}_-\left(\hat{a}^\dagger\hat{a}\hat{a}^\dagger-\hat{a}^\dagger\hat{a}^\dagger\hat{a}\right)\right.\right. \\
&\quad \left.\left.+ig\left[\hat{\rho}\hat{S}_+\left(\hat{a}^\dagger\hat{a}\hat{a}-\hat{a}\hat{a}^\dagger\hat{a}\right)\right]-2\kappa\hat{\rho}\hat{a}^\dagger\left(1-\hat{a}^\dagger\hat{a}\right)\hat{a}\right\} \\
&= \text{tr}\left\{ig\hat{\rho}\hat{S}_-\hat{a}^\dagger-ig\hat{\rho}\hat{S}_+\hat{a}-2\kappa\hat{\rho}\hat{a}^\dagger\hat{a}\right\}
\end{aligned}$$

We see that the number operator evolves in time according to

$$\boxed{\frac{d}{dt}\langle\hat{a}^\dagger\hat{a}\rangle=-2\kappa\langle\hat{a}^\dagger\hat{a}\rangle-ig\langle\hat{a}^\dagger\hat{S}_-\rangle+\text{h.c.}}, \quad (\text{A.8})$$

where h.c. represents the Hermitian conjugate.

The next task is to determine the differential equation governing the time evolution for the projection operator into the excited state of the two-level system.¹

$$\begin{aligned}
\frac{d}{dt}\langle\hat{S}_+\hat{S}_-\rangle &= \text{tr}\left\{-i\frac{\omega}{2}\left[\hat{\sigma}_z,\hat{\rho}\right]\hat{S}_+\hat{S}_-+ig\left[\hat{a}\hat{S}_++\hat{a}^\dagger\hat{S}_-,\hat{\rho}\right]\hat{S}_+\hat{S}_-\right. \\
&\quad \left.+\frac{\gamma}{2}\left(2\hat{S}_-\hat{\rho}\hat{S}_+-\hat{S}_+\hat{S}_-\hat{\rho}-\hat{\rho}\hat{S}_+\hat{S}_-\right)\hat{S}_+\hat{S}_-\right\}
\end{aligned}$$

¹We can evaluate the operator $\hat{S}_+\hat{S}_-$ by writing it in terms of the states of the two-level system: $\hat{S}_+\hat{S}_-=|a\rangle\langle b|b\rangle\langle a|=|a\rangle\langle a|$

$$\begin{aligned}
& + \frac{\gamma_p}{2}(\hat{\sigma}_z \hat{\rho} \hat{\sigma}_z - \hat{\rho}) \hat{S}_+ \hat{S}_- \} \\
= & \text{tr} \{ -i \frac{\omega}{2} \hat{\rho} (\hat{S}_+ \hat{S}_- \hat{\sigma}_z - \hat{\sigma}_z \hat{S}_+ \hat{S}_-) + ig \hat{\rho} (\hat{a}^\dagger \hat{S}_+ \hat{S}_-^2 + \hat{a} \hat{S}_+ \hat{S}_- \hat{S}_+ \\
& - \hat{a}^\dagger \hat{S}_- \hat{S}_+ \hat{S}_- - \hat{a} \hat{S}_+^2 \hat{S}_-) - \frac{\gamma}{2} \hat{\rho} (\hat{S}_+ \hat{S}_- \hat{S}_+ \hat{S}_- + \hat{S}_+ \hat{S}_- \hat{S}_+ \hat{S}_-) \\
& + \frac{\gamma_p}{2} \hat{\rho} (\hat{\sigma}_z \hat{S}_+ \hat{S}_- \hat{\sigma}_z - \hat{S}_+ \hat{S}_-) \} \\
= & \{ -i \frac{\omega}{2} \hat{\rho} (|a\rangle\langle a| - |a\rangle\langle a|) + ig \hat{\rho} (\hat{a} \hat{S}_+ - \hat{a}^\dagger \hat{S}_-) \\
& - \gamma \hat{\rho} \hat{S}_+ \hat{S}_- - \frac{\gamma_p}{2} \hat{\rho} (\hat{S}_+ \hat{S}_- - \hat{S}_+ \hat{S}_-) \},
\end{aligned}$$

which provides the final form of the differential equation for $\hat{S}_+ \hat{S}_-$,

$$\boxed{\frac{d}{dt} \langle \hat{S}_+ \hat{S}_- \rangle = -\gamma \langle \hat{S}_+ \hat{S}_- \rangle - ig \hat{a}^\dagger \hat{S}_- + \text{h.c.}} \quad (\text{A.9})$$

The final independent expectation value that needs to be solved for is $\hat{a}^\dagger \hat{S}_-$.

$$\begin{aligned}
\frac{d}{dt} \langle \hat{a}^\dagger \hat{S}_- \rangle & = \text{tr} \{ -i \frac{\omega}{2} [\hat{\sigma}_z, \hat{\rho}] \hat{a}^\dagger \hat{S}_- - i\nu [\hat{a}^\dagger \hat{a}, \hat{\rho}] \hat{a}^\dagger \hat{S}_- + ig [\hat{a} \hat{S}_+, \hat{\rho}] \hat{a}^\dagger \hat{S}_- \\
& + \kappa (2\hat{a} \hat{\rho} \hat{a}^\dagger - \hat{a}^\dagger \hat{a} \hat{\rho} - \hat{\rho} \hat{a}^\dagger \hat{a}) \hat{a}^\dagger \hat{S}_- \\
& + \frac{\gamma}{2} (2\hat{S}_- \hat{\rho} \hat{S}_+ - \hat{S}_+ \hat{S}_- \hat{\rho} - \hat{\rho} \hat{S}_+ \hat{S}_-) \hat{a}^\dagger \hat{S}_- \\
& + \frac{\gamma_p}{2} (\hat{\sigma}_z \hat{\rho} \hat{\sigma}_z - \hat{\rho}) \hat{a}^\dagger \hat{S}_- \} \\
= & \text{tr} \{ -i \frac{\omega}{2} \hat{\rho} \hat{a}^\dagger [\hat{S}_-, \hat{\sigma}_z] - i\nu \hat{\rho} \hat{a}^\dagger [\hat{a}^\dagger, \hat{a}] \hat{S}_- + ig \hat{\rho} (\hat{a}^\dagger \hat{a} \hat{S}_- \hat{S}_+ - \hat{a} \hat{a}^\dagger \hat{S}_+ \hat{S}_-) \\
& - \kappa \hat{\rho} (\hat{a}^\dagger \hat{a}^\dagger \hat{a} + \hat{a}^\dagger \hat{a} \hat{a}^\dagger) \hat{S}_- \\
& + \frac{\gamma}{2} \hat{\rho} \hat{a}^\dagger (2\hat{S}_+ \hat{S}_-^2 - \hat{S}_- \hat{S}_+ \hat{S}_- - \hat{S}_+ \hat{S}_-^2)
\end{aligned}$$

$$+ \frac{\gamma_p}{2} \hat{\rho} (\hat{\sigma}_z \hat{a}^\dagger \hat{S}_- \hat{\sigma}_z - \hat{a}^\dagger \hat{S}_-).$$

Because $\hat{\sigma}_z \hat{S}_- \hat{\sigma}_z = (|a\rangle\langle a| - |b\rangle\langle b|) |b\rangle\langle a| (|a\rangle\langle a| - |b\rangle\langle b|) = -|b\rangle\langle a| = -\hat{S}_-$, this can be written as

$$\begin{aligned} \frac{d}{dt} \langle \hat{a}^\dagger \hat{S}_- \rangle &= \text{tr} \{ -i\omega \hat{\rho} \hat{a}^\dagger \hat{S}_- + i\nu \hat{\rho} \hat{a}^\dagger \hat{S}_- + ig \hat{\rho} (-\hat{a}^\dagger \hat{a} \hat{\sigma}_z - \hat{S}_+ \hat{S}_-) \\ &\quad - \kappa \hat{\rho} (\hat{a}^\dagger - \hat{a}^\dagger \hat{a}^\dagger \hat{a}) \hat{S}_- \\ &\quad - \frac{\gamma}{2} \hat{\rho} \hat{a}^\dagger \hat{S}_- \\ &\quad + \frac{\gamma_p}{2} (-2\hat{a}^\dagger \hat{S}_-) \} \\ &= -i\omega \langle \hat{a}^\dagger \hat{S}_- \rangle + i\nu \langle \hat{a}^\dagger \hat{S}_- \rangle - ig (\langle \hat{a}^\dagger \hat{a} \hat{\sigma}_z \rangle + \langle \hat{S}_+ \hat{S}_- \rangle) \\ &\quad - \kappa \langle \hat{a}^\dagger \hat{S}_- \rangle - \frac{\gamma}{2} \langle \hat{a}^\dagger \hat{S}_- \rangle - \gamma_p \langle \hat{a}^\dagger \hat{S}_- \rangle \end{aligned}$$

As before, the expectation value $\langle \hat{a}^\dagger \hat{a} \hat{\sigma}_z \rangle$ can be simplified in the 3-state Hilbert space.

$$\begin{aligned} \langle \psi | \hat{a}^\dagger \hat{a} | \psi \rangle &= \langle \psi | \hat{a}^\dagger \hat{a} (c_{0b} |0, b\rangle + c_{1b} |1, b\rangle + c_{0a} |0, a\rangle) = c_{1b} \langle \psi | 1, b \rangle ; \\ \langle \psi | \hat{a}^\dagger \hat{a} \hat{\sigma}_z | \psi \rangle &= \langle \psi | \hat{a}^\dagger \hat{a} \hat{\sigma}_z (c_{0b} |0, b\rangle + c_{1b} |1, b\rangle + c_{0a} |0, a\rangle) = -c_{1b} \langle \psi | 1, b \rangle = -\langle \hat{a}^\dagger \hat{a} \rangle \end{aligned}$$

Using this result, the differential equation governing the time evolution of $\langle \hat{a}^\dagger \hat{S}_- \rangle$ can be written in simplified form as

$$\boxed{\frac{d}{dt} \langle \hat{a}^\dagger \hat{S}_- \rangle = - \left(\kappa + \frac{\gamma}{2} + \gamma_p + i\Delta \right) \langle \hat{a}^\dagger \hat{S}_- \rangle - ig \left(\langle \hat{S}_+ \hat{S}_- \rangle - \langle \hat{a}^\dagger \hat{a} \rangle \right)} \quad (\text{A.10})$$

APPENDIX B

QUANTIZATION OF A PARAXIAL RESONATOR

In this appendix, the problem of determining the fields and mode-volume inside of a stable, paraxial resonator will be considered. Quantization may be performed by canonical quantization once the Hamiltonian has been written in the form of a classical, canonical coordinate and its time-derivative: $H(q, \dot{q})$. However, this step is carried out in chapter 2 and will not be repeated here.

The basic strategy is to specify the electric and magnetic fields satisfying the Helmholtz equation and subject to the boundary conditions of a resonator whose surfaces are sections of spheres. Once these have been specified then the classical Hamiltonian may be calculated by integrating the electrodynamic energy density over the volume of the intra-cavity fields. This turns out to consist of some position-independent factors multiplied against the integral of the mode intensity over the volume of the cavity (or unit cell in the case of periodic boundary conditions).

B.1 Classical Field of the Resonator

The resonator contains no sources, so any electric or magnetic fields must satisfy the vacuum Maxwell's equations. In particular, we seek solutions to the vacuum

wave equation.

$$\left(\nabla^2 - \frac{1}{c^2} \frac{\partial^2}{\partial t^2}\right) \mathbf{E} = 0$$

In Cartesian coordinates, the vector Laplacian can be written in a simple form.

$$\nabla^2 \begin{bmatrix} E_x \\ E_y \\ E_z \end{bmatrix} = \begin{bmatrix} \nabla^2 E_x \\ \nabla^2 E_y \\ \nabla^2 E_z \end{bmatrix}. \quad (\text{B.1})$$

Due to (B.1) we can write the wave equation as a set of individual scalar equations in Cartesian coordinates. In this case, we consider a paraxial mode of a resonator bounded by two spherical, reflective boundaries. The transverse nature of the field tells us that the polarization vectors for the fields will lie in spherical surfaces in the neighborhood of the optical axis. The immediate task is to write this in terms of Cartesian coordinates so that the simplification allowed by B.1 can be exploited.

Due to a coordinate singularity in spherical coordinates¹ it is desirable to use a modified set of spherical coordinates to describe the orientation of the polarization vectors. The singularity can be nicely avoided by choosing the polar angle to be zero along the x-axis rather than the z-axis. Due to this change we now have $\sin \theta \approx \pi/2$ and $\phi \approx \pi/2$ close to the optical axis. Additionally, the transformation

¹Points on the z-axis correspond to $(z, 0, \phi)$ — the azimuthal coordinate is completely undefined. Two dimensional polar coordinates the origin has an analogous coordinate singularity. The origin occurs at $\rho = 0$ while ϕ is undefined.

from spherical basis vectors to Cartesian basis vectors takes place as follows:

$$\begin{bmatrix} \hat{r} \\ \hat{\theta} \\ \hat{\phi} \end{bmatrix} = \begin{bmatrix} \cos \theta & \sin \theta \cos \phi & \sin \theta \sin \phi \\ -\sin \theta & \cos \theta \cos \phi & \cos \theta \sin \phi \\ 0 & -\sin \phi & \cos \phi \end{bmatrix} \cdot \begin{bmatrix} \hat{x} \\ \hat{y} \\ \hat{z} \end{bmatrix}.$$

Thus, we have $\hat{\theta} = -\sin \theta \hat{x} + \cos \theta \cos \phi \hat{y} + \cos \theta \sin \phi \hat{z} \approx -\hat{x} + \frac{x}{z} \hat{y} + \frac{x}{z} \hat{z}$ in the vicinity of the optical axis but away from $z = 0$. This provides us with a relationship between the amplitudes of the different electric field vector's Cartesian components that satisfies the condition of lying within a spherical surface and near the optical axis.

This constraint allows the wave equation to be written as the following:

$$\begin{bmatrix} -\nabla^2 E_0(\mathbf{r}, t) \\ 0 \\ \nabla^2 \frac{x}{z} E_0(\mathbf{r}, t) \end{bmatrix} = \frac{1}{c^2} \begin{bmatrix} -\partial_t^2 E_0(\mathbf{r}, t) \\ 0 \\ \frac{x}{z} \partial_t^2 E_0(\mathbf{r}, t) \end{bmatrix}. \quad (\text{B.2})$$

Each component obeys a scalar wave equation. This can be attacked by the usual separation of variables. Suppose that $E_0(\mathbf{r}, t) = R(\mathbf{r}) \cdot T(t)$. Then the equality of the first row requires that

$$\begin{aligned} -\nabla^2 [R(\mathbf{r}) \cdot T(t)] &= -\frac{1}{c^2} \partial_t^2 [R(\mathbf{r}) \cdot T(t)] \\ \Rightarrow \frac{\nabla^2 R(\mathbf{r})}{R(\mathbf{r})} &= \frac{\ddot{T}(t)}{T(t)} \end{aligned}$$

Proceed by noticing that the only way for the equation to hold is if each side is, separately, equal to the same constant. Rewrite as two equations and utilize a clever choice of separation constant.

$$\begin{aligned} \frac{\nabla^2 R(\mathbf{r})}{R(\mathbf{r})} &= -k^2 \\ \Rightarrow \frac{\ddot{T}(t)}{c^2 T(t)} &= -k^2 \end{aligned}$$

This yields

$$\nabla^2 R(\mathbf{r}) + k^2 R(\mathbf{r}) = 0 \tag{B.3}$$

and

$$\frac{d^2}{dt^2} T(t) + (kc)^2 T(t) = 0. \tag{B.4}$$

Here, (B.3) is the Helmholtz equation, while (B.4) provides for a harmonic time-dependent part. Formally, this can be demonstrated by converting the second order ODE into a system of two first-order ODEs and solving the characteristic equation to find the eigenvalues. The general solution to equation (B.4) can then be written as

$$T(t) = T_+ e^{i\lambda_- t} + T_- e^{-i\lambda_+ t}, \tag{B.5}$$

where λ_{\pm} are the two eigenvalues. The characteristic equation trivially leads to two imaginary eigenvalues, $\lambda_{\pm} = \pm\nu$, where $\nu = kc$. Inserting these values into (B.5)

provides the solution in this case.

$$T(t) = T_+ e^{i\nu t} + T_- e^{-i\nu t}. \quad (\text{B.6})$$

The main goal here is to solve the Helmholtz equation (B.3) as that provides for the spatial characteristics of the field. Since we consider here the standing wave modes of an optical resonator we can appropriately make a quasi-monochromatic or slowly-varying envelope approximation. The slowly varying envelope means that the spectrum for the field is narrow around the wavenumber of the plane wave. The spread of wavenumbers present in a Fourier decomposition of the envelope is small and therefore the corresponding length scale over which changes occur along the optical axis is long compared to the wavelength. That is, suppose that

$$R(\mathbf{r}) = A(\mathbf{r}) e^{ikz}. \quad (\text{B.7})$$

The slowly varying envelope approximation constrains the variations of the envelope function, A , so that

$$\left| \frac{\partial^2 A}{\partial z^2} \right| \ll \left| k \frac{\partial A}{\partial z} \right| \ll |k^2 A|. \quad (\text{B.8})$$

When (B.8) is inserted into (B.3) it permits the following,

$$\begin{aligned}
 (\nabla^2 + k^2)R(\mathbf{r}) &= (\nabla^2 + k^2)A(\mathbf{r})e^{ikz} \\
 &= \left(\frac{\partial^2}{\partial x^2} + \frac{\partial^2}{\partial x^2} \right) A(\mathbf{r})e^{ikz} + \left(\frac{\partial^2}{\partial z^2} + k^2 \right) A(\mathbf{r})e^{ikz} \\
 &= \nabla_T^2 A(\mathbf{r})e^{ikz} + \frac{\partial^2 A(\mathbf{r})}{\partial z^2} e^{ikz} \\
 &\quad + 2ik \frac{\partial A(\mathbf{r})}{\partial z} e^{ikz} - \cancel{k^2 A(\mathbf{r})e^{ikz}} + \cancel{k^2 A(\mathbf{r})e^{ikz}} \\
 &= 0.
 \end{aligned}$$

It is now clear that $R(\mathbf{r})$ will be a solution of the Helmholtz equation (B.3) provided that the envelope function obeys a paraxial Helmholtz equation:

$$\nabla_T^2 A(\mathbf{r}) + 2ik \frac{\partial A(\mathbf{r})}{\partial z} = 0. \quad (\text{B.9})$$

Taking a small sideways step, it's also possible to assert that a spherical wave is a well known solution to the Helmholtz equation whose wavefronts are spherical surfaces. Invoking the paraxial approximation, the corresponding wave is a parabolic wave.

$$\begin{aligned}
\frac{Ae^{ikr}}{r} &= \frac{Ae^{ik\sqrt{x^2+y^2+z^2}}}{\sqrt{x^2+y^2+z^2}} \\
&= \frac{Ae^{ikz\sqrt{1+\frac{x^2+y^2}{z^2}}}}{z\sqrt{1+\frac{x^2+y^2}{z^2}}} \\
&\approx \underbrace{\frac{Ae^{ik\left(\frac{x^2+y^2}{2z}\right)}}{z}}_{A(\mathbf{r})} \cdot e^{ikz}.
\end{aligned}$$

This provides an example that the paraxial approximation already contains the essential content of the slowly varying envelope approximation.

The equation determining E_z just turns out to be obtained from the equation for E_x by a simple substitution:

$$\begin{aligned}
\nabla^2 \left(\frac{x}{z} \cdot E_0(\mathbf{r}, t) \right) &= \frac{x}{zc^2} \frac{\partial^2 E_0(\mathbf{r}, t)}{\partial t^2} \\
\Rightarrow T(t) \nabla^2 \left(\frac{x}{z} \cdot R(\mathbf{r}) \right) &= \frac{xR(\mathbf{r})}{zc^2} \frac{\partial^2 T(t)}{\partial t^2} \\
\Rightarrow \frac{z}{xR(\mathbf{r})} \nabla^2 \left(\frac{x}{z} \cdot R(\mathbf{r}) \right) &= \frac{1}{c^2 T(t)} \cdot \frac{\partial^2 T(t)}{\partial t^2}.
\end{aligned}$$

Necessarily, the same equation is obtained (B.4) for the time dependence as before. Meanwhile, the spatial equation is

$$\nabla^2 \left(\frac{x}{z} \cdot R(\mathbf{r}) \right) = -k^2 \frac{xR(\mathbf{r})}{z}, \tag{B.10}$$

which, not surprisingly, is just the equation obtained for E_x by taking $R \rightarrow \frac{x}{z}R$.

Since we already have solved for $R(\mathbf{r})$ it is straightforward to verify that it remains a solution to the Helmholtz equation when multiplied by x/z .

So, a paraboloidal field of the following form obeys the boundary condition for a single spherical equipotential surface $z \neq 0$:

$$\mathbf{E}(\mathbf{r}, t) = E_0 \left(-\hat{x} + \frac{x}{z}\hat{z} \right) \frac{A_0 e^{ik\left(\frac{x^2+y^2}{2z}\right)}}{z} e^{ikz}. \quad (\text{B.11})$$

However, as pointed out previously, this field runs into problems at $z = 0$. The field's amplitude is undefined in the entire plane! The oscillatory part of the envelope also begins to oscillate arbitrarily quickly under approach of $z = 0$. To avoid these difficulties and permit cavities that include a flat surface at $z = 0$ — such as the cavity employed in the current experimental work — it suffices to move the pole away from the real axis by taking $z \rightarrow q(z) = z - iz_R$. The resulting solution is the Gaussian beam. Its wavefronts are flat at $z = 0$ while retaining spherical wavefronts everywhere (flat corresponds to a circle of infinite radius of curvature). Additionally, the curvature of a wavefront intersecting the optical axis at $z = z'$ can be tuned by selecting a different z_R .

The q-parameter is often written in terms of more physically meaningful quantities. This provides a representation for the beam in terms of understandable physical quantities, such as the radius of the beam (as measured to the distance

from the optical axis where the intensity drops to a value of $1/e^2$ compared to the value on the axis), the radius of curvature of the wavefronts, and a residual phase shift (the Gouy phase).

The Gaussian envelope is:

$$A(\mathbf{r}) = \frac{A_0}{q(z)} \exp \left[\frac{ik(x^2 + y^2)}{2q(z)} \right]; \quad (\text{B.12})$$

where $q(z)$ is the complex q parameter, $z - iz_R$. A representation of the beam written in terms of more physical properties of the beam can be obtained by defining the following:

$$\frac{1}{q(z)} \equiv \frac{z}{z^2 + z_R^2} + i \frac{z_R}{z^2 + z_R^2} = \frac{1}{R(z)} + i \frac{\lambda}{\pi W^2(z)}, \quad (\text{B.13})$$

where the following definitions have been made:

$$\begin{aligned} w_0 &\equiv \sqrt{\frac{\lambda z_R}{\pi}}; \\ w(z) &\equiv w_0 \sqrt{1 + \left(\frac{z}{z_R}\right)^2}; \\ R(z) &\equiv z \left[1 + \left(\frac{z_R}{z}\right)^2 \right]. \end{aligned} \quad (\text{B.14})$$

$w(z)$ is the cylindrical radius of the $1/e^2$ contour, w_0 is the radius at the waist — located at $z = 0$ — and $R(z)$ is the radius of curvature of the wavefronts at distance along the optical axis given by r . By applying (B.13) and (B.14) to (B.12)

a representation allowing more direct physical interpretation is obtained.

$$\begin{aligned}
A(\mathbf{r}) &= A_0 \left(\frac{1}{R(z)} + i \frac{\lambda}{\pi W^2(z)} \right) \exp \left[\frac{ik(x^2 + y^2)}{2} \left(\frac{1}{R(z)} + i \frac{\lambda}{\pi W^2(z)} \right) \right] \\
&= A_0 \left(\frac{1}{R(z)} + i \frac{\lambda}{\pi W^2(z)} \right) \exp \left[\frac{ik(x^2 + y^2)}{2R(z)} \right] \exp \left[-\frac{k(x^2 + y^2)\lambda}{2\pi W^2(z)} \right] \\
&= \frac{A_0}{z_R} \left(\frac{z_R}{R(z)} + i \frac{w_0^2}{W^2(z)} \right) \cdot F = \frac{A_0}{z_R} \left(\frac{z}{z_R} \frac{w_0^2}{W^2(z)} + i \frac{w_0^2}{W^2(z)} \right) \cdot F \\
&= i \frac{A_0 \cdot w_0}{z_R \cdot w(z)} \left[\frac{w_0}{w(z)} \left(1 - i \frac{z}{z_R} \right) \right] \cdot F = i \frac{A_0 \cdot w_0}{z_R \cdot w(z)} \left[\frac{\left(1 - i \frac{z}{z_R} \right)}{\sqrt{1 + \left(\frac{z}{z_R} \right)^2}} \right] \cdot F \\
&= \frac{iA_0}{z_R} \cdot \frac{w_0}{w(z)} \sqrt{\frac{1 - i \frac{z}{z_R}}{1 + i \left(\frac{z}{z_R} \right)^2}} \cdot F \\
&= \frac{iA_0}{z_R} \cdot \frac{w_0}{w(z)} \exp \left[-i \arctan \left(\frac{z}{z_R} \right) \right] \cdot F,
\end{aligned}$$

where F has been used temporarily to stand in for the appropriate exponential factors. The final step follows from the identity [26]:

$$\arctan \xi = \frac{1}{2i} \ln \frac{1 + i\xi}{1 - i\xi}.$$

Without loss of generality, the constant factors in the front of the expression may be absorbed into A_0 , since it is an unspecified complex number to be determined by boundary conditions. Define the resulting phase factor arising from the above identity as $\zeta(z) = \arctan \frac{z}{z_R}$. This finally leaves the Gaussian envelope in its familiar form.

$$A(\mathbf{r}) = A_0 \frac{w_0}{w(z)} \exp \left[-\frac{\rho^2}{w^2(z)} \right] \cdot \exp \left[ik \frac{\rho^2}{2R(z)} - i\zeta(z) \right]. \quad (\text{B.15})$$

Absorption of a factor of $1/z_R$ into the coefficient A_0 appears consistent when considering the units of A_0 in (B.12) in comparison to those of A_0 in (B.15). At this point the electric field inside of the cavity has been determined. Recalling that the general solution permits combinations of both eigenvalues, take this opportunity to replace e^{ikz} with $\cos(kz)$ to reflect a priori knowledge that the cavity mode contains waves traveling in both directions due to reflections at the mirror surfaces.

$$\mathbf{E}(\mathbf{r}, t) = A_1 T(t) \left(-\hat{x} + \frac{x}{z - iz_R} \hat{z} \right) \frac{w_0}{w(z)} e^{-\frac{\rho^2}{w^2(z)}} \exp \left[ik \frac{\rho^2}{2R(z)} - i\zeta(z) \right] \cos(kz) \quad (\text{B.16})$$

Having found the electric field it is straightforward to calculate the corresponding magnetic field. The corresponding \mathbf{B} field can be determined by using Maxwell's equations. Begin by invoking Faraday's Law. In differential form and SI units it has the following form:

$$-\partial_t \mathbf{B} = \nabla \times \mathbf{E}.$$

Calculating the curl of the electric field is straight-forward. After differentiating and invoking the paraxial approximation to eliminate terms of greater than first

order in x/z or y/z , the following expression remains:

$$\partial_t \mathbf{B}(\mathbf{r}, t) = A(\mathbf{r})T(t) \begin{bmatrix} 0 \\ 1k \sin(kz) \\ \frac{ky}{q(z)} \cos(kz) \end{bmatrix}$$

Next, differentiate once more and satisfy the remaining Maxwell-Ampere equation by invoking the wave equation.

$$\ddot{\mathbf{B}}(\mathbf{r}) = A(\mathbf{r})\dot{T}(t) \begin{bmatrix} 0 \\ k \sin(kz) \\ \frac{ky}{q(z)} \cos(kz) \end{bmatrix} \quad (\text{B.17})$$

The magnetic field obeys an identical wave equation. This leads to the same separation of variables resulting in harmonic time dependence and a Helmholtz equation, permitting $\nabla^2 \mathbf{B} = -k^2 \mathbf{B}$.

$$\begin{aligned} \frac{1}{c^2} \ddot{\mathbf{B}} &= \nabla^2 \mathbf{B} \\ \Rightarrow \ddot{\mathbf{B}} &= -\nu^2 \mathbf{B}. \end{aligned} \quad (\text{B.18})$$

Use the result of (B.18) with (B.17). This gives the magnetic field.

$$\mathbf{B}(\mathbf{r}, t) = -\frac{A(\mathbf{r})\dot{T}(t)}{\nu^2} \begin{bmatrix} 0 \\ k \sin(kz) \\ \frac{iky}{q(z)} \cos(kz) \end{bmatrix} \quad (\text{B.19})$$

Having obtained the form of the magnetic field we turn to the matter of calculating the energy in the field. Express the electrodynamic energy as the volume integral of the energy density using the fields determined previously.

From classical theory [27], the energy density may be written in the following way:

$$U = \frac{1}{2} \left(\epsilon_0 |\mathbf{E}|^2 + \frac{1}{\mu_0} |\mathbf{B}|^2 \right). \quad (\text{B.20})$$

The total energy depends upon the intensities of the electric and magnetic fields integrated over a characteristic volume. Because the energy depends on the square of the modulus of the fields we can neglect the longitudinal component of each of the fields: After squaring, the longitudinal electric and magnetic field components will be, respectively, $O\left(\left(\frac{x}{z}\right)^2\right)$ and $O\left(\left(\frac{y}{z}\right)^2\right)$.

$$\begin{aligned}
H &= \frac{1}{2} \int_V d^3\mathbf{r} \left(\epsilon_0 \mathbf{E}^2 + \frac{1}{\mu_0} \mathbf{B}^2 \right) \\
&= \frac{1}{2} \int_V d^3\mathbf{r} |A(\mathbf{r})|^2 \left[\epsilon_0 T^2(t) \cos^2(kz) + \frac{1}{\mu_0} \frac{\epsilon_0 \mu_0}{\nu^2} \dot{T}^2(t) k^2 \sin^2(kz) \right] \\
&= \frac{1}{2} \epsilon_0 \int_V d^3\mathbf{r} |A(\mathbf{r})|^2 \left(T^2(t) \cos^2(kz) + \frac{1}{\nu^2} \dot{T}^2(t) \sin^2(kz) \right)
\end{aligned}$$

Notice that the integral is essentially over the squared modulus of the resonator mode function, $R(\mathbf{r})$. To proceed we calculate the mode volume for the Gaussian beam. Both terms are a Gaussian envelope applied to a standing wave which is integrated over many wavelengths. Calculation will be done for the electric-field mode function, but the reader should note that an identical calculation carries through for the magnetic field.

The mode function for the electric field is:

$$R(\mathbf{r}) = A_0 \frac{w_0}{w(z)} \exp \left[-\frac{\rho^2}{W^2(z)} \right] \exp \left[i \frac{\rho^2}{2R(z)} - i\zeta(z) \right] \cos(kz). \quad (\text{B.21})$$

Taking the modulus square of this we have:

$$|R(\mathbf{r})|^2 = A_0^2 \frac{w_0^2}{W^2(z)} \exp \left[-\frac{2\rho^2}{W^2(z)} \right] \cos^2(kz). \quad (\text{B.22})$$

Once again, the mode volume is the integral of the mode-intensity over the cavity volume. This may now be written as:

$$\begin{aligned}
\int_V d^3\mathbf{r} |R(\mathbf{r})|^2 &= A_0^2 \int_V d\tau \frac{w_0^2}{W^2(z)} \exp\left[-\frac{2\rho^2}{W^2(z)}\right] \cos^2(kz) \\
&= A_0^2 w_0^2 \int_0^{2\pi} \int_0^\infty \int_0^L \rho d\rho d\phi dz \frac{1}{W^2(z)} \exp\left[-\frac{2\rho^2}{W^2(z)}\right] \cos^2(kz) \\
&= 2\pi A_0^2 w_0^2 \int_0^L dz \frac{1}{W^2(z)} \cos^2(kz) \int_0^\infty \rho d\rho \exp\left[-\frac{2\rho^2}{W^2(z)}\right]
\end{aligned}$$

The ρ integral can be performed directly via substitution. Let $\xi = -\frac{2\rho^2}{W^2(z)}$. Then $d\xi = -\frac{4\rho}{W^2(z)} d\rho$. This allows us to re-write the integral in the following way:

$$\begin{aligned}
\int_V d^3\mathbf{r} |R(\mathbf{r})|^2 &= 2\pi A_0^2 w_0^2 \int_0^L dz \frac{1}{W^2(z)} \cos^2(kz) \int_0^{-\infty} \frac{W^2(z)}{-4} d\xi e^\xi \\
&= \frac{\pi}{2} A_0^2 w_0^2 \int_0^L dz \cos^2(kz) \\
&= \frac{\pi}{4} A_0^2 w_0^2 L.
\end{aligned}$$

The above result is actually an approximate upper bound due to integration over an interval of $[0, \infty]$ in ρ . In the case of an extremely paraxial limit this approximation seems justified as this is consistent with a mirror with very large radius of curvature. The above calculation is for a region of space bounded by two flat mirrors enclosing a Gaussian beam.

The effective mode volume is a volume that, when multiplied against the squared modulus of the mode function evaluated at the location of the emitter, provides the same numerical result as integrating the modulus of the mode function over the actual volume of the cavity. It is defined by:

$$\int_V d^3\mathbf{r} |R(\mathbf{r})|^2 = |R(\mathbf{r}_{2-level})|^2 \cdot V_{\text{eff}}. \quad (\text{B.23})$$

Take the position of the atom to be at the cylindrical coordinates $(0, \phi, 0)$. When inserted into (B.22) this provides us with $|R(\mathbf{r}_{2-level})|^2 = |A_0|^2$. Inserting this into (B.23) provides the effective mode volume:

$$V_{\text{eff}} = \frac{\pi w_0^2 L}{4}. \quad (\text{B.24})$$

Armed with this insight, it is possible to write down the total energy in a more suggestive way.

$$H = \frac{1}{2} \epsilon_0 V_{\text{eff}} |A_0|^2 \left(T^2(t) + \frac{1}{\nu^2} \dot{T}^2(t) \right) \quad (\text{B.25})$$

Without loss of generality, we can scale the coefficient and the amplitude of $T(t)$.

Scale the coefficient so that:

$$A_0 = \sqrt{\frac{2\nu^2}{\epsilon_0 V_{\text{eff}}}}.$$

Define the scaled dynamical variable as $q(t) = \sqrt{\frac{\epsilon_0 V_{\text{eff}}}{2\nu^2}} T(t)$. This leaves the Hamiltonian in the following familiar form:

$$H = \frac{1}{2} (\nu^2 q^2 + \dot{q}^2).$$

This is the energy of a classical harmonic oscillator with unit mass, such that $p = \dot{q}$

$$\boxed{H = \frac{1}{2} (\nu^2 q^2 + p^2)}. \quad (\text{B.26})$$

APPENDIX C

ACRONYMS

AlGaAs $\text{Al}_x\text{Ga}_{1-x}\text{As}$. An alloy with a molar fraction of Al (Ga) of x ($1-x$).

ALE atomic layer epitaxy. A coating technique that uses self-limiting chemical reactions to allow epitaxial growth. It provides a conformal coating but tends to suffer from higher scattering than traditional coating techniques.

AOM acousto-optic modulator. A device that uses Bragg scattering off of a moving grating comprised of pressure waves (sound) in a crystal. Diffracted beams exhibit frequency shifts as well as angular shifts and the diffracted orders may be modulated by controlling the driving signal into the crystal.

CCD charge-coupled device. A device operated by manipulating charge packets held in capacitive bins.

CQED cavity quantum electrodynamics. A subfield of QED in which a resonator is used to modify the nature of matter-field interactions.

BB84 Bennett and Brassard, 1984. The first quantum key distribution protocol.

Published by Bennett and Brassard in 1984, its security rests on the No-Cloning theorem.

- CW** continuous-wave. A term used to describe lasers operating with continuous output.
- DBR** distributed Bragg reflector. Quarter-wavelength optical thickness semiconductor stack; a high reflector.
- FDTD** finite-difference time-domain. A method for numerically solving PDEs on a grid.
- FSR** free spectral range. The frequency difference between two adjacent longitudinal modes of the same transverse order in a resonator. In a hemispherical cavity $\text{FSR} = \frac{c}{2L}$, where L is the distance between the mirrors.
- IFQD** interface fluctuation quantum dot. A quantum dot formed from fluctuations of the interfaces of a quantum well.
- LOQC** linear optical quantum computing. A scheme for performing quantum computations that relies on single photons, linear optics and projective measurements.
- MBE** molecular beam epitaxy. A process in which molecular beams are used to deposit material layer-by-layer.
- MOT** magneto-optical trap. A method of trapping atoms using both a tapered magnetic field and counter-propagating laser beams to achieve a high degree of cooling.

NA numerical aperture. A measure of the acceptance angle of an optical system.

$NA = n \sin \theta$, where n denotes index of refraction.

NMR nuclear magnetic resonance. Phenomena relating to resonant interactions between the magnetic moment of a nuclear spin and an (electro-) magnetic field (usually in the RF band).

ODE ordinary differential equation. An equation involving only functions of a single independent variable and its derivatives.

OFHC oxygen-free, high-conductivity. An acronym used to describe copper specified as having a negligible content of oxides and hydroxyl groups. This provides for good conductive properties — both thermal and electrical.

PBS polarizing beam splitter: An optical device in which (for an assumed orientation of the device) vertically polarized light gets reflected and horizontally polarized light gets transmitted.

PDMS poly(dimethyl-siloxane). An organic silicone compound with elastomeric properties; commonly used to create molds for nano replication.

PID proportional-integral-derivative. A term describing a general class of feedback circuits capable of applying a control signal generated from some system output via proportionality, rate of change and integrated output.

PL photoluminescence. A form of spectroscopy utilizing optical excitation and measurement of the resulting emission spectrum.

PSD power spectral density. A measure of the “intensity” of a time series per unit frequency. In the context of surface measurements, it corresponds to the modulus square of height variations per unit spatial frequency.

PZT Lead-zirconate-tantalate. A widely used piezo-electric ceramic.

QCPG quantum controlled phase gate. A two-qubit quantum gate that applies a phase factor to each input provided the two qubit input state is $|11\rangle$. All other input states map back to themselves.

QD quantum dot. A zero dimensional object or a three dimensional potential well. Typically, it consists of a region of semiconductor surrounded on all sides by a material with a larger band gap.

QKD quantum key distribution. Any of various schemes utilizing properties of quantum systems to guarantee secure distribution of random bit-strings (i.e. one-time pad).

QW quantum well. A two dimensional structure exhibiting confinement in one dimension. It is generally formed by a layer of semiconductor, surrounded by another semiconductor with a higher band gap.

RWA rotating wave approximation. An approximation corresponding to moving to rotating coordinates.

SMF single-mode fiber. An optical fiber capable of supporting only a single mode at a specified wavelength.

SQD single quantum dot. A solitary semiconductor quantum dot.

TE transverse electric. A field whose electric field is everywhere perpendicular to the optical axis.

TM transverse magnetic. A field whose magnetic field is everywhere perpendicular to the optical axis.

TSA Technical Science Administration. Offers professional technological expertise and service to the scientific community of the University of Oregon.

UHV ultra-high vacuum. Pressure range of roughly: $P \lesssim 10^{-8}$ Torr.

BIBLIOGRAPHY

- [1] G. Bastard, E. E. Mendez, L. L. Chang, and L. Esaki. Exciton binding energy in quantum wells. *Phys. Rev. B*, 26(4):1974–1979, Aug 1982.
- [2] C. H. Bennett, G. Brassard, and A. Eckert. Quantum cryptography. *Scientific American*, 267:50, 1992.
- [3] E. D. Black. An introduction to pound–drever–hall laser frequency stabilization. *American Journal of Physics*, 69(1):79–87, 2001.
- [4] D. Bouwmeester, A. Ekert, and A. Zeilinger, editors. *The physics of quantum information: quantum cryptography, quantum teleportation, quantum computation*. Springer-Verlag, London, UK, 2000.
- [5] R. Bratschitsch and A. Leitenstorfer. Quantum dots: Artificial atoms for quantum optics. *Nature Materials*, 5:855–856, Nov 2006. 10.1038/nmat1768.
- [6] H.-P. Breuer and F. Petruccione. *The Theory of Open Quantum Systems*. Oxford University Press, 2002.
- [7] H. J. Carmichael. *Statistical Methods in Quantum Optics 1*. Springer, 1999.
- [8] H. J. Carmichael. *Statistical Methods in Quantum Optics 1*, chapter 1.5, pages 20 – 26. Springer, 1999.
- [9] H. J. Carmichael. *Statistical Methods in Quantum Optics 1*, chapter 7.3. Springer, 1999.
- [10] K. L. Chavez and D. W. Hess. A novel method of etching copper oxide using acetic acid. *Journal of The Electrochemical Society*, 148(11):G640–G643, 2001.
- [11] G. Cui. *An external optical micro-cavity strongly coupled to optical centers for efficient single-photon sources*. PhD thesis, University of Oregon, 2008.
- [12] G. Cui, J. M. Hannigan, R. Loeckenhoff, F. M. Matinaga, M. G. Raymer, S. Bhongale, M. Holland, S. Mosor, S. Chatterjee, H. M. Gibbs, and G. Khitrova. A hemispherical, high-solid-angle optical micro-cavity for cavity-qed studies. *Opt. Express*, 14(6):2289–2299, 2006.
- [13] G. Cui and M. G. Raymer. Quantum efficiency of single-photon sources in the cavity-qed strong-coupling regime. *Opt. Express*, 13,:9660–9665, 2005.

- [14] P. Domokos, J. M. Raimond, M. Brune, and S. Haroche. Simple cavity-qed two-bit universal quantum logic gate: The principle and expected performances. *Phys. Rev. A*, 52(5):3554–3559, Nov 1995.
- [15] M. I. Dyakonov. *Spin Physics in Semiconductors*, chapter 1, page 11. Springer, 2008.
- [16] X. Fan. Pure dephasing induced by exciton phonon interactions in narrow gaas quantum wells. *Solid State Communications*, 108:857–861, Nov. 1998.
- [17] D. H. Foster. Focused modes in the 60 μm cavity. Private communication.
- [18] D. H. Foster, A. K. Cook, and J. U. Nöckel. Goos-hänchen induced vector eigenmodes in a dome cavity. *Opt. Lett.*, 32(12):1764–1766, 2007.
- [19] D. H. Foster and J. U. Nöckel. Bragg-induced orbital angular-momentum mixing in paraxial high-finesse cavities. *Optics Letters*, 29(23):2788–2790, 2004.
- [20] D. H. Foster and J. U. Nöckel. Methods for 3-d vector microcavity problems involving a planar dielectric mirror. *Optics Communications*, 234(1-6):351 – 383, 2004.
- [21] D. Gammon, A. Efros, J. Tischler, A. Bracker, V. Korenev, and I. Merkulov. Electronic and nuclear spin in the optical spectra of semiconductor quantum dots. In T. Takagahara, editor, *Quantum Coherence Correlation and Decoherence in Semiconductor Nanostructures*, pages 207 – 280. Academic Press, San Diego, 2003.
- [22] D. Gammon, E. S. Snow, B. V. Shanabrook, D. S. Katzer, and D. Park. Fine structure splitting in the optical spectra of single gaas quantum dots. *Physical Review Letters*, 76(16):3005–3008, 1996.
- [23] A. V. Gopal and A. S. Vengurlekar. Well-width dependence of light-hole exciton dephasing in gaas quantum wells. *Phys. Rev. B*, 62(7):4624–4629, Aug 2000.
- [24] S. V. Goupalov. Anisotropy-induced exchange splitting of exciton radiative doublet in cdse nanocrystals. *Physical Review B (Condensed Matter and Materials Physics)*, 74(11):113305, 2006.
- [25] P. Goy, J. M. Raimond, M. Gross, and S. Haroche. Observation of cavity-enhanced single-atom spontaneous emission. *Physical Review Letters*, 50(24):1903–1906, 1983.
- [26] I. S. Gradshteyn and I. M. Ryzhik. *Table of Integrals, Series, and Products*, chapter 1. Academic Press, 5 edition, January 1994.

- [27] D. J. Griffiths. *Introduction to Electrodynamics*. Prentice-Hall, Inc., 2nd edition, 1989.
- [28] C.-H. Han and E.-S. Kim. Study of self-limiting etching behavior in wet isotropic etching of silicon. *Japanese Journal of Applied Physics*, 37(Part 1, No. 12B):6939–6941, 1998.
- [29] D. J. Heinzen, J. J. Childs, J. E. Thomas, and M. S. Feld. Enhanced and inhibited visible spontaneous emission by atoms in a confocal resonator. *Phys. Rev. Lett.*, 58(13):1320–1323, Mar 1987.
- [30] D. J. Heinzen and M. S. Feld. Vacuum radiative level shift and spontaneous-emission linewidth of an atom in an optical resonator. *Phys. Rev. Lett.*, 59(23):2623–2626, Dec 1987.
- [31] R. J. Hughes, J. E. Nordholt, D. Derkacs, and C. G. Peterson. Practical free-space quantum key distribution over 10 km in daylight and at night. *New Journal of Physics*, 4:43, 2002.
- [32] R. G. Hulet, E. S. Hilfer, and D. Kleppner. Inhibited spontaneous emission by a rydberg atom. *Phys. Rev. Lett.*, 55(20):2137–2140, Nov 1985.
- [33] A. Imamoglu, D. D. Awschalom, G. Burkard, D. P. DiVincenzo, D. Loss, M. Sherwin, and A. Small. Quantum information processing using quantum dot spins and cavity qed. *Phys. Rev. Lett.*, 83(20):4204–4207, Nov 1999.
- [34] E. L. Ivchenko. *Optical Spectroscopy of Semiconductor Nanostructures*, chapter 5.5, page 267. Alpha Science International Ltd., 2005.
- [35] A. Kiraz, C. Reese, B. Gayral, L. Zhang, W. V. Schoenfeld, B. D. Gerardot, P. M. Petroff, E. L. Hu, and A. Imamoglu. Cavity-quantum electrodynamics with quantum dots. *Journal of Optics B: Quantum and Semiclassical Optics*, 5(2):129–137, 2003.
- [36] D. Kleppner. Inhibited spontaneous emission. *Physical Review Letters*, 47(4):233–236, 1981.
- [37] E. Knill, R. Laflamme, and G. J. Milburn. A scheme for efficient quantum computation with linear optics. *Nature*, 409(6816):46–52, Jan 2001.
- [38] A. Kuhn, M. Hennrich, and G. Rempe. Deterministic single-photon source for distributed quantum networking. *Phys. Rev. Lett.*, 89(6):067901, Jul 2002.
- [39] V. D. Kulakovskii, G. Bacher, R. Weigand, T. Kümmell, A. Forchel, E. Borovitskaya, K. Leonardi, and D. Hommel. Fine structure of biexciton emission in symmetric and asymmetric cdse/zns single quantum dots. *Phys. Rev. Lett.*, 82(8):1780–1783, Feb 1999.

- [40] A. Larionov, M. Bayer, J. Hvam, and K. Soerensen. Collective behavior of a spin-aligned gas of interwell excitons in double quantum wells. *JETP Letters*, 81(3):108–111, Feb 2005.
- [41] M. Larsson, K. N. Dinyari, and H. Wang. Composite optical microcavity of diamond nanopillar and silica microsphere. *Nano Letters*, 9(4):1447–1450, 2009.
- [42] H. Mabuchi and A. C. Doherty. Cavity quantum electrodynamics: Coherence in context. *Science*, 298(5597):1372–1377, 2002.
- [43] F. D. Martini, G. Innocenti, G. R. Jacobovitz, and P. Mataloni. Anomalous spontaneous emission time in a microscopic optical cavity. *Phys. Rev. Lett.*, 59(26):2955–2958, Dec 1987.
- [44] P. L. McEuen. Quantum physics: Artificial atoms: New boxes for electrons. *Science*, 278(5344):1729–1730, 1997.
- [45] J. McKeever, A. Boca, A. D. Boozer, R. Miller, J. R. Buck, A. Kuzmich, and H. J. Kimble. Deterministic generation of single photons from one atom trapped in a cavity. *Science*, 303(5666):1992–1994, 2004.
- [46] S. E. Morin, C. C. Yu, and T. W. Mossberg. Strong atom-cavity coupling over large volumes and the observation of subnatural intracavity atomic linewidths. *Phys. Rev. Lett.*, 73(11):1489–1492, Sep 1994.
- [47] J.-W. Pan, D. Bouwmeester, H. Weinfurter, and A. Zeilinger. Experimental entanglement swapping: Entangling photons that never interacted. *Phys. Rev. Lett.*, 80(18):3891–3894, May 1998.
- [48] E. Pazy, E. Biolatti, T. Calarco, I. D’Amico, P. Zanardi, F. Rossi, and P. Zoller. Spin-based optical quantum computation via pauli blocking in semiconductor quantum dots. *EPL (Europhysics Letters)*, 62(2):175–181, 2003.
- [49] C.-Z. Peng, T. Yang, X.-H. Bao, J. Zhang, X.-M. Jin, F.-Y. Feng, B. Yang, J. Yang, J. Yin, Q. Zhang, N. Li, B.-L. Tian, and J.-W. Pan. Experimental free-space distribution of entangled photon pairs over 13 km: Towards satellite-based global quantum communication. *Phys. Rev. Lett.*, 94(15):150501, Apr 2005.
- [50] E. Peter, P. Senellart, D. Martrou, A. Lemaître, J. Hours, J. M. Gérard, and J. Bloch. Exciton-photon strong-coupling regime for a single quantum dot embedded in a microcavity. *Phys. Rev. Lett.*, 95(6):067401, Aug 2005.

- [51] U. Pohl, A. Schliwa, R. Seguin, S. Rodt, K. Pötschke, and D. Bimberg. *Advances in Solid State Physics*, chapter Size-Tunable Exchange Interaction in InAs/GaAs Quantum Dots, pages 45–58. Springer Berlin, 2007.
- [52] E. M. Purcell. Spontaneous transition probabilities in radio-frequency spectroscopy. *Physical Review*, 69:681[A], 1946.
- [53] J. P. Reithmaier, G. Sek, A. Löffler, C. Hofmann, S. Kuhn, S. Reitzenstein, L. V. Keldysh, V. D. Kulakovskii, T. L. Reinecke, and A. Forchel. Strong coupling in a single quantum dot-semiconductor microcavity system. *Nature*, 432:197–200, 2004.
- [54] K. Resch, M. Lindenthal, B. Blauensteiner, H. Böhm, A. Fedrizzi, C. Kurtsiefer, A. Poppe, T. Schmitt-Manderbach, M. Taraba, R. Ursin, P. Walther, H. Weier, H. Weinfurter, and A. Zeilinger. Distributing entanglement and single photons through an intra-city, free-space quantum channel. *Opt. Express*, 13(1):202–209, 2005.
- [55] T. M. Stace, G. J. Milburn, and C. H. W. Barnes. Entangled two-photon source using biexciton emission of an asymmetric quantum dot in a cavity. *Physical Review B (Condensed Matter and Materials Physics)*, 67(8):085317, 2003.
- [56] R. P. Stanley, R. Houdré, U. Oesterle, M. Gailhanou, and M. Ilegems. Ultrahigh finesse microcavity with distributed bragg reflectors. *Applied Physics Letters*, 65(15):1883–1885, 1994.
- [57] T. Takagahara. Theory of exciton dephasing in semiconductor quantum dots. *Physical Review B (Condensed Matter and Materials Physics)*, 60(4):2638–2652, 1999.
- [58] A. Thränhardt, C. Ell, G. Khitrova, and H. M. Gibbs. Relation between dipole moment and radiative lifetime in interface fluctuation quantum dots. *Phys. Rev. B*, 65(3):035327, Jan 2002.
- [59] M. Trupke, E. A. Hinds, S. Eriksson, E. A. Curtis, Z. Moktadir, E. Kukhareuka, and M. Kraft. Microfabricated high-finesse optical cavity with open access and small volume, 2005.
- [60] R. Ursin, T. Jennewein, M. Aspelmeyer, R. Kaltenbaek, M. Lindenthal, P. Walther, and A. Zeilinger. Communications: Quantum teleportation across the danube. *Nature*, 430(7002):849–849, Aug 2004.
- [61] T. Yoshie, A. Scherer, J. Hendrickson, G. Khitrova, H. M. Gibbs, G. Rupper, C. Ell, O. B. Shchekin, and D. G. Deppe. Vacuum rabi splitting with a single quantum dot in a photonic crystal nanocavity. *Nature*, 432:200–203, 2004.

- [62] Y. Zhang and M. Lončar. Submicrometer diameter micropillar cavities with high quality factor and ultrasmall mode volume. *Opt. Lett.*, 34(7):902–904, 2009.
- [63] A. Zrenner, L. V. Butov, M. Hagn, G. Abstreiter, G. Böhm, and G. Weimann. Quantum dots formed by interface fluctuations in alas/gaas coupled quantum well structures. *Phys. Rev. Lett.*, 72(21):3382–3385, May 1994.